EFFECTS OF A WINGTIP-MOUNTED PROPELLER ON WING LIFT, INDUCED DRAG, AND SHED VORTEX PATTERN

By

MELVIN H. SNYDER, JR.

Bachelor of Science
in Mechanical Engineering
Carnegie Institute of Technology
Pittsburgh, Pennsylvania
1947

Master of Science
in Aeronautical Engineering
Wichita State University
Wichita, Kansas
1950

Submitted to the Faculty of the
Graduate College of the
Oklahoma State University
in partial fulfillment of
the requirements for
the Degree of
DOCTOR OF PHILOSOPHY
May, 1967

EFFECTS OF A WINGTIP-MOUNTED PROPELLER
ON WING LIFT, INDUCED DRAG, AND
SHED VORTEX PATTERN

Thesis Approved:

Glen W. Zumwalt
Thesis Adviser

Ladislaus J Fila

J B Boggs

R B Deal

D D Durham
Dean of the Graduate College

PREFACE

The subject of induced drag is one that is both intriguing and frustrating to an aerodynamicist. It is the penalty that must be paid for producing lift using a wing having a finite span. Induced drag is drag that would be present even in a perfect (inviscid) fluid. Also present is the trailing vortex which produces the induced drag.

It was desired to determine whether it was possible to combine the swirling of a propeller slipstream with the trailing wing vortex in ways such that the wing loading would be affected and the induced drag either increased or decreased. This paper reports the results of a wind tunnel testing program designed to examine this idea.

Indebtedness is acknowledged to the National Science Foundation for the financial support through a Science Faculty Fellowship, which made possible graduate study at Oklahoma State University.

Acknowledgement is gratefully made of the guidance and encouragement of Dr. G. W. Zumwalt, graduate adviser, and Dr. J. H. Boggs and Dr. R. B. Deal, committee members; and of the constructive criticism of Professor L. J. Fila. Mr. Marvin Davidson, manager of the Walter H. Beech Wind Tunnel at Wichita State University, was very helpful during the model testing in the wind tunnel.

TABLE OF CONTENTS

LIST OF TABLES

LIST OF FIGURES

Figure		Page

Figure | Page

Figure		Page

LIST OF SYMBOLS

A	Aspect Ratio	
A	Area	sq. ft.
$\hat{a}_\theta$	Unit angular vector	
b	Span of wing (or other lifting surface)	ft.
b_v	Vortex span	ft.
C_D	Coefficient of drag, $\frac{D}{qS}$	
C_{D_i}	Induced drag coefficient	
C_{D_p}	Effective parasite drag coefficient	
C_{D_r}	Residual drag coefficient = $C_{D_p} - c_{d_{o_{min}}}$	
C_L	Coefficient of lift, $\frac{L}{qS}$	
$C_{L_{max}}$	Maximum lift coefficient	
C_{L_α}	Slope of lift curve, $dC_L/d\alpha$	per degree
C_M	Coefficient of pitching moment, $\frac{M}{qSc}$	
$C_{M_{c/4}}$	Coefficient of the moment about the wing quarter-chord	
C_T	Thrust Coefficient, $\frac{\text{Thrust}}{\rho N^2 d^4}$	
c	Chord of wing (or airfoil section)	ft.
c_{d_o}	Profile (two-dimensional airfoil section) drag coefficient	
D	Drag; component of force parallel to the freestream velocity direction	lb.
D'	Drag per foot of span, D/b	lb./ft.
D_i	Induced drag	lb.
d	Propeller (or impeller) diameter	ft.

d_v	Distance from wing to position of "fully rolled-up" vortex	ft.
e	Rate of expansion in x-direction	
e	Span efficiency factor $\frac{1}{\pi A} \frac{dC_D}{dC_L^2}$	
e_w	Wing efficiency factor, $\frac{1}{\pi A m} \approx \frac{1}{1+\delta}$	
F	Thrust	lb.
F	Force	lb.
f	Rate of expansion (divergence) in y-direction	
g	Rate of expansion (divergence) in z-direction	
h	Semi-height of end-plate, measured from wing chord to tip of end-plate (total height of a symmetrical end-plate is 2h)	ft.
$\hat{i}$	Unit vector in x-direction	
J	Advance ratio $\frac{V_a}{Nd}$	
$\hat{j}$	Unit vector in y-direction	
K	Constant	
$\hat{k}$	Unit vector in z-direction	
L	Lift; component of force normal to the freestream velocity direction	lb.
L'	Lift per foot of span, L/b	lb./ft.
l	Length	ft.
M	Pitching moment, about the y-axis	lb./ft.
$M_{c/4}$	Moment about the wing quarter-chord line	lb./ft.
m	Slope $\left(\frac{\Delta C_D}{\Delta C_L^2}\right)$ of straight line fit to wing data when plotted C_D vs. C_L^2	
N	Rotational speed of propeller	rev./sec.

n	Normal distance from a point to a vortex filament	ft.
p	Pressure	lb./ft.^{2}
p_a	Ambient (freestream) pressure	lb./ft.^{2}
p_L	Pressure acting on lower surface	lb./ft.^{2}
p_t	Total (stagnation) pressure, $p + qF_c \approx p_a + q$	lb./ft.^{2}
p_u	Pressure acting on upper surface	lb./ft.^{2}
q	Dynamic pressure, $\frac{1}{2}\rho V^2 = \frac{1}{2}\gamma p M^2$	lb./ft.^{2}
q_a	Free-stream dynamic pressure	lb./ft.^{2}
q_{ss}	Dynamic pressure in propeller slipstream	lb./ft.^{2}
R	Propeller radius, d/2	ft.
R'	Resultant force per foot of span of lifting surface (having components L' and D'), $\rho V_{res}\Gamma$	lb./ft.
$\overline{R}$	Vector position of point in flow field	
Re	Reynolds' number, $\frac{\rho V \ell}{\mu}$, Eff. Re = (Re)x(T.F.)	
r	Radius	ft.
r_c	Radius of rotational core of rolled-up trailing vortex	ft.
S	Wing area	sq. ft.
S_p	Portion of wing area in propeller slipstream	sq. ft.
T_C	Thrust coefficient, $\frac{\text{Thrust}}{e_2 V^2 d^2}$	
t	Thickness of airfoil, esp. max. thickness	ft.
u	X-component of velocity	ft./sec.
V	Velocity = $\lvert\overline{V}\rvert$	ft./sec.

V_a	Freestream velocity	ft./sec.
V_{min}	Minimum level-flight velocity, corresponds to $C_{L_{max}}$	ft./sec.
V_{max}	Maximum level-flight speed	ft./sec.
V_{res}	Resultant (of V_a and w) velocity	ft./sec.
V_s	Velocity along a surface or boundary	ft./sec.
V_{ss}	Velocity in propeller slipstream	ft./sec.
V_θ	Velocity on a cylindrical surface at angle θ from stagnation point	ft./sec.
$\overline{V}$	Total velocity vector	ft./sec.
$\overline{V}_o$	Translational component of velocity vector	ft./sec.
$\overline{V}'$	Rotational component of velocity vector	ft./sec.
$\overline{V}''$	Vectorial representation of divergence of velocity	ft./sec.
v	Y-component of velocity	ft./sec.
W	Airplane weight	lb.
w	Z-component of velocity	ft./sec.
w	Downwash velocity	ft./sec.
x	Dimension parallel to wind tunnel centerline	ft.
y	Dimension measured spanwise from the plane of symmetry normal to tunnel centerline	ft.
z	Dimension normal to x and y	ft.
α	Angle of attack	degrees
α_i	Induced angle of attack $18.24 \frac{C_L}{A}(1+\tau)$	Degrees
α_o	Airfoil section (two-dimensional) angle of attack	degrees
β	Propeller blade pitch angle	degrees

β	Angle between radial line and the normal to the vortex filament	degrees
Γ	Circulation, $\oint_s V_s ds$	ft.^{2}/sec.
Γ_0	Circulation at mid-span	ft.^{2}/sec.
γ	Airplane approach angle, $\tan^{-1} \frac{D - F}{L}$	degrees
γ	Strength of vortex sheet	ft./sec.
Δ	Increment	
δ	Glauert (induced drag) factor	
δ_e	End-plate deflection angle	degrees
δ_f	Flap deflection angle	degrees
ε	(negative) downwash angle	radius
μ	Viscosity	slugs/ft. sec.
ρ	Density (fluid, air)	slugs/ft.^{3}
σ	Angle between path of integration and velocity vector	degrees
Σ	Summation	
τ	Glauert (induced angle of attack) factor	
θ	Angle of rotation (or of position)	degrees
$\bar{\Omega}$	Angular velocity of rotation	rad./sec.
ω	$= \lvert\bar{\Omega}\rvert$	
ζ	Vorticity, $\frac{\Gamma}{A}$	1/sec.

SUBSCRIPTS

a	Freestream or ambient
c/4	Quarter chord point or line
D	Drag
e	End-plates
i	Induced
L	Lift
L	Lower surface
$M_{c/4}$	Pitching moment about the quarter-chord line
o	Oval end-plate
p_e	Equivalent parasite
res	Resultant
r	Round end-plate
V	Upper surface
p	Propeller
O	Center of span

CHAPTER I

INTRODUCTION

The use of a wing, having a finite span, to produce lift results in three penalties which would not exist if the lifting surface had an infinite span. These three penalties are:

1. Decrease in lift near the wing tips (and, therefore, a lower C_L of the wing at any angle of attack and a lower $C_{L_{max}}$).
2. Increase in wing drag by the amount of the induced drag.
3. Creation of downwash behind the wing (e.g., at the tail surfaces) which is not constant, but is a function of the wing lift coefficient.

This fact has long been recognized. At the turn of the century, Lanchester postulated the type of flow that a real finite span wing would experience. His sketches predicted the formation and shedding of vortices which wrap up into large-scale vortices trailing downstream from each wing tip. Figure 1 is a reproduction of his sketches published in Aerodynamics (27).

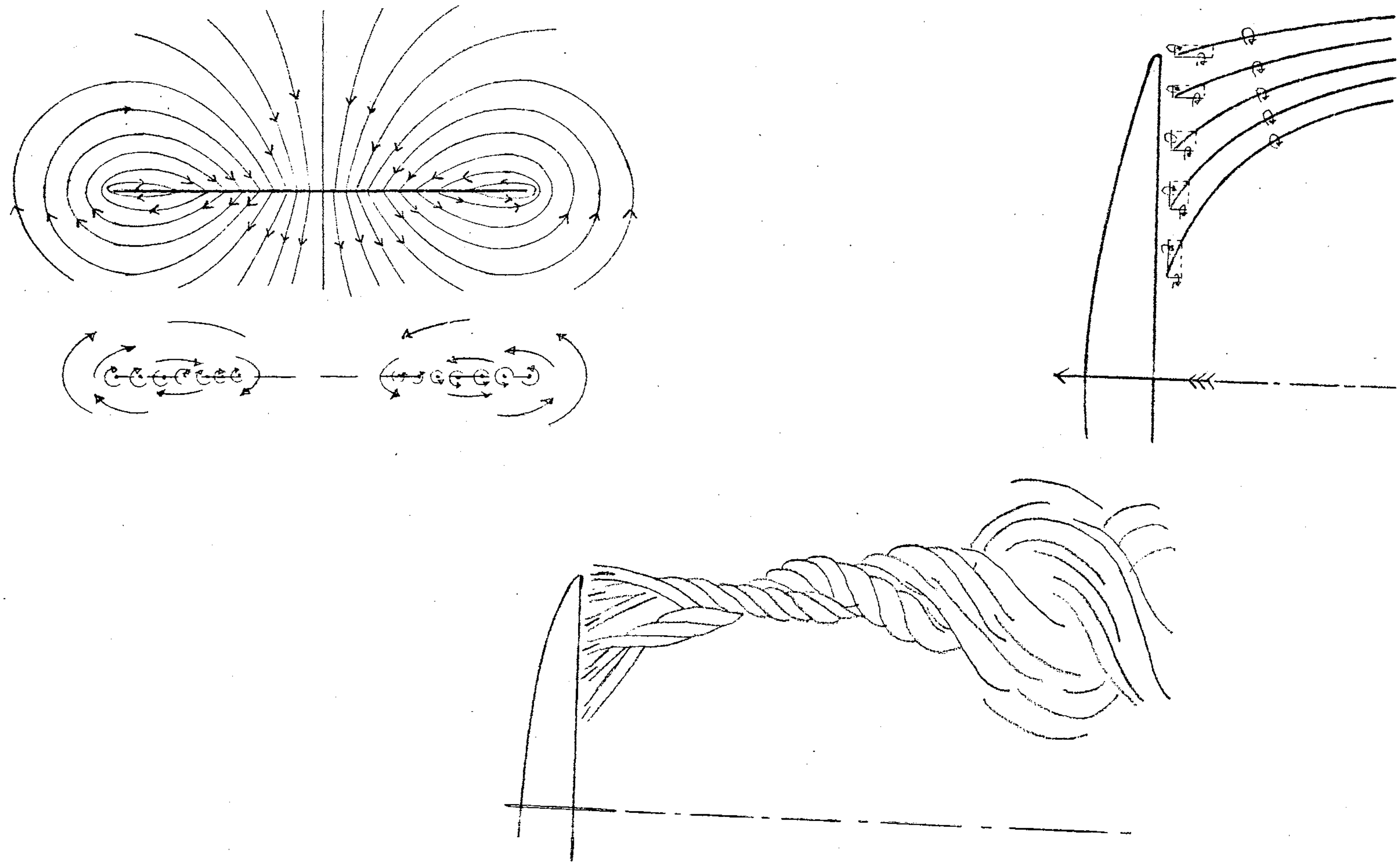

Figure 1. Lanchester's Sketches of Vortex Motion in the Peripterv

Prandtl first discussed the problem of the three-dimensional flow over a wing of finite span in 1911 and published his treatment of the problem in 1918. The Prandtl wing theory is the basis for most of the work which has been done to date on the finite-span lifting wing.

Not only have the problems been long recognized, but the history of the attempts to improve the effectiveness of a finite lifting wing predates the Wright brother's first powered flight. Pope (37) reports that Lanchester secured a patent in 1897 covering the use of end-plates on wings!

The principal objectives of various schemes to alter the flow around finite-span wings are:

a) The increase of wing lift (i.e., increase $C_{L_{max}}$ and C_{L_α}).

b) The decrease of wing drag (by reduction of induced drag).

The maximum lift coefficient of the wing is always less than the maximum coefficient of lift of the wing sections in two-dimensional flow. The reason for this difference is that the loss of lift near the wing tips causes the maximum lift coefficient of sections near the tips to be less than if the flow were two-dimensional. Also, the stall of the wing effectively begins when some portion of the wing stalls; that is, there is separation locally at some point on the airfoil. Although most of the wing may be unstalled, the wing C_L will not continue to increase as α increases after a portion of the wing stalls.

It is, however, the induced drag which, in the past, has been the target of most of the improvement devices. The induced drag varies inversely with the square of the wingspan for a given wing loading. It is at low speeds that the induced drag is particularly important. At the velocity for maximum range of an airplane the induced drag is equal in magnitude to the skin friction drag of the wing and airplane. At speeds less than this speed the induced drag is greater than the drag of the rest of the airplane.

Included among the desirable traits for an airplane wing are:

a) High $C_{L_{max}}$.

b) Low values of induced drag (for takeoff and climb).

c) High value of induced drag (for approach and landing).

The physical span of an aircraft wing is limited by practical considerations. As mentioned above, the earliest (and the most often repeated) approach to the goal of making a wing perform as though the span were greater, has been the modification of wingtip geometry (e.g., through the use of end-plates, tip-bodies, etc.). In this paper, these methods are examined in Chapter II and shown to be inferior. However, it is possible to attain many of the desired wing traits by the use of rotating propellers at the wingtips. This application of energy to the flow field through the use of mechanical rotors is the subject of the experimental program reported in this paper. These experiments are examined in detail in Chapters III and IV.

CHAPTER II

EVALUATION OF END-PLATES

It could be said that an infinite-span wing would not be necessary if it were possible to force the air to behave as though the span were infinite; i.e., if it were possible to maintain two-dimensional flow over the three-dimensional wing. The (apparently) obvious approach to this objective is through the use of end-plates.

Conventional End-Plates

In 1927, Hemke (21) reported a systematic investigation of the effect of end-plates on the drag of wings. Hemke reached the following conclusions:

> Calculations show that the induced drag of monoplanes and multiplanes may be decreased by attaching end-plates to the ends of the wing. The frictional drag of the end-plates may be calculated approximately. The reduction of the induced drag exceeds the additional frictional drag due to the end-plates at all but the small values of lift. For given dimensions of wings and end-plates the reduction of drag less the friction of drag of the end-plates varies directly as the square of the absolute lift coefficient. The average reduction of drag decreases as the aspect ratio decreases. Calculations and experiments agree quite satisfactorily for single wings equipped with end-plates.
>
> Wind tunnel tests show that the coefficients used in calculating a frictional drag of the

> end-plates may be reduced by fairing the end-plates. The shape of the end-plate determines to some extent the reduction of induced drag ...
>
> Recent experiments have shown that much higher lift coefficients can be obtained than have been the case up to now with the conventional airfoils ...

Although these conclusions seem favorable to the idea of attaching end-plates to the wing, the period following the publication of this report was not marked by the application of end-plates to aircraft wings. The key sentence in the conclusions is the one which states that the reduction of the induced drag exceeds the additional frictional drag due to the end-plates <u>in all but the small values of the lift</u>. It is at these "small values of the lift" (actually, at small values of lift coefficient) that the airplane flies at high speed. This fact means that the additions of end-plates to the wing will limit the high speed performance of the aircraft.

The models reported on by Hemke were rather small (four inches chord) and the Reynolds Number of the tests, although not stated in the report, were probably quite low. In order to determine whether Hemke's conclusions were valid, a brief wind tunnel investigation was conducted.

This test and all of the powered model testing, reported in the following chapters, were performed in the Walter H. Beech Memorial Wind Tunnel on the campus of Wichita State University. This wind tunnel is a horizontal, single-return, closed-throat tunnel. A plan of the tunnel is shown in Figure 2.

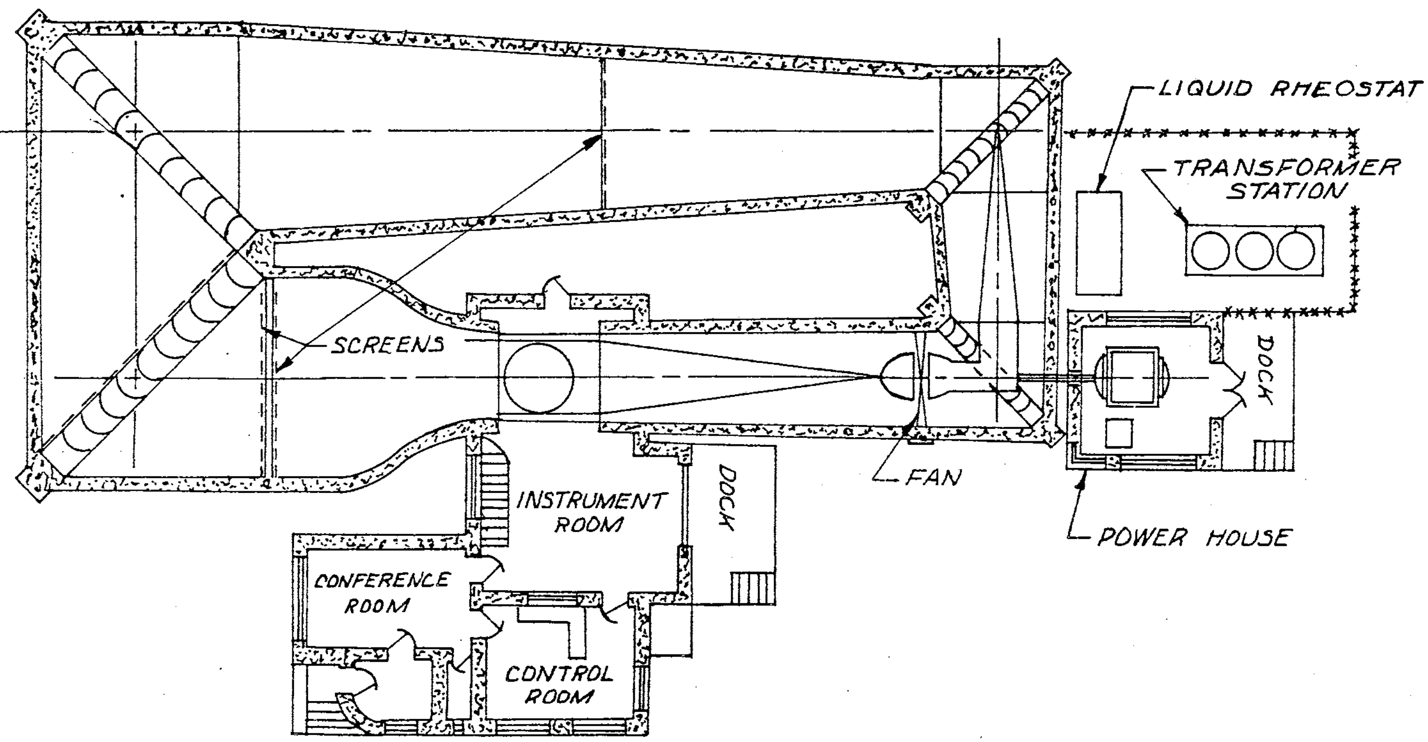

Figure 2. Plan of Walter H. Beech Wind Tunnel

The test section is 7 feet by 10 feet with corner fillets which reduce the cross-sectional area to 68 square feet. The test section is 12 feet long. The tunnel is powered by a 1500 horsepower motor, and the speed is varied by controlling the propeller pitch. The six component pyramidal balance is mounted below the test section floor. The balance readings, together with angles of attack and yaw, test section dynamic pressure, ambient pressure and temperature and run number are recorded by an on-line card punch. Because the mounting of the reflection plane model of the wing required that the wing be rotated 90 degrees from the conventional position, the wing lift was measured by the side-force balance, the pitching moment of wing was measured by the yawing moment balance, and drag was measured by the drag balance. Only these three components were measured.

The end-plate test program consisted of a reflection-plane wing model (referred to as the auxiliary model) tested in the wind tunnel in the following configurations:

1. The basic constant-chord wing with a plain square wingtip.
2. The wing with a round end-plate.
3. The wing with an oval end-plate.

The model details are sketched in Figure 3, and Figure 4 shows the model under test in the wind tunnel. The model is a plastic-foam model with a wooden span and covered with fiberglas.

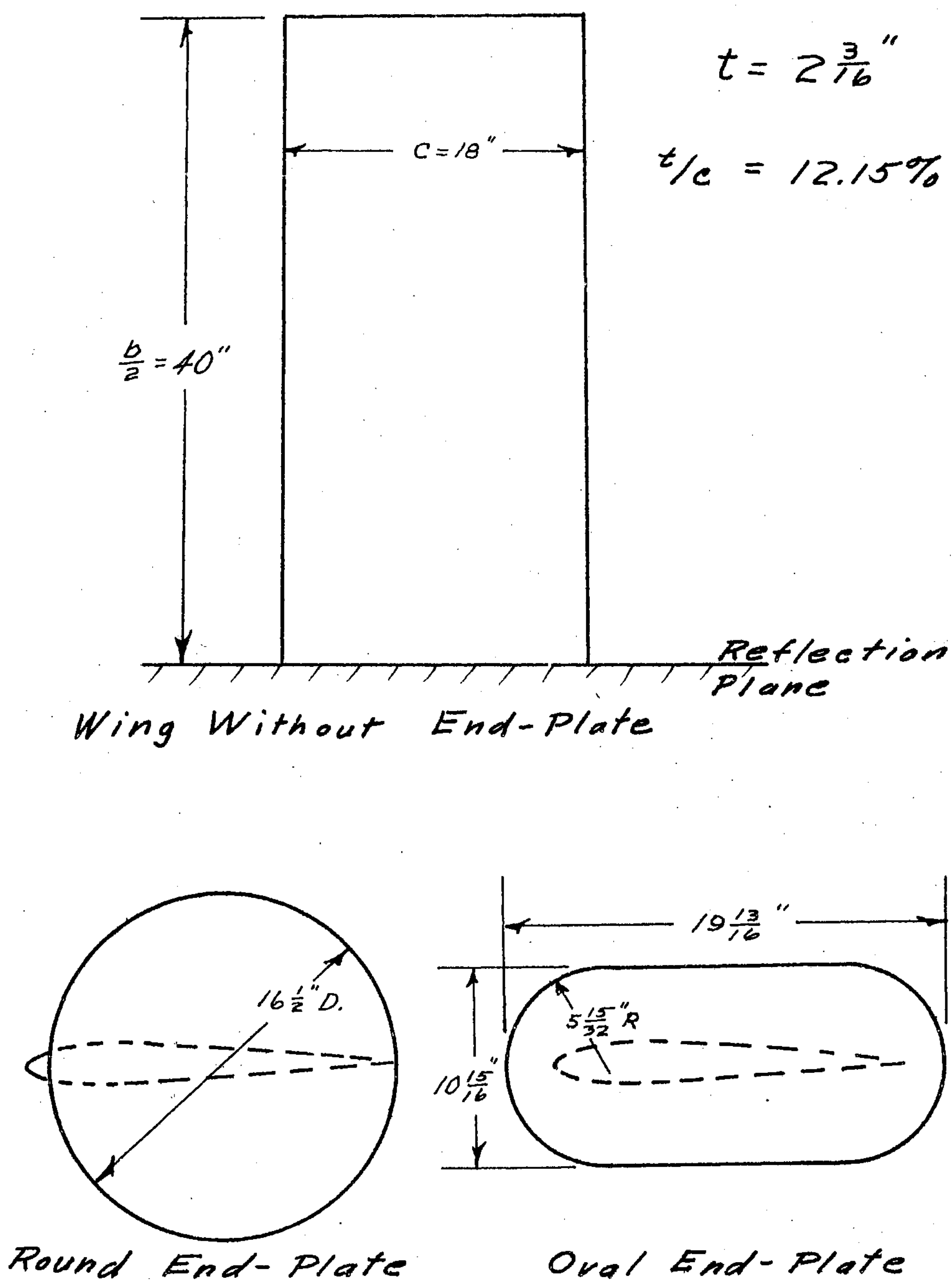

Figure 3. Auxiliary Model and End-Plates

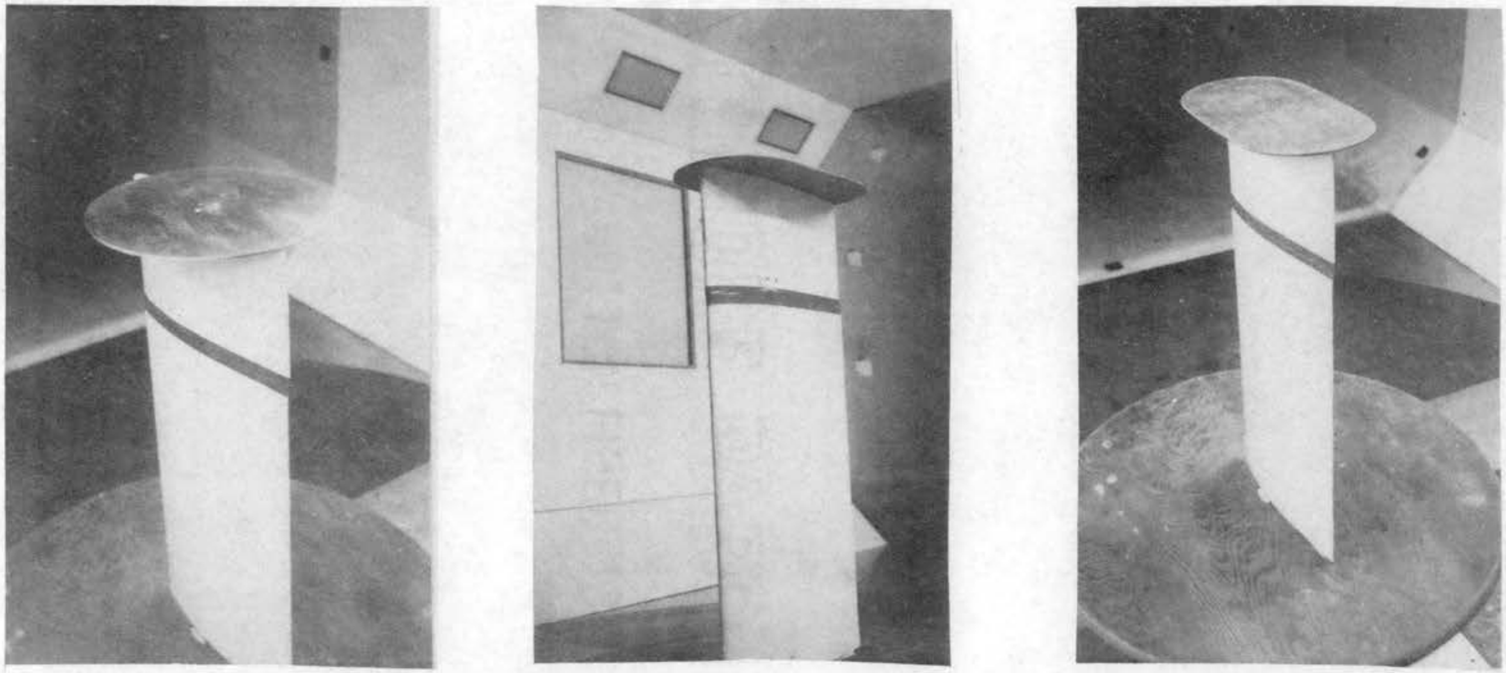

a b c

Figure 4. Supplementary Model With End-Plates Being Tested in the Wind Tunnel

The effective Reynolds Number of the test was 1.6×10^6.

The addition of end-plates to a wing should have two principal effects:

1. Decrease in induced drag.
2. Increase in lift at any angle of attack (greater than angle of zero lift) resulting in increased slope of the lift curve and increased $C_{L_{max}}$.

These effects can be seen in Figures 5 and 6.

The basic wing has the dimensions:

Span = 80 inches

Chord = 18 inches

Area = 1440 square inches

Aspect Ratio = 4.44

The characteristics of the wing in the three configurations tested are summarized in Table I.

It will also be noted that the basic wing has a lower total drag than the wing with round end-plates in the range of C_L from 0 to 0.2 and a lower drag than with oval end-plate in the range $0 < C_L < 0.3$.

As expected, the end-plates improved the induced drag characteristics of the wing, increasing the effective aspect ratio. The increased $C_{L_{max}}$ will result in decreasing the minimum flight speed. It is necessary to examine whether this method of accomplishing these ends is an efficient one. If, instead of putting end-plates on the

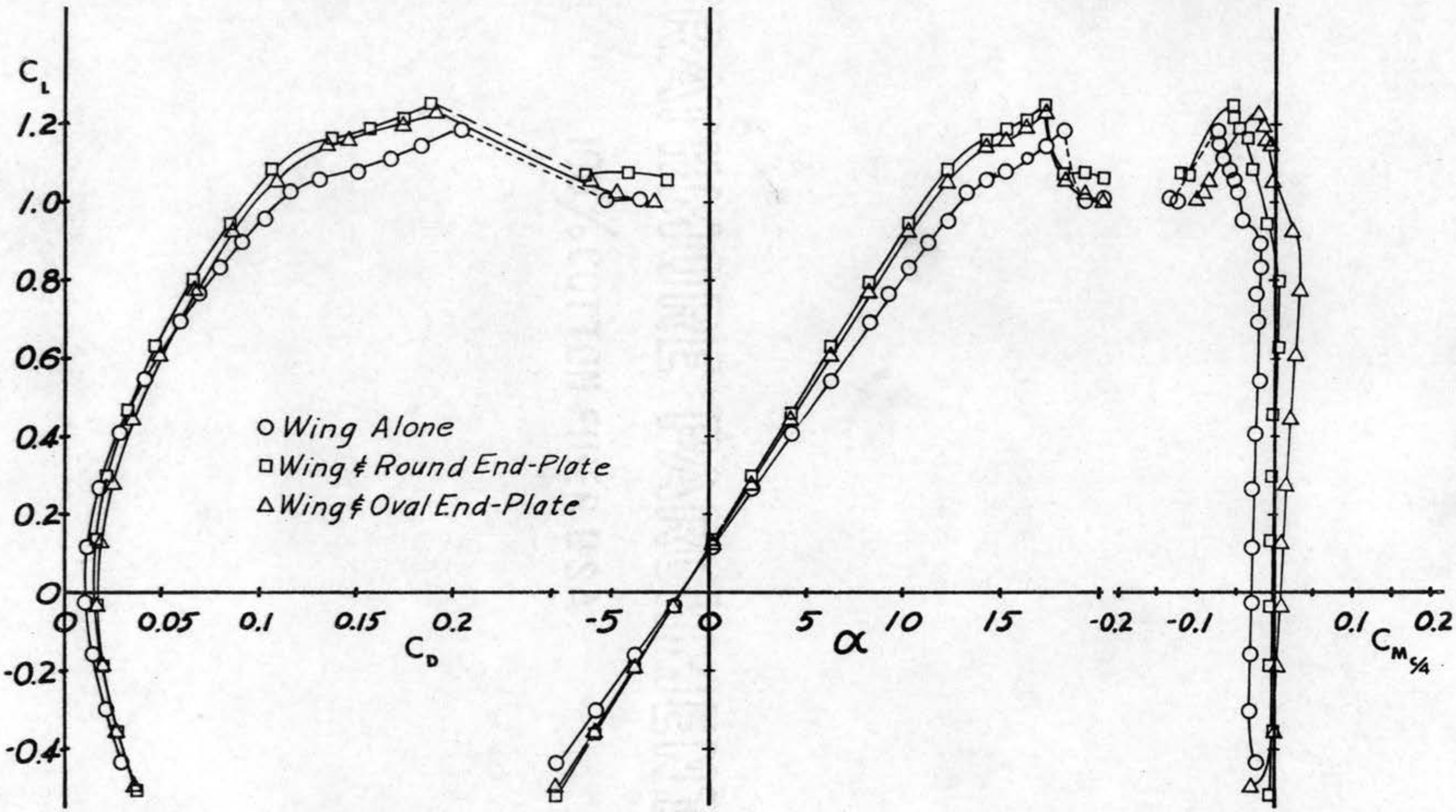

Figure 5. Supplementary Model Characteristics

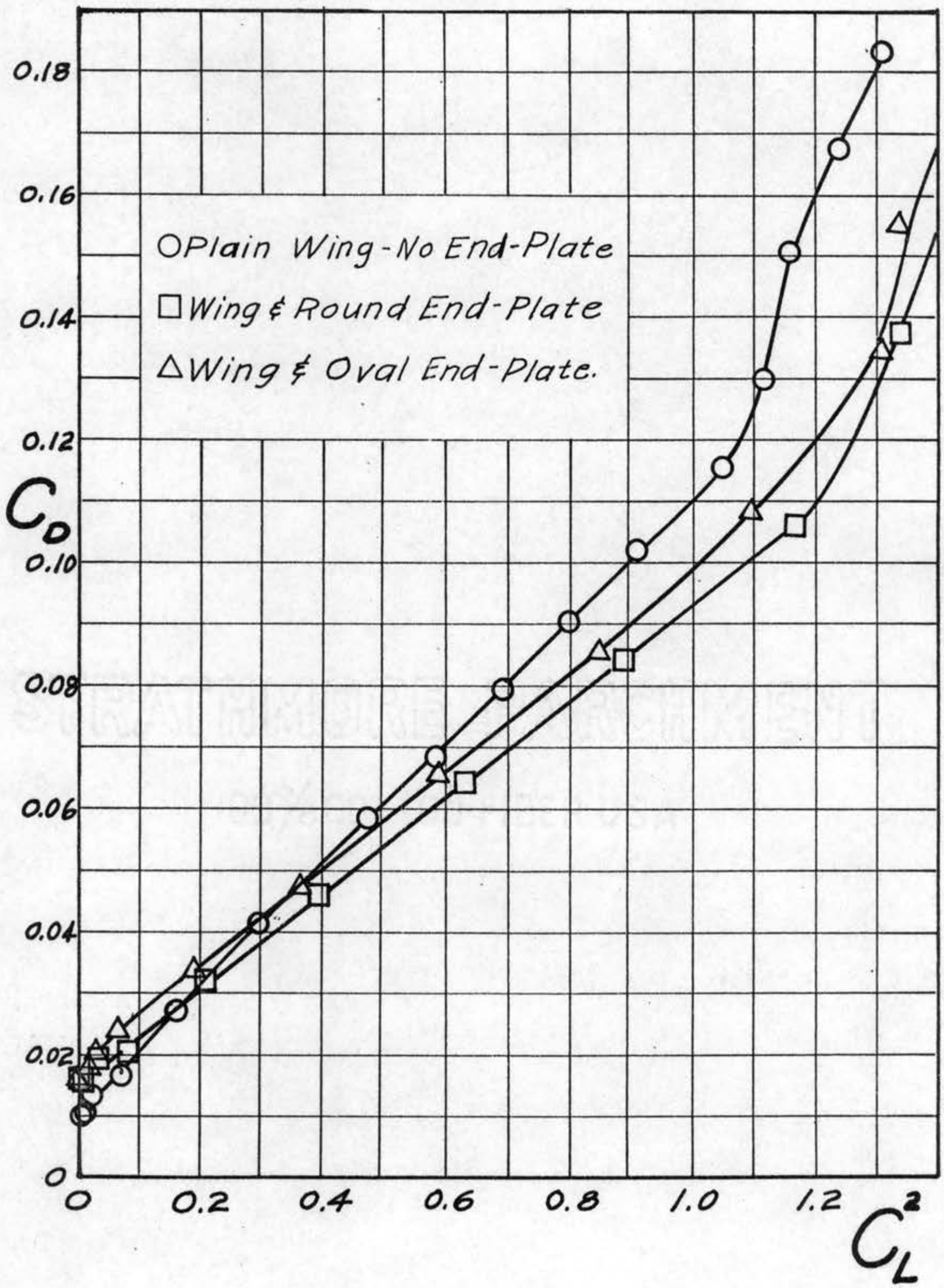

Figure 6. Supplementary Model Drag

TABLE I

SUMMARY OF CHARACTERISTICS OF AUXILIARY MODEL

Wing Characteristic	Basic Wing	With Round End-Plate	With Oval End-Plate
Lift-Curve Slope	0.072 per deg	0.0815	0.0815
$C_{L_{max}}$	1.185	1.249	1.229
$V_{min}/(V_{min})_{basic\ wing}$	1.0	0.97	0.98
C_D equation	$C_D = 0.011 + 0.0987 C_L^2$	$C_D = 0.0159 + 0.0764 C_L^2$	$C_D = 0.0188 + 0.0784 C_L^2$
e_w	0.725	0.938	0.914
Eff. Aspect Ratio = Ae_w	3.23	4.17	4.06
C_D at $C_L = 1$	0.109	0.092	0.098

wing, the same area were added to the wing by extending the wing span, the following results would obtain (Prime indicates extended span wing):

Round end-plate area = 214 sq. in. (each)

Semispan increment = 11.89 in.

$$A' = \frac{(b')^2}{S'} = \frac{(103.78)^2}{1868} = 5.77$$

If it is assumed that this extended span wing would have the same span efficiency factor as the basic wing, i.e., $e_w = 0.725$, then the effective aspect ratio would be $(A'e_w) = 5.77\ (.725) = 4.19$. Then the drag equation would be:

$$C'_D = 0.11 + \frac{1}{4.19\pi} C_L^2$$

$$C'_D = .011 + .076 C_L^2 .$$

These calculations show that if, instead of installing the round end-plate, the same area were added to the wingtip in the form of an extension of the span, the result would be an effective aspect ratio almost exactly the same as that resulting from the end-plate. The coefficient of drag of the extended wing will be less than that of the basic wing with round end plates at any given C_L.

The drag of the two wings have been compared on the basis of same flight velocities or on the basis of the same wing-loading (gross weight of extended wing airplane is increased). In each case, the drag of the extended wing is less than that of the wing plus end-plates.

Calculations may be repeated for the oval end-plate:

Oval end-plate area = 190.7 square inches

Extended wing area = 1821.4 square inches

$A' = 5.625$, $A'e_W = 4.08$ (compared to 4.06 with oval end-plate)

$C'_D = .011 + .078C_L^2$

Again, it can be seen that extension of the basic wing results in lower drag coefficient. The extended wing has less drag.

Full airplane model tests with rectangular and end-plates were previously conducted in the same wind tunnel at an effective Reynold's Number of 1,840,000. Three of the configurations tested are shown in Figure 7. These tests were reported by Morris (33) and the results are reproduced in Figure 8. It can be seen that only at the high lift coefficients is the drag of the wing with end-plates lower than that of the basic wing (in this case, $C_L > 0.7$).

These results confirm the conclusions reached by Riley (42):

> Substantial increases may be obtained in the maximum lift-drag ratio of wing-body combinations or complete airplanes, for which the total drag of the components other than the wing is large relative to the wing drag, by the use of appropriately designed end-plates. Except possibly for the smaller end-plates area, however, the increases obtained are not likely to be as large as those which would be obtained by utilizing the end-plate area as a simple addition to the wing span,

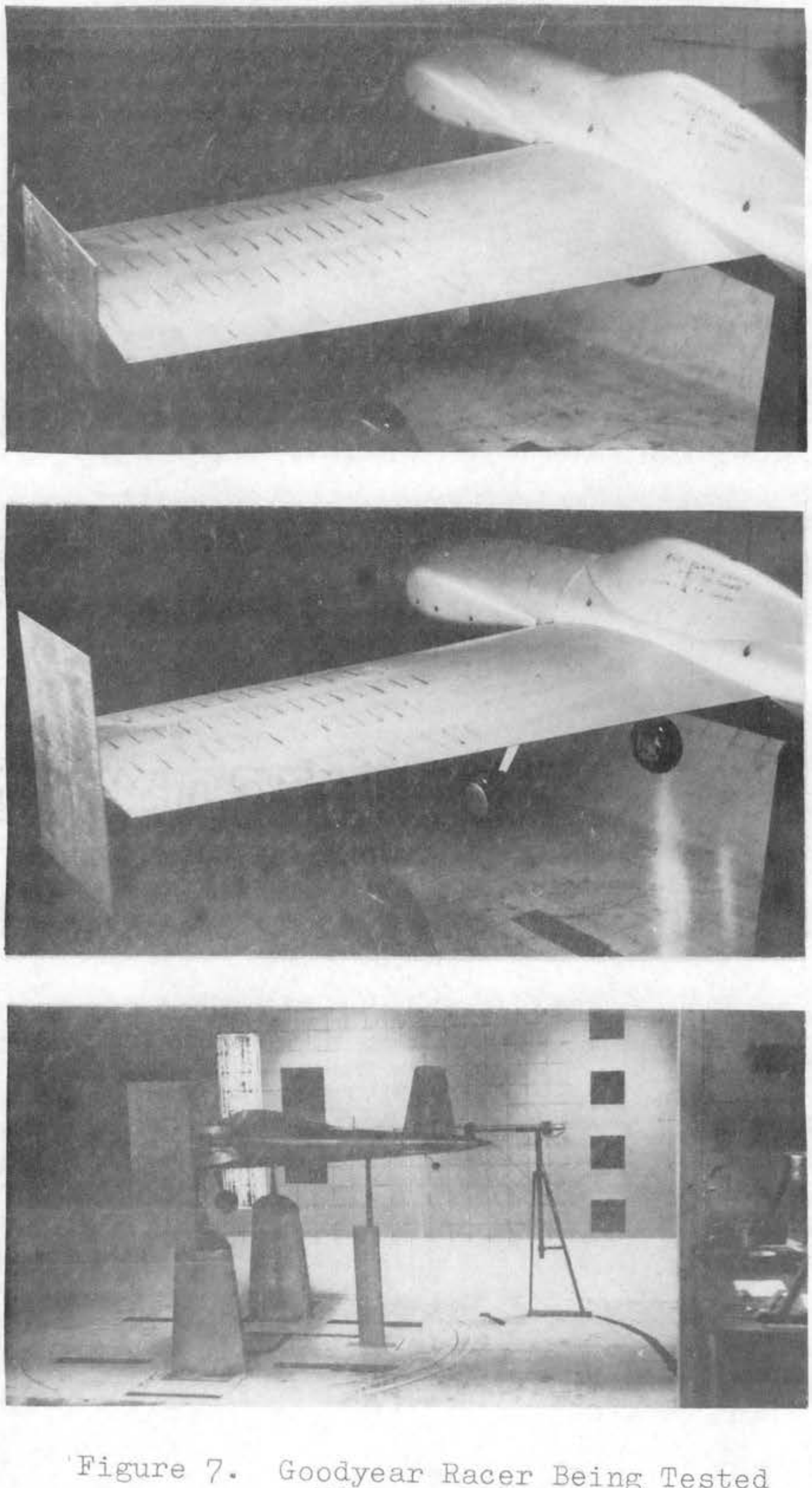

Figure 7. Goodyear Racer Being Tested
With End-Plates

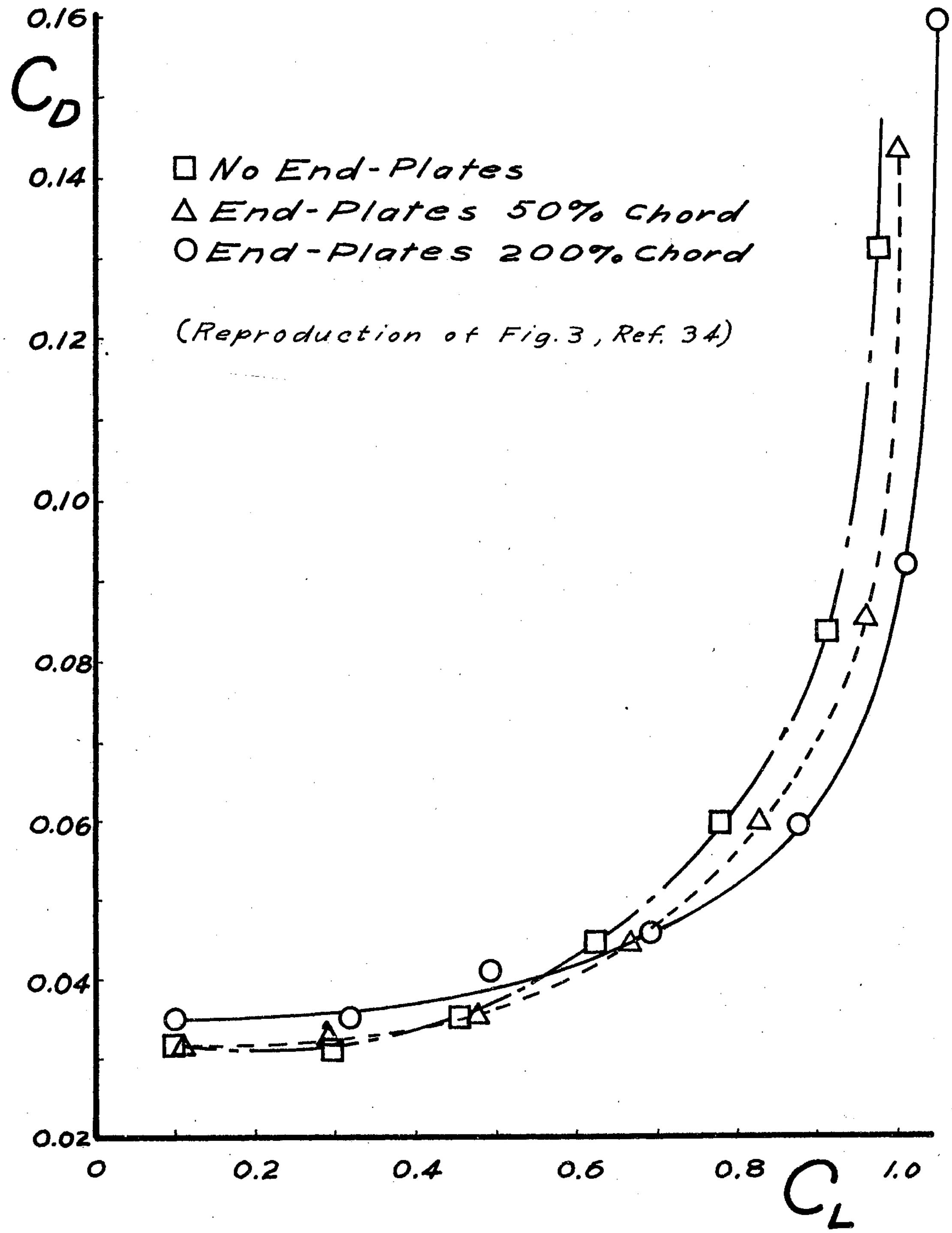

Figure 8. Effect of End-Plates on Drag of Goodyear Racer

> thus increasing the wing geometric aspect ratio.
>
> The maximum lift coefficient of the wing experienced an increase when the end-plates were added. The rate of increase, however, decreased with increasing end-plate area.

Similarly, Hoerner (22) stated:

> Basically, the end-plates have at least the drag of a pair of added wingtip extensions (having the same area). Any such added area naturally produces more lift for the same price of viscous drag. Practical application of end-plates in airplanes and/or guided missiles, therefore, seems to be restricted to such designs where the plates can also be utilized for stabilizing or control purposes.

Garbell (15) has discussed these cases of using wing-tip fins instead of centrally-located vertical fins.

For most of the history of flight, the major emphasis has been on increasing the cruise and top-speed flight velocities. These flight regimes are at low value of lift coefficient. It is logical, then, that end-plates have not been built onto aircraft for the reasons stated above. However, in recent years, increasing interest in STOL aircraft has made it reasonable to consider schemes which might sacrifice high-speed performance to attain low-speed capability. It was this attitude which led Lowry and Vogler (28) to investigate the use of end-plates on wings equipped with jet flaps and for Morris and Ten Eyck (34) to consider the combination of end-plates and circulation control to improve the landing and take-off distances of a reconnaissance-type airplane.

The Morris and Ten Eyck analysis determined the effects of wing aspect ratio, end-plates, and circulation control on the distances to land and take-off over a 50 foot obstacle. Assumed conditions included:

Gross Weight	2100 pounds
Standard sea-level atmsophere Runway friction coefficient:	0.06 for take-off 0.40 for landing
Maximum C_L for take-off:	No C.C., 29° flap: 2.24 With circulation control: 4.0
Maximum C_L for landing:	No C.C., 60° flap: 2.0 With circulation control: 3.0
Wing area	174 square feet
Taper ratio	1.5

Two types of end-plates:

(1) End-plates of 9% S were added to wingtip.

(2) Wingtip turned up at each end so that turned-up area was 9% of remaining area.

Equivalent parasite drag coefficient 0.028

Addition of end-plates increased e by 40%.

The results of this analysis are shown graphically in Figures 9 and 10. Examination of these figures leads to the following conclusions:

1. Addition of end-plates would not shorten landing distance.

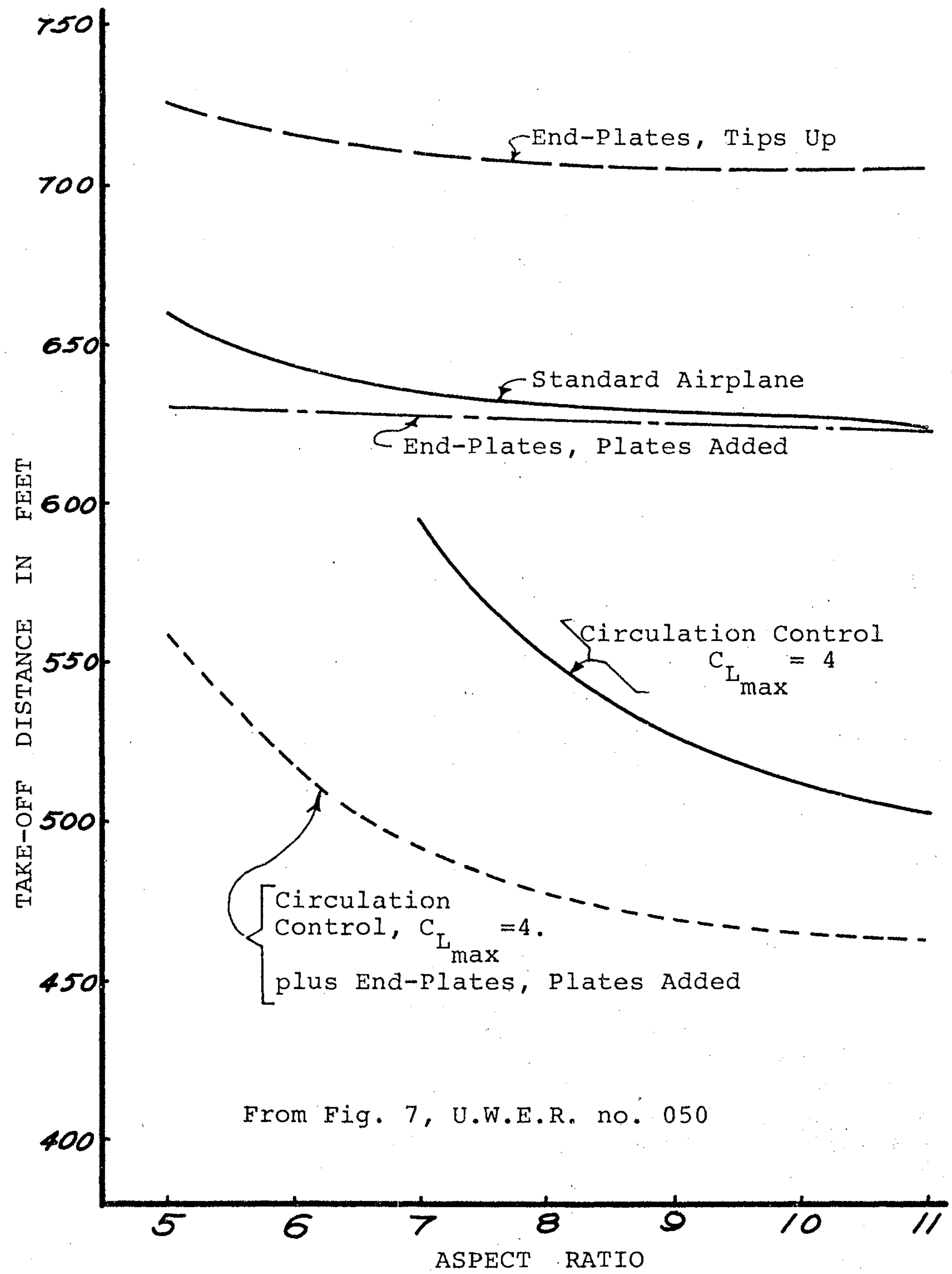

Figure 9. Effect of End-Plates on Take-Off Distance

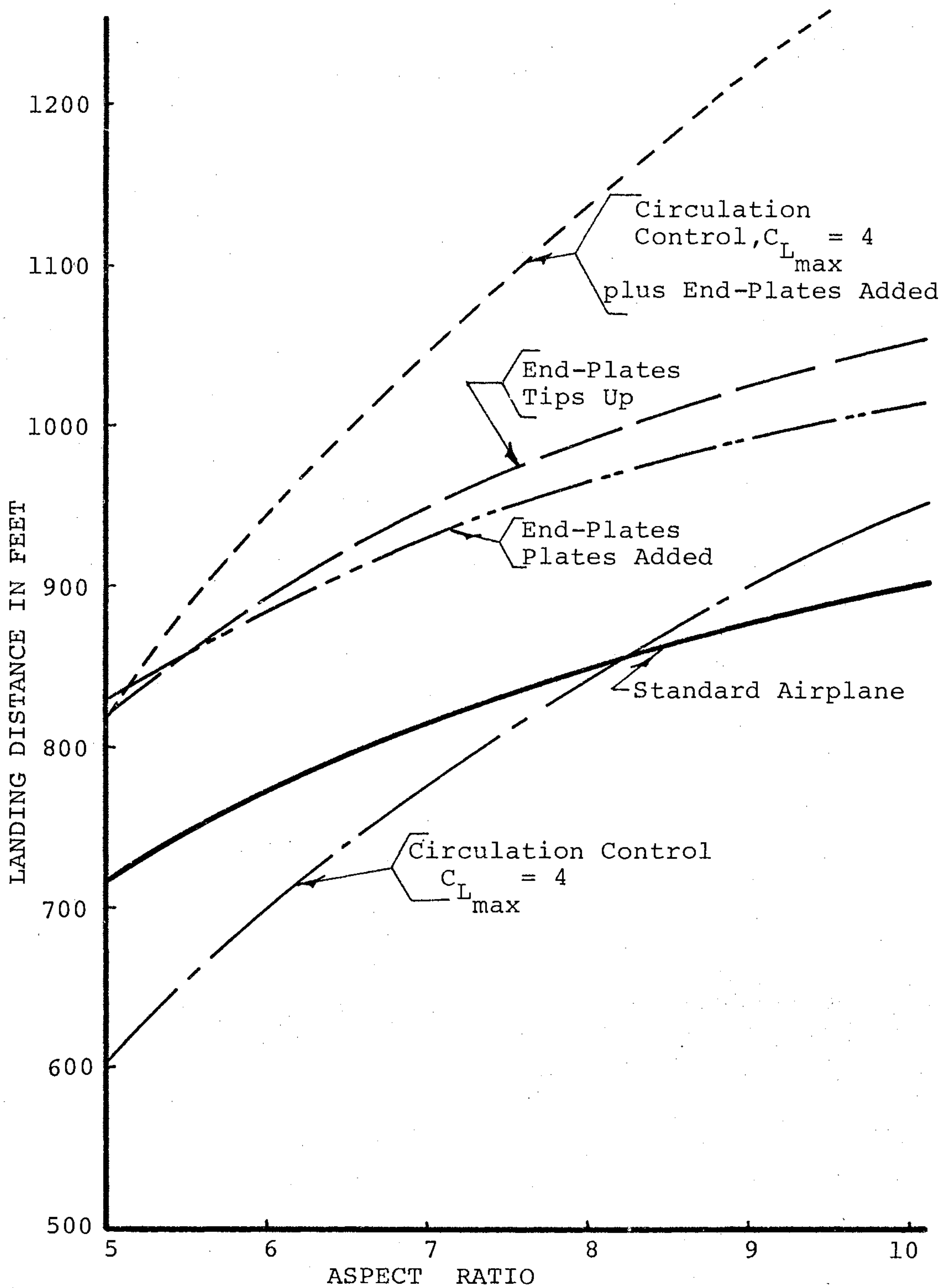

Figure 10. Effect of End-Plates on Landing Distance (over 50 ft. obstacle)

2. End-plates used in conjunction with circulation control would decrease take-off distance.

3. The area used in forming end-plates could be used to better advantage in the form of increased wing area.

The reason for the degradation of the landing performance with end-plates is that the decrease in D/L produces a flatter approach (i.e., smaller angle of glide, γ), as shown in Figure 11.

The approach angle is $\gamma = \text{arc tan}\ \frac{(D - F)}{L}$. In the final approach for minimum landing distance, F is negligible so that $\gamma = \text{arc tan}\ \frac{D}{L}$. Since landing distance is the distance from a 50-foot obstacle to the aircraft stopped position, the angle of approach has a marked effect on landing distance. It is desirable for D/L to be large for landing. Figure 12 illustrates the effect of D/L on the landing distance.

Variable-Geometry End-Plates

These opposing D/L requirements for take-off and landing led Clements (6 and 7) to devise variable-geometry end-plates for the purpose of controlling C_{D_i} (and, thus, D/L) to increase the angle of glide for landing and to decrease the take-off roll. It was his idea that, by making the end-plates of symmetrical airfoils with hinged sections, the induced drag could be increased

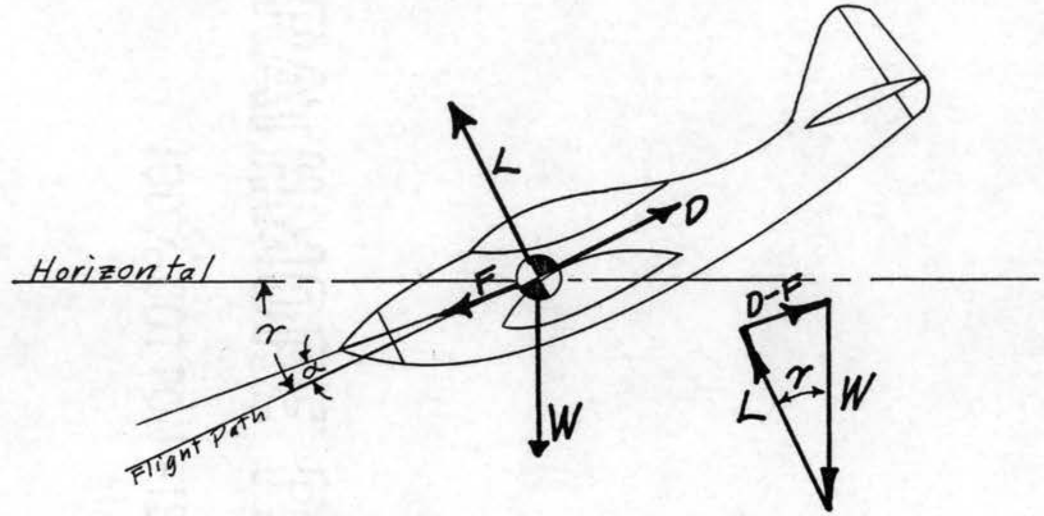

Figure 11. Forces on Aircraft in Approach Flight

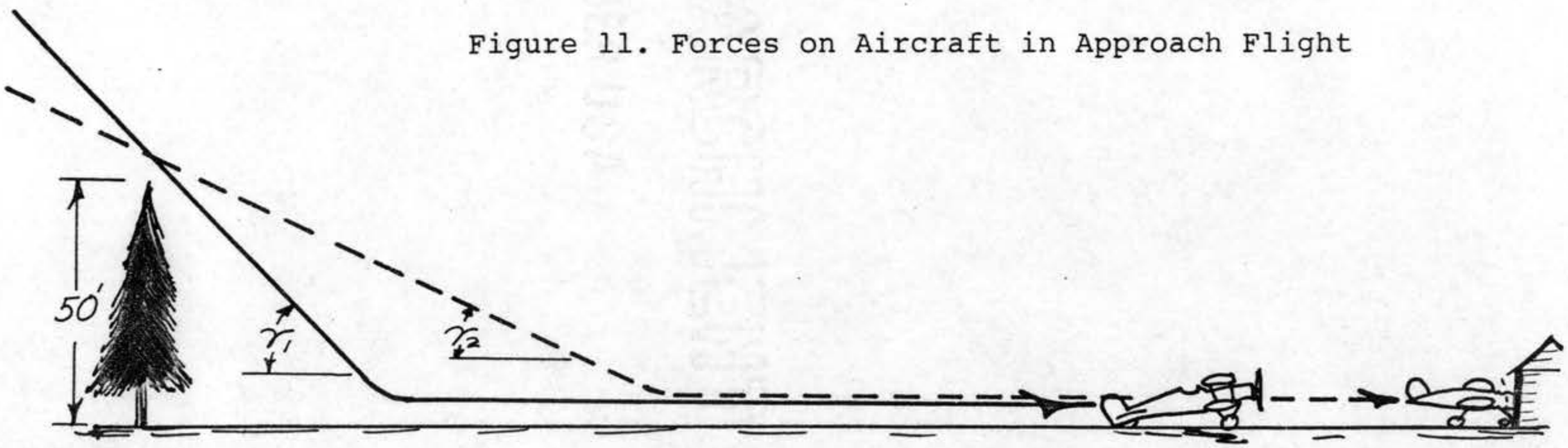

Figure 12. Effect of Approach Angle on Landing Distance

for approach flight or could be reduced for take-off and climb. Clements used the model shown in Figure 13. Both the angle of incidence of the symmetrical-airfoil end-plates and the angle of deflection of the end-plate flaps could be varied (inboard or outboard). These deflection angles are shown in Figure 14.

Clements' reasoning was a bit vague.

> The portion of the end-plate above the wing is deflected to give a reduced pressure on the inboard side of the plate, and the portion below the wing is deflected to give an increased pressure on the inboard side. In this way the force distribution of the wing is extended. The vortex flow of the wing tip is replaced by the vortex flow of the plates, or, in effect, the wing aspect ratio is increased.
>
> If, on the other hand, an increase in drag is desired, the end-plates are deflected in a manner opposite that described above. The end-plates will not supplement the wing lift distribution. The induced drag will not be reduced and will perhaps be increased because of a more rapidly diminishing lift distribution in the region of the end plates (7).

A more rigorous analysis of end-plate action may be considered. The following visualization of the vortex pattern was suggested by Mangler (29). Figure 15 shows the lifting wing represented by a horseshoe vortex. The downwash velocity at any station (on the span) at a distance y_1 inboard of the wingtip is $w = \frac{K}{y_1}$.

The presence of end-plates on the wing will change the pattern of the horseshoe vortex to that of Figure 16. If the end-plates are symmetric (2h high), the strength of each of the trailing vortices will be one-half the strength of the bound vortex. Then, the downwash velocity

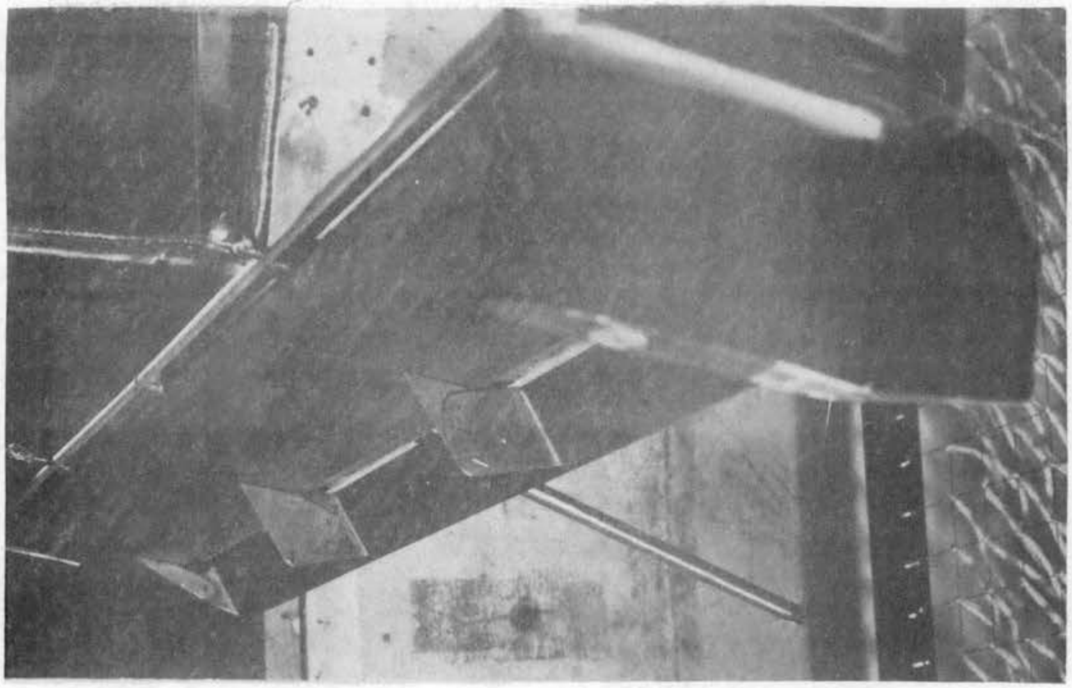

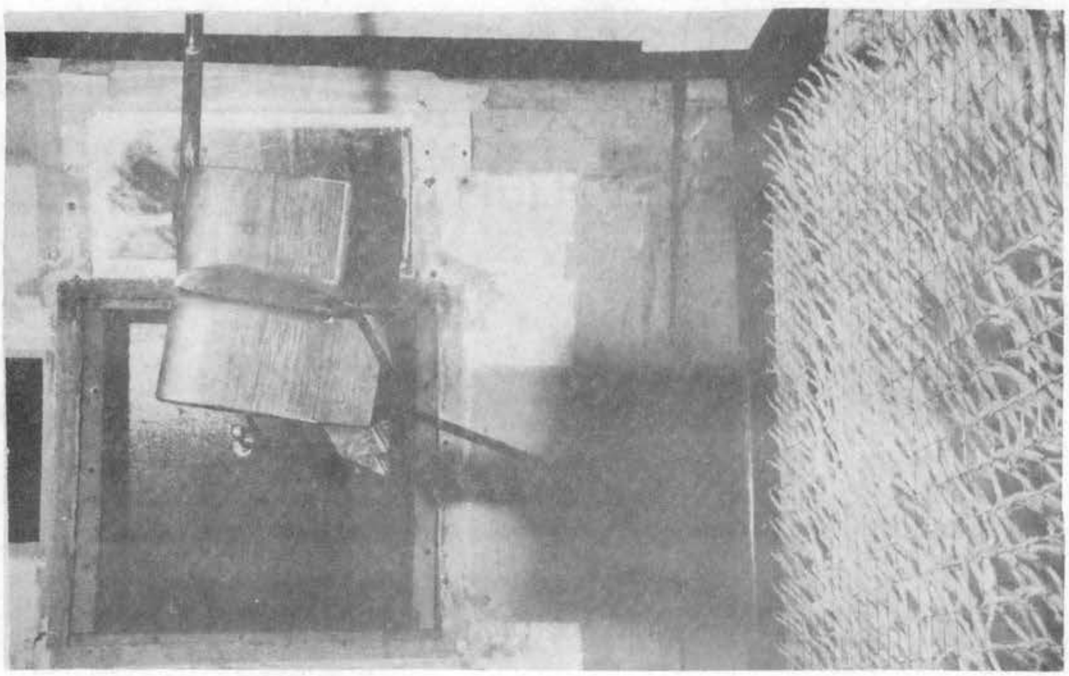

Figure 13. Clements' Variable Geometry End-Plates

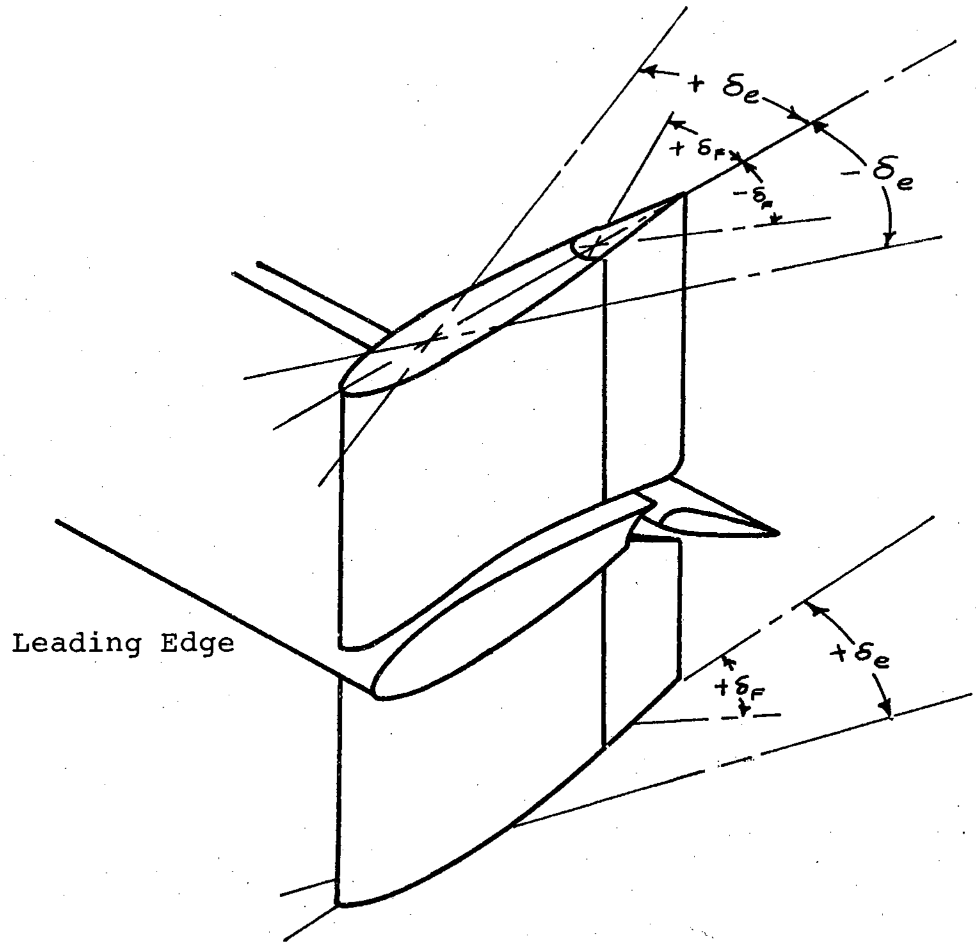

δ_f End-Plate Flap Deflection

δ_e End-Plate Deflection

\+ Increase Drag

− Decrease Drag

Note that for a given deflection sign the deflections above and below the wing are opposite.

Figure 14. Deflection Nomenclature for Clements' End-Plates

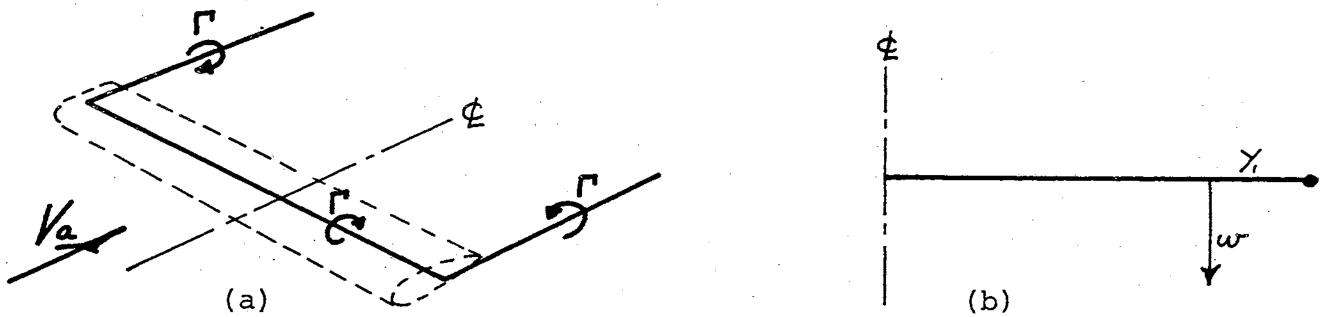

Figure 15. (a) Horseshoe Vortex Representing Lifting Wing
(b) Downwash at Distance y_1 Inboard of Wingtip

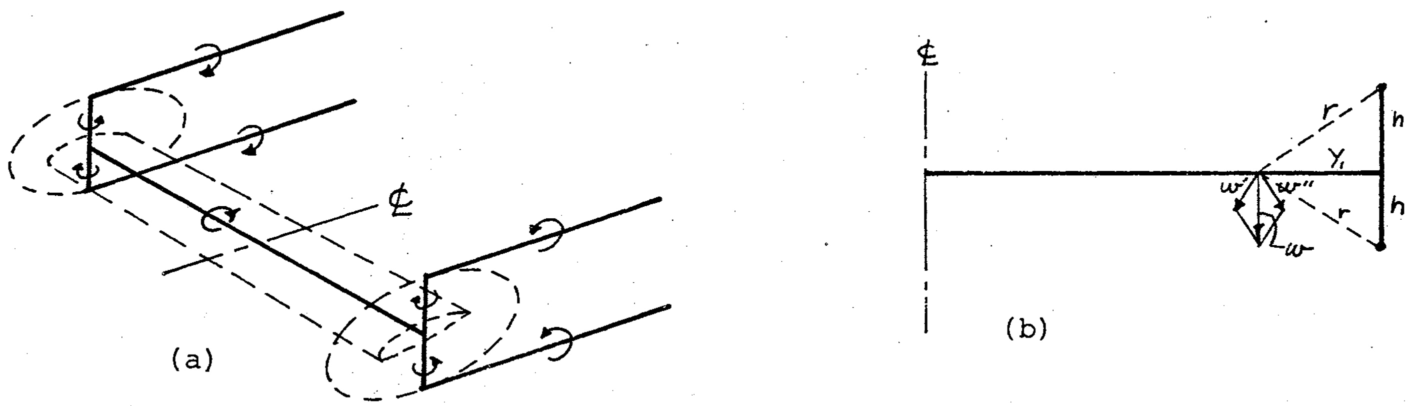

Figure 16. (a) Vortex Pattern Simulating Wing with End-Plates
(b) Downwash Produced by Wing with End-Plates

at the station of distance y_1 inboard of the wing tip is:

$$w' = w'' = \frac{K/2}{r} = \frac{K}{2\sqrt{y_1^2 + h^2}}$$

$$w_e = \sqrt{(w')^2 + (w'')^2} = \sqrt{\frac{K^2}{4(y_1^2 + h^2)} + \frac{K^2}{4(y_1^2 + h^2)}}$$

$$= \frac{K}{\sqrt{2(y_1^2 + h^2)}}$$

(The subscript e refers to the case <u>with</u> end-plates.)

$$\frac{D'_i}{L'} = \frac{w}{V_a} \quad ; \quad \frac{D'_{i_e}}{L'} = \frac{w_e}{V_a}$$

For a given L':

$$\frac{D_{i_e}'}{L'}\,\frac{L'}{D_i'} = \frac{w_e}{V_a}\,\frac{V_a}{w} = \frac{K}{\sqrt{2}\,\sqrt{y_1^2 + h^2}}\,\frac{y_1}{K}$$

$$\frac{D_{i_e}'}{D_i'} = \frac{Y_1}{\sqrt{2}\,\sqrt{y_1^2 + h^2}} = \frac{1}{\sqrt{2}\,\sqrt{1 + (h/y_1)^2}}$$

This ratio, D_{i_e}'/D'_i is always smaller than 1.0. Note that as the height, h, of the end-plates increases, the value of D_{i_e}' decreases. The limiting case is, of course, that of infinite end-plates ($h \to \infty$) in which case the induced drag approaches zero. This flow is, then, two-dimensional.

In the consideration of a vortex sheet instead of a single vortex filament, the reasoning is identical since the result of each trailing vortex filament within the sheet is the same as that of the single vortex. Thus, the cumulative effect of all the vortices in the vortex sheet will have the same trend. The presence of a neutral end-plate decreases the induced drag.

The symmetrical airfoil (or a thin flat plate) will produce side-forces directed inboard on the end-plate above the wing and outboard below the wing. Examination of the pressure field tends to confirm this conclusion (see Figure 17).

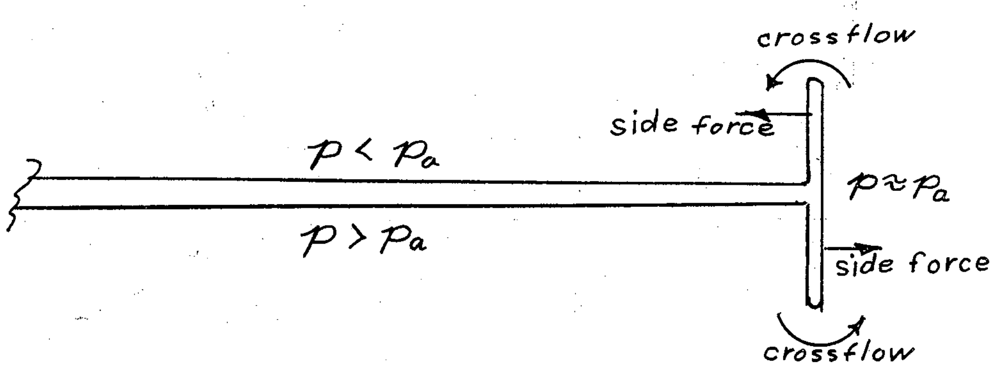

Figure 17. Side Forces on Neutral End-Plates

It will be noted that these sideforces are in the direction specified by Clements (7) for the reduction of wing induced drag.

Figure 18 contrasts the downwash pattern for an

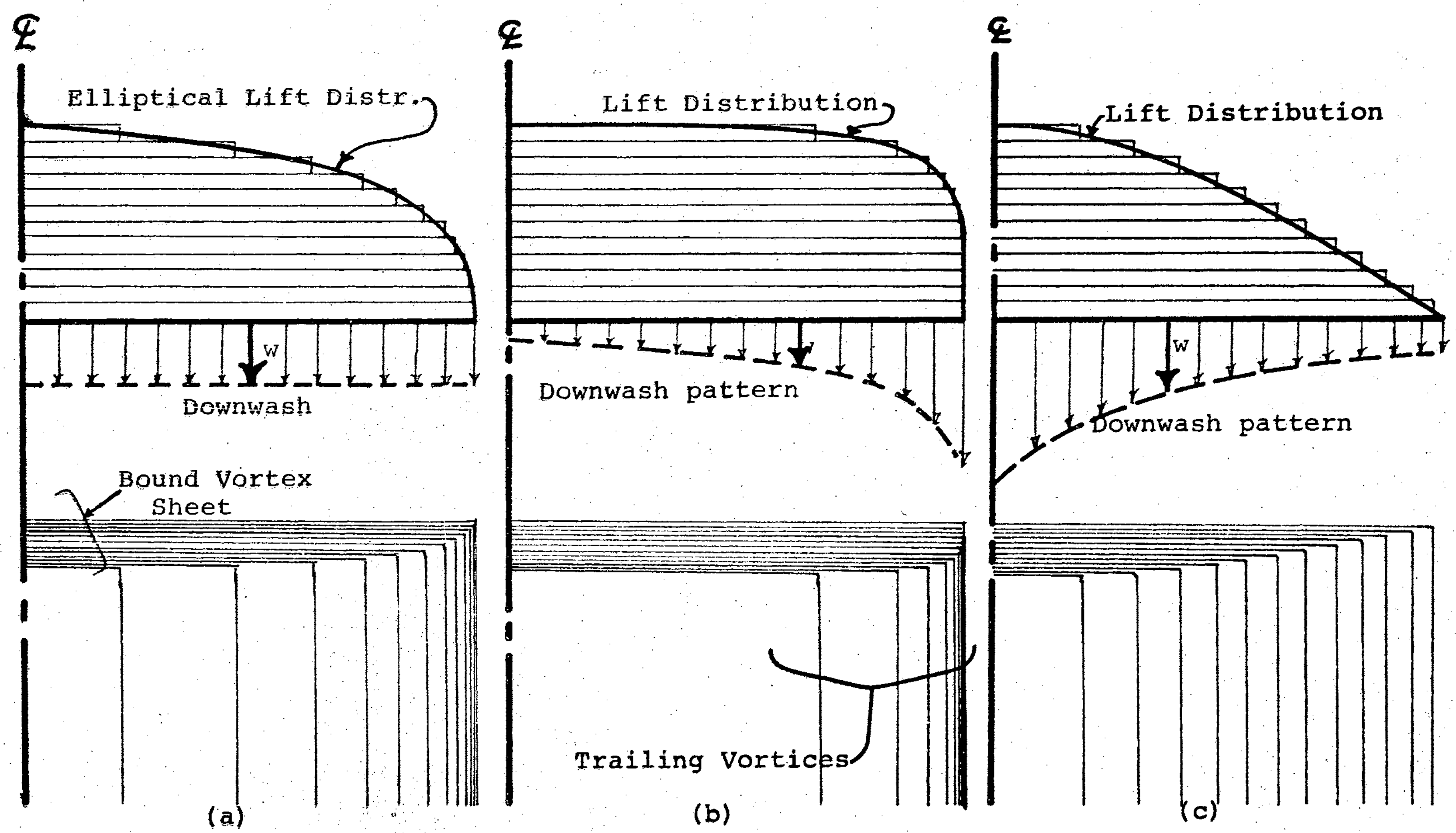

Figure 18. Lift Distribution and Pattern of Shed Vortices

elliptically-loaded wing (a) with wings in which the lift had been shifted outboard (b) or inboard (c). For ease in visualization, these wings have been approximated, in each case, by a finite number of trailing vortices. At any spanwise station, the downwash due to a single trailing vortex may be obtained by integrating the Biot-Savart equation from 0 to ∞, giving $w = \frac{\Gamma}{4 \pi n}$. Then the downwash at the station due to all the trailing vortices is $\sum_{i=1}^{\infty} \frac{\Gamma}{4 \pi n_i}$; n is the spanwise distance to the trailing vortex.

Shifting the trailing vortex strength outboard decreases the inboard downwash and decreases the average downwash velocity. The spanwise position of the rolled-up vortex will also move outboard. The decrease in average downwash velocity causes a corresponding decrease in the induced drag. Shifting the load inboard increases the average downwash, increases the induced drag, and moves the rolled-up vortex inboard. These statements may be summarized:

Direction of Wingloading Shift	Average Downwash Velocity	Vortex Span	Induced Drag
Inboard	Increases	Decreases	Increases
Outboard	Decreases	Increases	Decreases

This shifting of lift distribution may be done in a variety of ways:

Wing twist - (wash-in and wash-out)

Changing of airfoil section

Flap deflection.

It is well-known that wash-out (decreasing the angle of attack toward the tip) increases the drag of a wing.

As stated above, Clements proposed shifting the lift distribution (and, thus affecting the induced drag) by using adjustable end-plates. His model is shown in Figure 13. It consisted of an aspect ratio 5 wing of Clark-Y section equipped with full-span slots and full-span 30% chord slotted flaps. In all tests, the flaps were deflected 50 degrees because Clements was particularly interested in the landing and take-off configurations (high C_L). The end-plates had an NACA 0012 section and were equipped with 30% chord plain flaps. The end-plates had a square planform; the end-plate chord equaled the wing chord and the end-plates extended one-half chord above the wing and one-half chord below the wing.

The incidence of the end-plates was varied by rotating the end-plate above a vertical axis through the end-plate quarter-chord. Also the end-plate flaps were deflected. The sign convention is shown in Figure 14. The tests were performed at a Reynolds Number of 350,000.

Several values of end-plate and flap deflections were investigated. The results of the best combinations are presented in Figure 19. Values abstracted from these results are given in Table II.

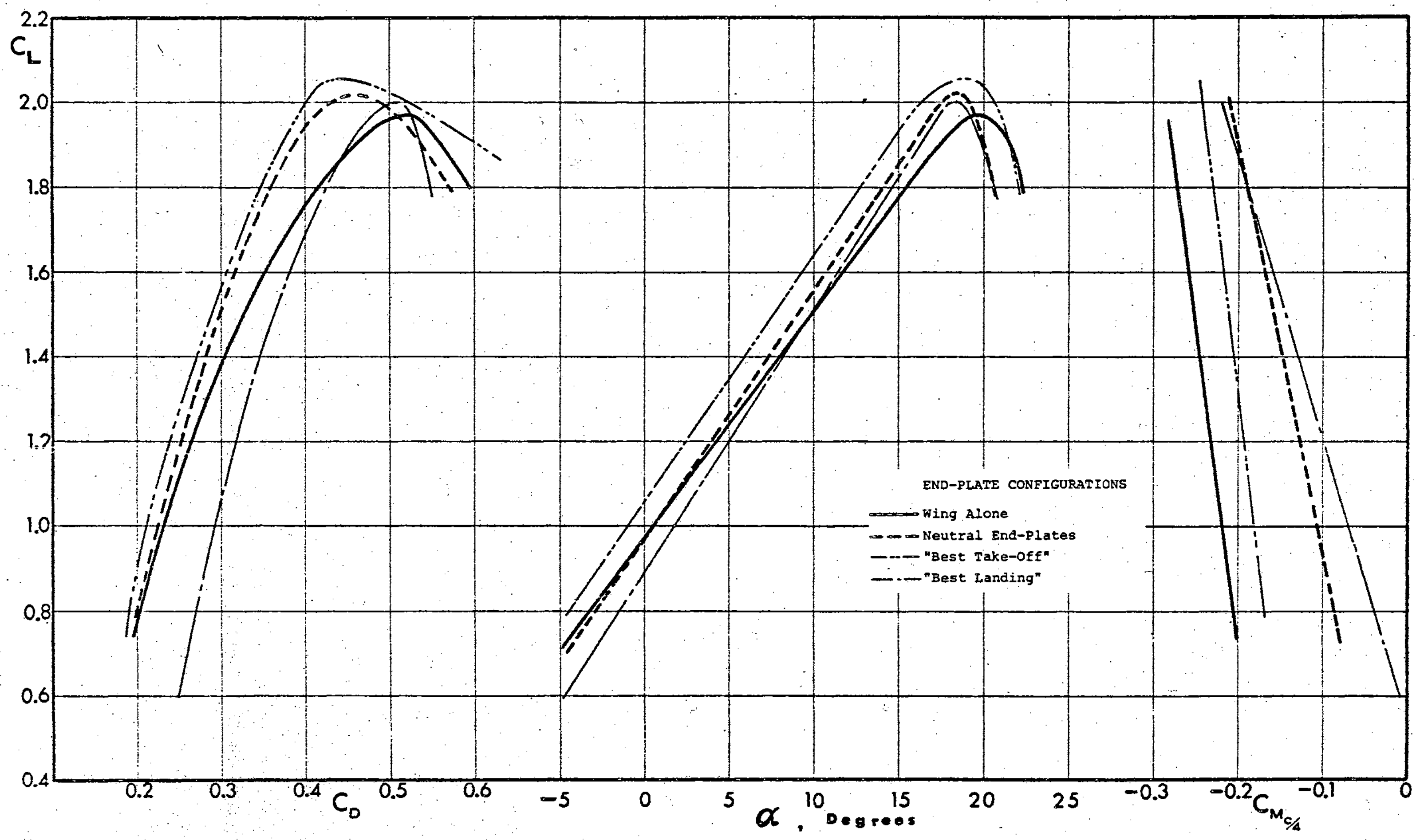

Figure 19. Wing Characteristics With Adjustable End-Plates

TABLE II

CANTED ADJUSTABLE END-PLATES

	C_L	C_D	α	C_M	dC_M/dC_L
Wing alone	1.4	0.308	8.2	-0.246	-0.068
End-Plate and end-plate flap neutral	1.4	0.284	7.4	-0.149	-0.101
End-Plate deflected -5° end-plate flap neutral	1.4	0.269	6.0	-0.205	-0.060
End-Plate neutral, end-plate flap at +30°	1.4	0.345	8.3	-0.128	-0.148

Examination of these results gives credence to Clements' statement that "Canted Adjustable End-Plates can be used to control the drag of wings. The drag can be increased or decreased depending upon the end-plate or end-plate flap deflection" (7). This method of constructing end-plates appears quite promising.

However, analysis of the results, in the same manner as employed for the standard end-plates previously, shows that the canted adjustable plates are not as good as they appear to be. Data from Figure 19 were used in plotting C_D vs C_L^2 in Figure 20. The principal results are tabulated in Table III. Also included in Table III are results for an "Extended Wing" which resulted from extending the span of the wing, instead of using end-plates, by

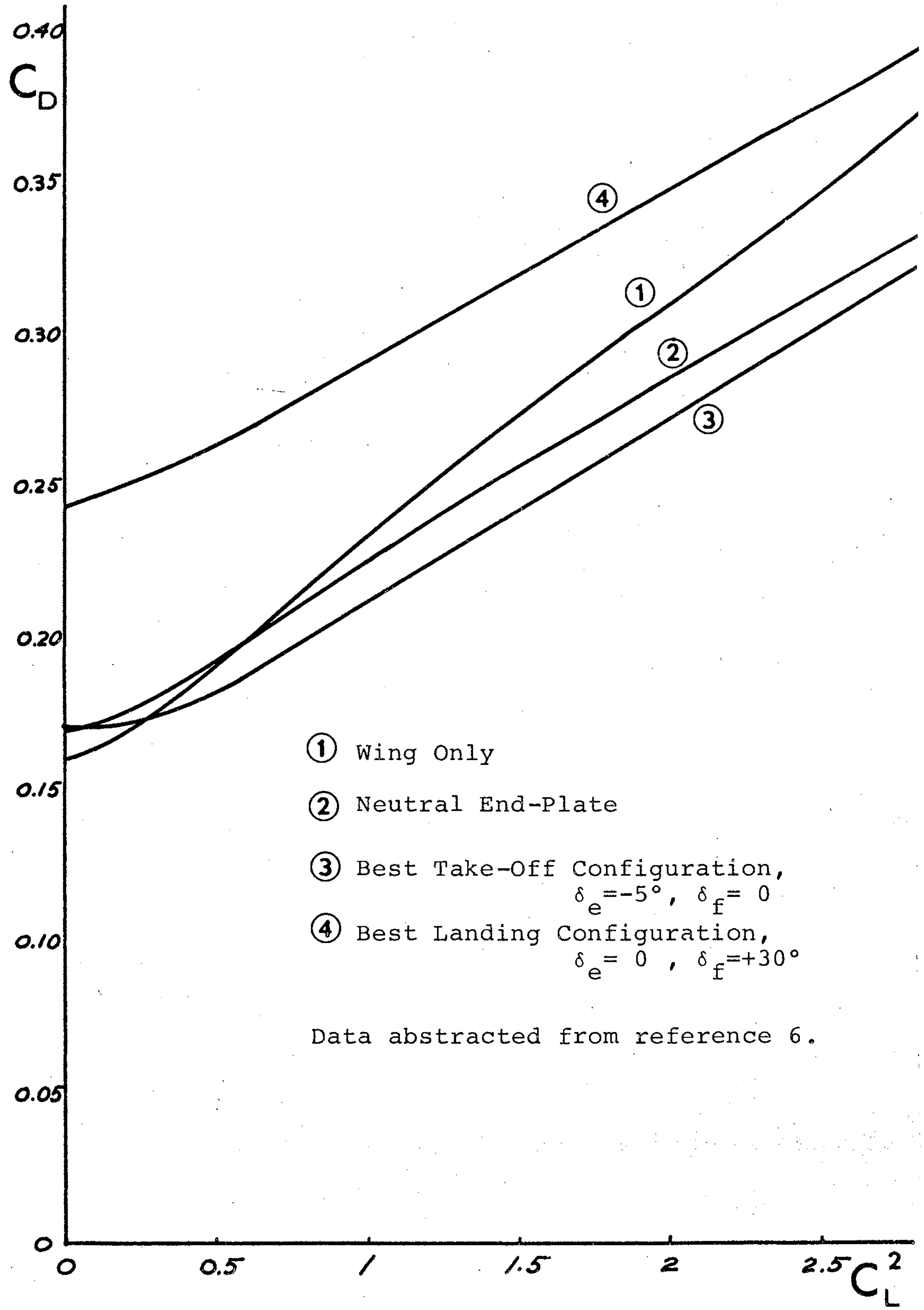

Figure 20. Drag of Adjustable End-Plates

TABLE III

SUMMARY OF WING PERFORMANCE WITH CLEMENTS' CANTED ADJUSTABLE END-PLATES

Configuration	$C_{L_{max}}$	C_D Equation	e_w	Effective Aspect Ratio	D/L at $C_L = 1$
Basic Wing	1.97	$C_D = 0.155 + 0.077C_L^2$	0.828	4.14	0.234
Wing with Neutral End-Plates	2.01	$C_D = 0.167 + 0.059C_L^2$	1.08	5.40	0.225
"Best Take-off" Configuration	2.055	$C_D = 0.158 + 0.058C_L^2$	1.09	5.46	0.212
"Best Landing" Configuration	2.0	$C_D = 0.239 + 0.055C_L^2$	1.162	5.81	0.28
Extended Wing (no end-plates)	1.97	$C_D = 0.155 + 0.055C_L^2$	0.82	5.64	0.200
Extended Wing + Drag Brake	1.97	$C_D = .0.239 + .055C_L^2$	0.82	5.64	0.294

adding the same area to the wingtips. The actual aspect ratio of this extended wing would be 7.0. The last configuration in Table III is the extended wing combined with a retractable flat-plate drag brake, having an area of about 7% of the wing area.

Table III shows that this higher-aspect-ratio-extended-wing with the drag brake retracted would produce lower drag than the "Best take-off Configuration" for take-off and climb. With the drag brake extended, the drag of the "Best Landing Configuration" is exceeded.

Thus, it appears that even with this most promising of the various arrangements of end-plates, the additional area could have been used more effectively in the form of extensions of the wing lifting surface. Improvements in effective aspect ratio must come from other schemes, such as the use of wingtip rotors described in the next chapters.

CHAPTER III

WINGTIP-MOUNTED PROPELLERS

As reviewed in the previous chapter, a myriad of fixed and variable-goemetry end-plates have been proposed but with little effectiveness. The exception to this statement is the combination of end-plates with some method of circulation-control producing high values of C_L, particularly when forced to use wings of low geometric aspect ratio.

Rather than continue to manipulate wing geometry to approach two-dimensional flow it would seem logical to use some energy source for the task of directing the flow. The most obvious source of energy is the main aircraft powerplant. This paper will be restricted to propeller-driven aircraft -- the propellers being driven by piston engines or by gas turbines.

The purpose is to determine whether the engine-driven propellers which propel the aircraft can, at the same time, be used to control the wing loading and the downwash and drag of the wing.

Objectives and Proposed Solution

The objectives, previously set forth, of controlling the wing loading and the downwash are:

a) High $C_{L_{max}}$

b) Low values of induced drag (for take-off and climb).

c) High values of induced drag (for approach and landing).

To these highly desirable characteristics should be added the requirements that the system for attaining these ends should:

1. Add no weight or structural penalty.
2. Add no additional profile drag increment.
3. Add no complexity to the control of the aircraft.

These requirements can be met by placing the propellers which propel the aircraft at the wingtips. The engines would be mounted in pods, or nacelles, fitted to the ends of the wing.

Possible advantages of such an arrangement include:

1. The rotational component of the propeller slip-stream is available for amplifying or attenuating the wing vortex system. This component has, heretofore, been considered the result of lost energy.
2. The propellers are necessary for propulsion of the aircraft, i.e., this is not a case of adding a piece of equipment or structure;

rather, it is a case of locating it to best advantage.

3. Placing the engines and propellers at the wing-tips will relieve the wing shear and bending-moments and could result in a lighter structure.
4. Placing the engines at the wingtips and the fuel in the outboard parts of the wings would greatly improve the safety and chances for crew survival in cases of crash landing.

Possible disadvantages of this arrangement include:

1. Difficulty (or impossibility) of trimming the aircraft for one-engine-out operation.
2. Production of aero-elastic problems created by the changing of the torsional moment of inertia of the wing and the interaction of bending and torsional modes of flutter or vibration.

The main objective of this paper is to report the results of an experimental program designed to test and evaluate the effectiveness of this scheme.

Experimental Investigation

The test program consisted of wind tunnel testing of a wing, with and without propellers mounted at the tip of the wing. These propellers were powered by a motor contained within a streamlined pod at the wingtip.

Model Description

The wing tested is a tapered wing with an aspect ratio of about 8. The dimensions of the model are given in Table IV and Figure 21 is a sketch of the model.

In order to provide a periptery not influenced by the tunnel walls, the test was a reflection-plane test. The reflection-plane was the floor of the tunnel test section as shown in Figures 22 and 23. The wing model that was tested is a hollow, cast magnesium wing having an unbroken taper in thickness ratio and in planform. The wingtip, ailerons, flaps and inserts are mahogany. The model was mounted with no dihedral and with the vertical quarter-chord line collinear with the balance centerline. Figures 22(a) and 23(a) show the wing with standard plain tip installed in the tunnel.

In addition to the plain tip, the model was tested with a wingtip pod. The purpose of the pod is to house an electric motor which serves as drive for the propeller and impeller. The pod is a streamlined body of revolution $19\frac{1}{2}$ inches long with a fineness ratio of 4.6. Figure 22(c) shows the pod with a dummy spinner nose. The spinners of the propeller and the impeller have the same contour.

It was planned to use two propellers in the tests -- one of standard conformation and of relatively high efficiency (high ratio of axial velocity to angular velocity) and the other having fairly high rotational velocity

TABLE IV

MODEL PHYSICAL DIMENSIONS

Wing	
Semi-area	3.992 sq. ft.
Semi-span	4.011 ft.
Aspect Ratio	8.06
Mean aerodynamic chord	0.995 ft.
Airfoil sections	
Root	NACA 23018
Tip	NACA 23012
Twist	None
Flap chord	25% chord
Flap span	62.5% span
Aileron chord	30% chord
Aileron span	25% span
Wingtip Pod	
Length	19½ in.
Maximum diameter	4¼ in.
Frontal area	14.2 sq. in.
Planform area	40.5 sq. in.
Wing semi-span, including pod	4.302 ft.
Wing aspect ratio, including pod	8.78

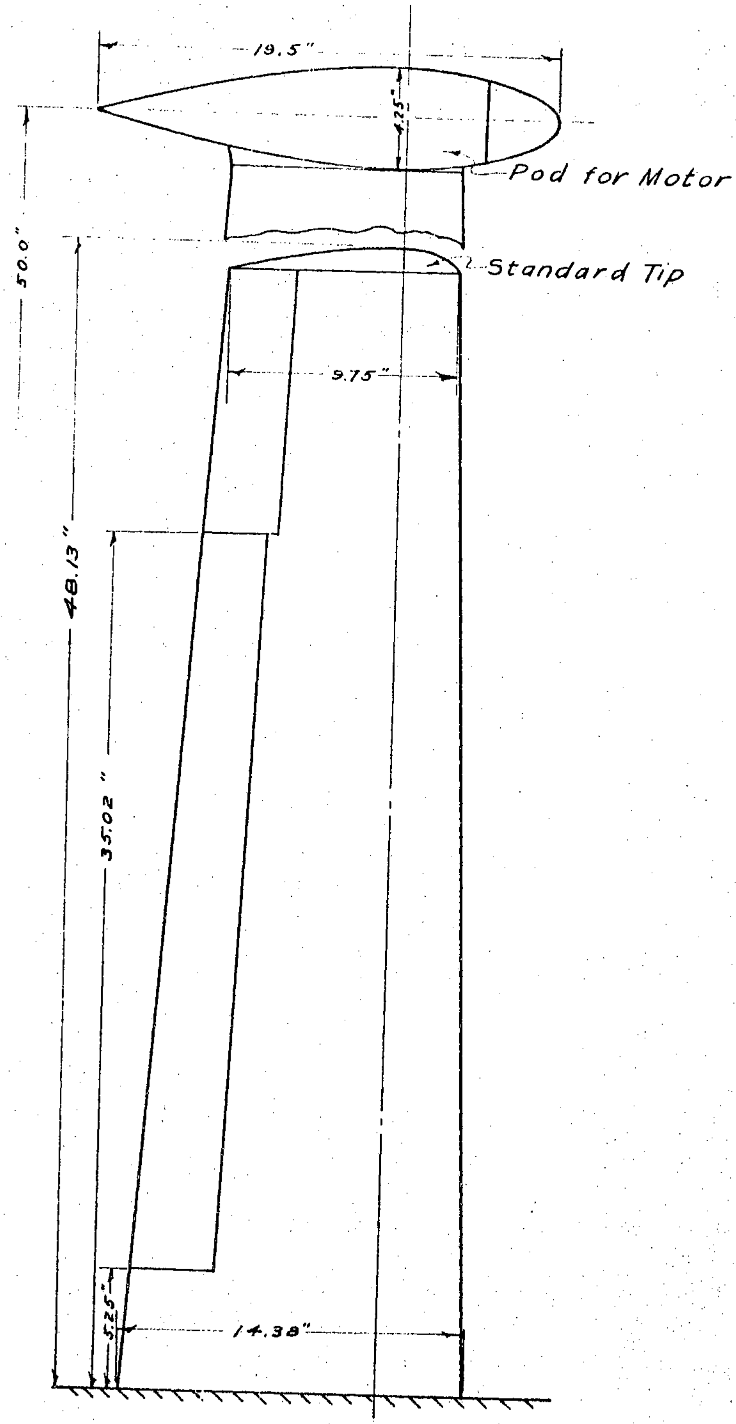

Figure 21. Wind Tunnel Model Showing Alternate Tips

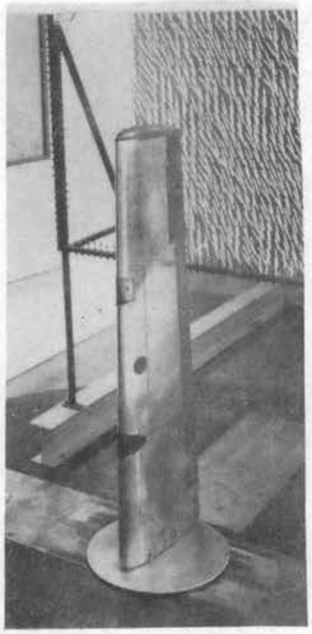

(a) Plain Tip

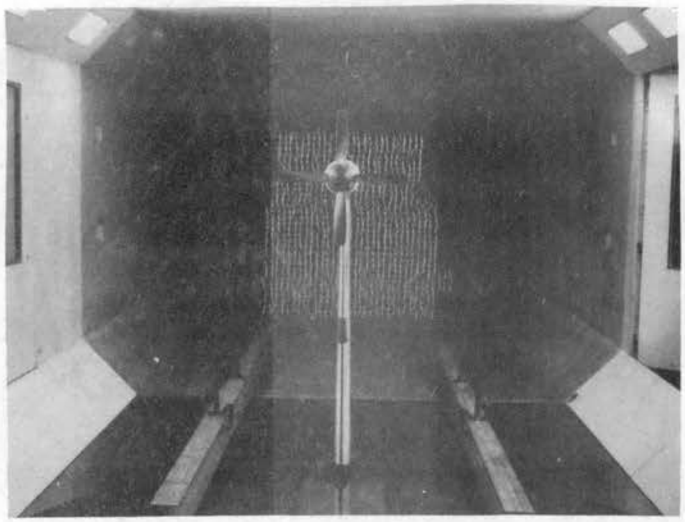

(b) Four-Blade Propeller

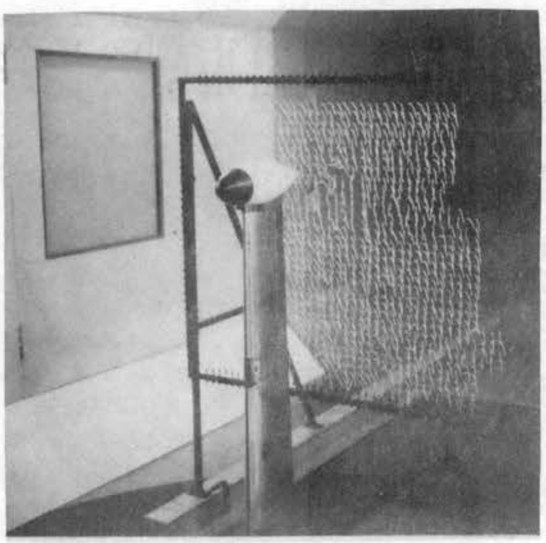

(c) Dummy Spinner

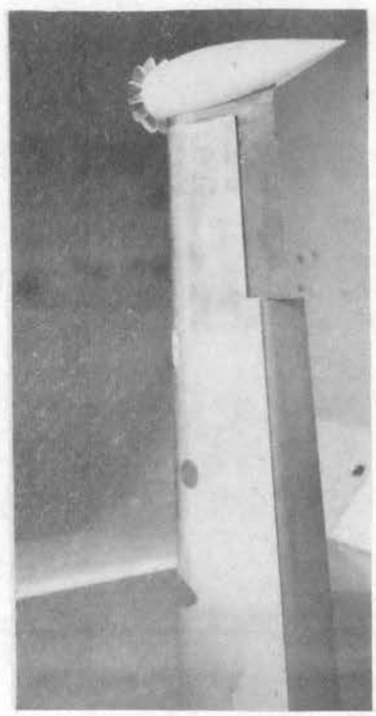

(d) Impeller

Figure 22. Reflection Plane Wing With Various Tip Configurations

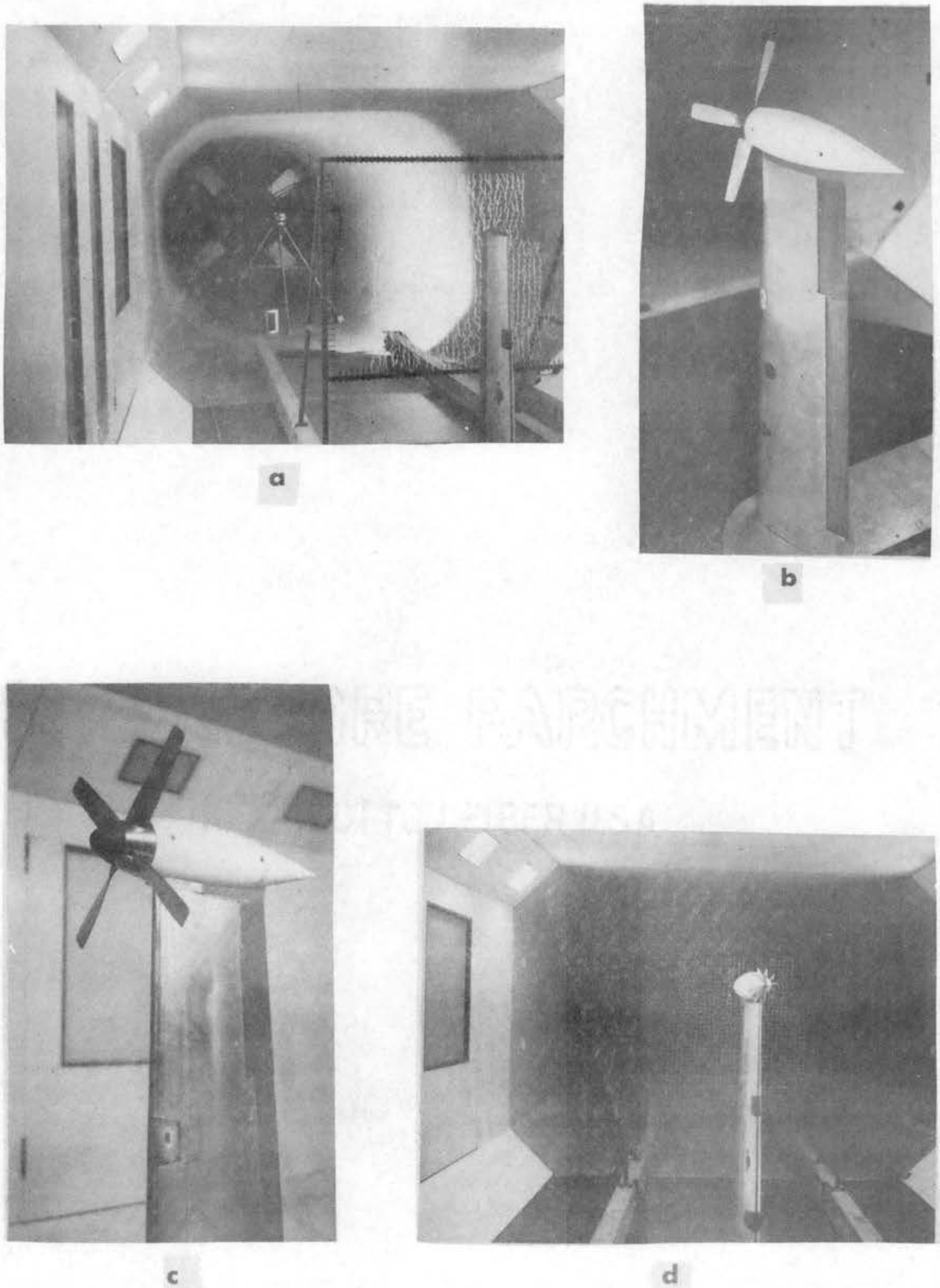

Figure 23. Various Test Configurations of Model

compared to the axial velocity. The purpose in using this second propeller was to obtain data bearing on the observations of Lippisch[1]. He stated that a limitation to the use of a propeller in affecting the wing trailing vortex was the efficiency of the propeller -- about 80% of the energy provides axial acceleration of the air and only about 20% is available to produce rotation with which to supplement or to counteract the trailing vortex and the attendant downwash pattern.

Some years ago, the writer tested, for the Beech Aircraft Corporation, a propeller invented by Tom Quick. This Quick propeller was an impeller similar to that shown in Figures 22(d) and 23(d). Quick maintained that the air would be thrown radially outward producing at the nose of the impeller a region of pressure that would be lower than that which existed on the rear portion of the streamlined housing, producing thrust. The tests indicated that the device does produce thrust, but the propulsive efficiency peaks at less than fifty per cent. This type of propeller was chosen to serve as the inefficient propeller for these tests. The Quick propeller will be referred to as the impeller and the four-bladed propeller will be called the propeller.

---

[1] Alexander Lippisch. Kenneth Razak, in 1965, reported to the writer a conversation on the subject which he had with the famous designer of the German rocket propelled fighter. At that time (about 1956) Lippisch was engaged in O.N.R. sponsored research in V/STOL aircraft.

The impeller is shown on the wing in Figures 22(d) and 23(d); the propeller is shown in Figures 22(b) and 23(b). They are compared in Figure 24.

The impeller has the same basic contour as the propeller spinner. Added to that contour are twelve radial blades having a maximum depth of one inch giving an overall impeller diameter of 5.25 inches. Figure 26 is a drawing of the impeller.

The blade planform and blade sections of the four-blade propeller are shown in Figure 27. This propeller is a right-hand rotation propeller. The pitch angle of the propeller blades was arbitrarily set at 15.5° (at $r/R = 60\%$) using the jig shown in Figure 25. This angle corresponds to a very low pitch. Propeller activity factor is about 90 per blade and the total propeller diameter is 15 inches.

The motor installation is shown in Figure 28. The motor is a synchronous motor rated at 10 horsepower at 12,000 r.p.m. and is three inches in diameter and six inches long. The power source is a variable frequency (0 to 400 cycles/sec.) generator; the frequency of the generated power is varied to change the motor speed. Speed is monitored by beating an induced signal from a loop on the motor shaft against a known input. Figure 29 shows the motor controls including the signal generator, oscilloscope, and TV monitor. As shown in Figure 28, the power leads and tachometer wires, as well as the cooling-water tubing and thermo-couple leads were carried to the

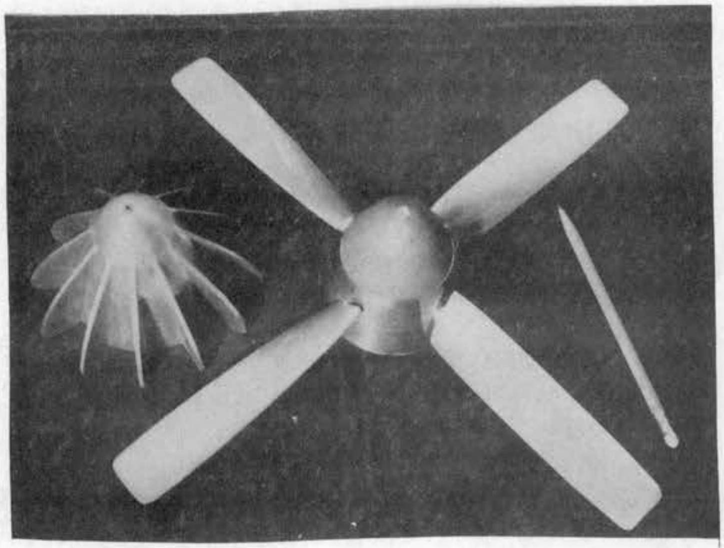

Figure 24. Impeller and Propeller

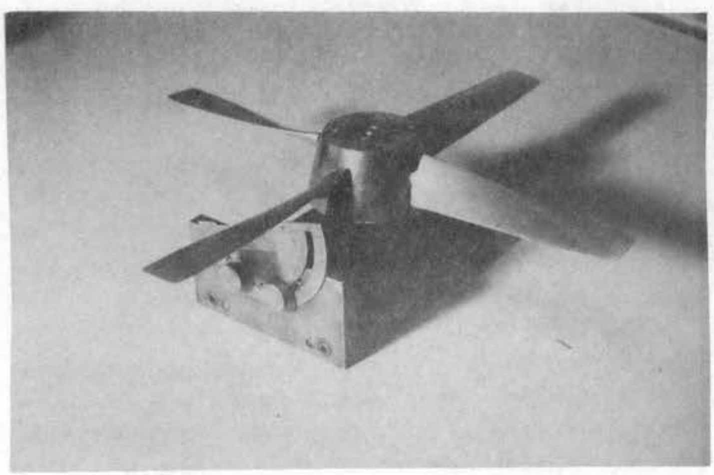

Figure 25. Propeller on Pitch-Angle Jig

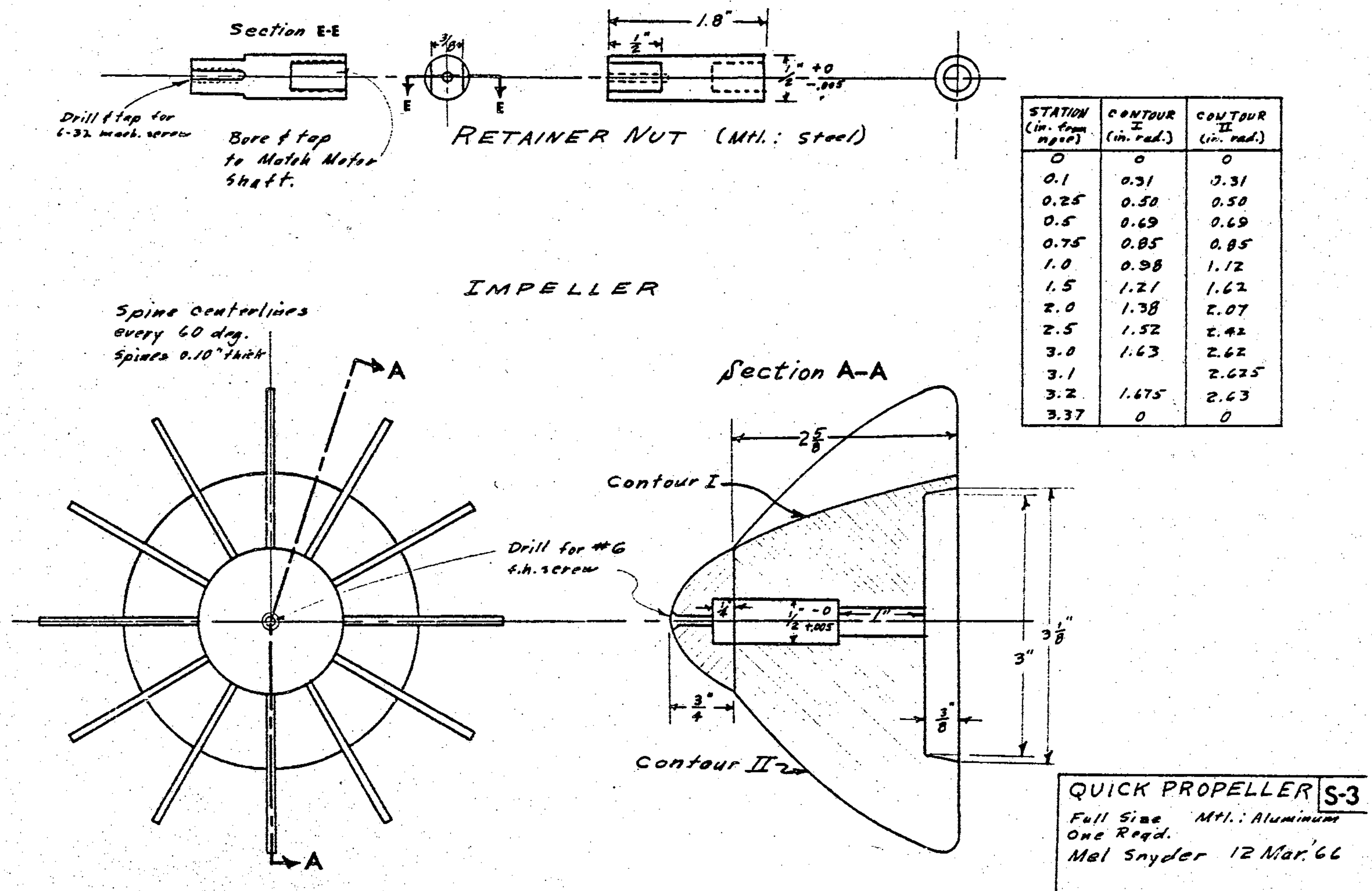

STATION (in. from nose)	CONTOUR I (in. rad.)	CONTOUR II (in. rad.)
0	0	0
0.1	0.31	0.31
0.25	0.50	0.50
0.5	0.69	0.69
0.75	0.85	0.85
1.0	0.98	1.12
1.5	1.21	1.62
2.0	1.38	2.07
2.5	1.52	2.42
3.0	1.63	2.62
3.1		2.625
3.2	1.675	2.63
3.37	0	0

Figure 26. Drawing of Impeller

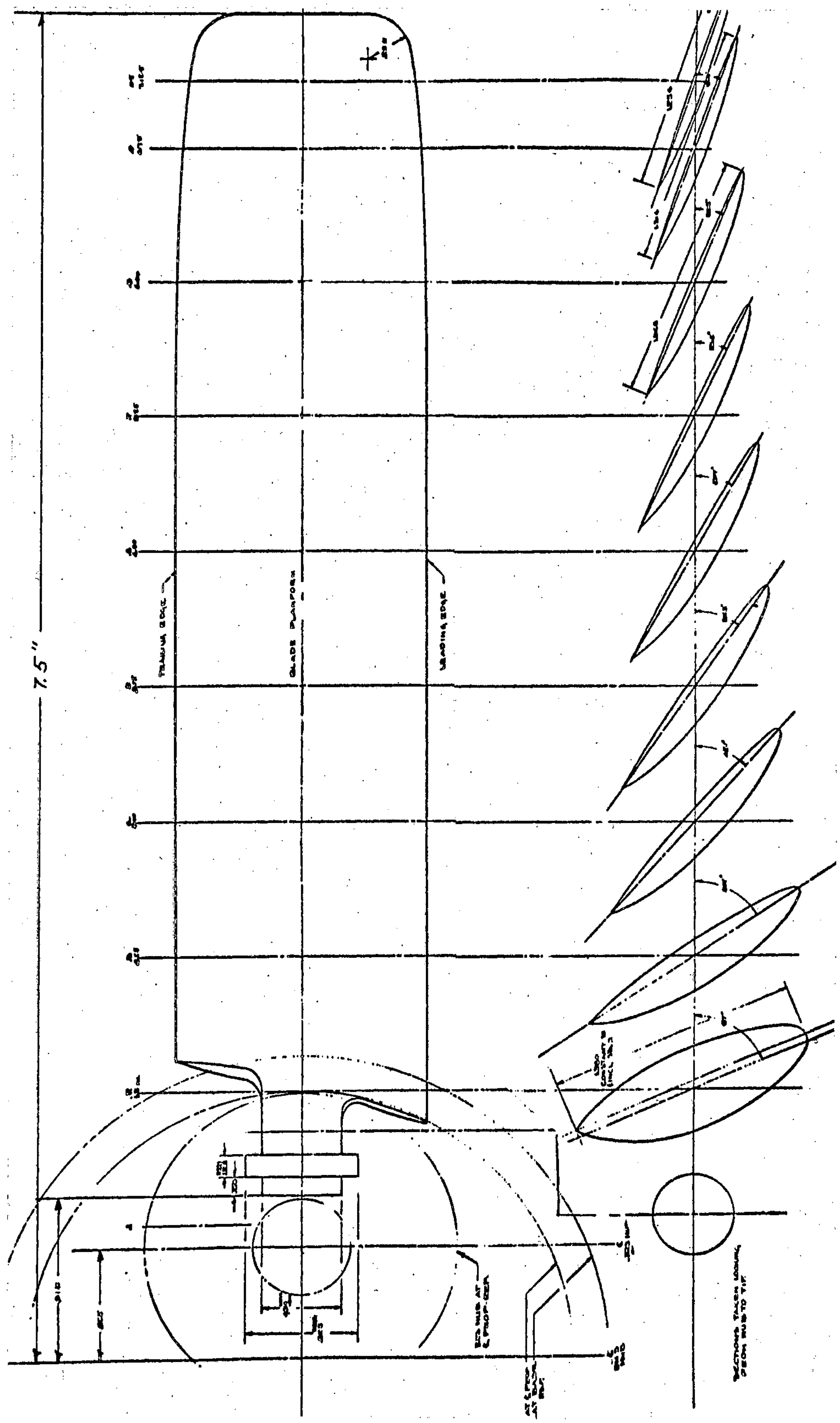

Figure 27. Propeller Blade

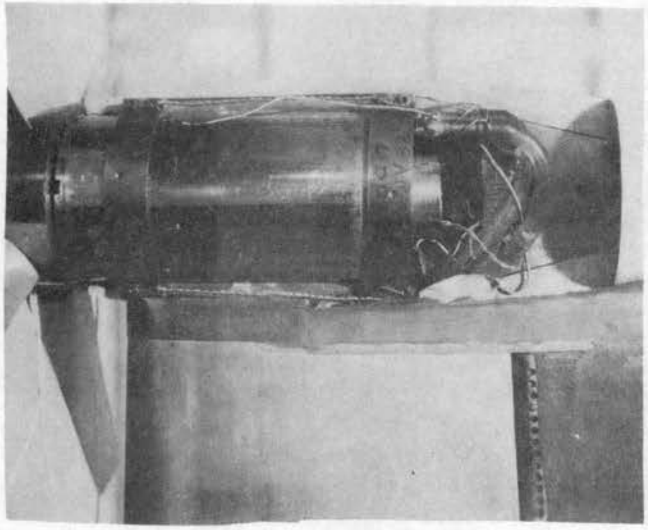

a

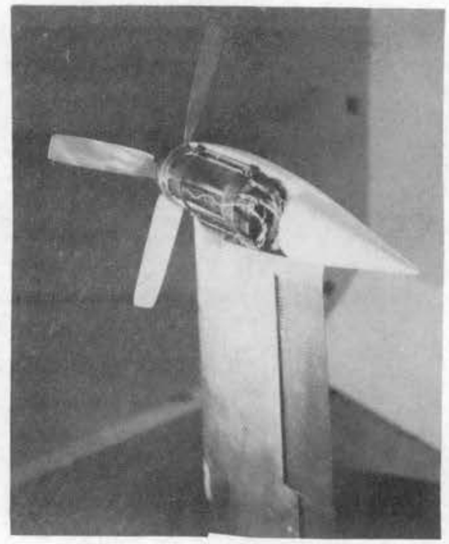

b

Figure 28. Motor Installation

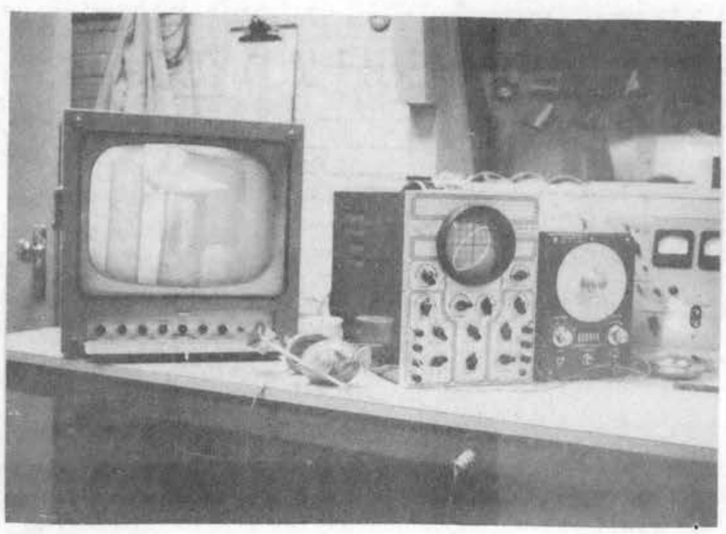

Figure 29. Motor Instrumentation

motor through the hollow wing.

Downstream of the wing, a tuft grid was mounted for the observation of the flow field direction. This grid is shown in Figures 22 (a, b, and c), and in Figure 23(a) the remotely-operated camera can be seen upstream of the tunnel propeller (the camera hood has been removed and is on the floor).

In order to correct the values of lift, drag, and pitching moment observed during the power-on tests, the lift, drag, and moment produced by the propellers was determined using the propeller mount shown in Figure 30.

The dynamic tare was found using the dummy spinner as shown in Figure 30(a). The propellers were operated as shown in Figures 30(b and c). In each case, the mount was rotated through the same angles of attack as those at which the wing had been tested. The propeller speeds were the same as during the wing tests.

Test Program

The test program included the following types of tests and model configurations.

Test Method:

1. Photographs of tuft-grid downstream of the model.
2. Balance measurement of three-components (lift, drag, and pitching moment) through

a

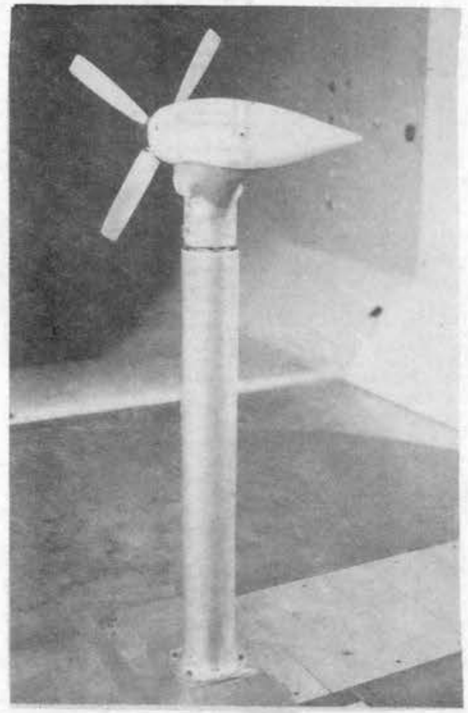

b

c

Figure 30. Determination of Corrections Due to Direct Thurst

range of angles of attack from -10° to +26°.

The tuft grid pictures were taken at nominal angles of attack of 12° and 0°. The flap deflections were either 0 or 40°. These angles were chosen from preliminary balance tests which indicated that the angle of zero lift of the basic wing was approximately zero and at $\alpha = 12°$ the C_L was about 1.0.

Model Configurations:

1. Wing with plain tip (Figure 22(a) and 23(a)).
2. Wing with pod and dummy spinner (Figure 22(c)).
3. Wing with pod and impeller (Figures 22(d) and 23(d)).
    a) Impeller stationary
    b) Impeller turning in the same direction as the wing trailing vortex (two speeds)
    c) Impeller turning in the counter-vortex direction (two speeds)
4. Wing with pod and propeller (Figures 22(b) and 23(b and c)).
    a) Propeller stationary (two positions)
    b) Propeller windmilling (counter-vortex direction)
    c) Propeller turning counter-vortex at greater than windmilling speed

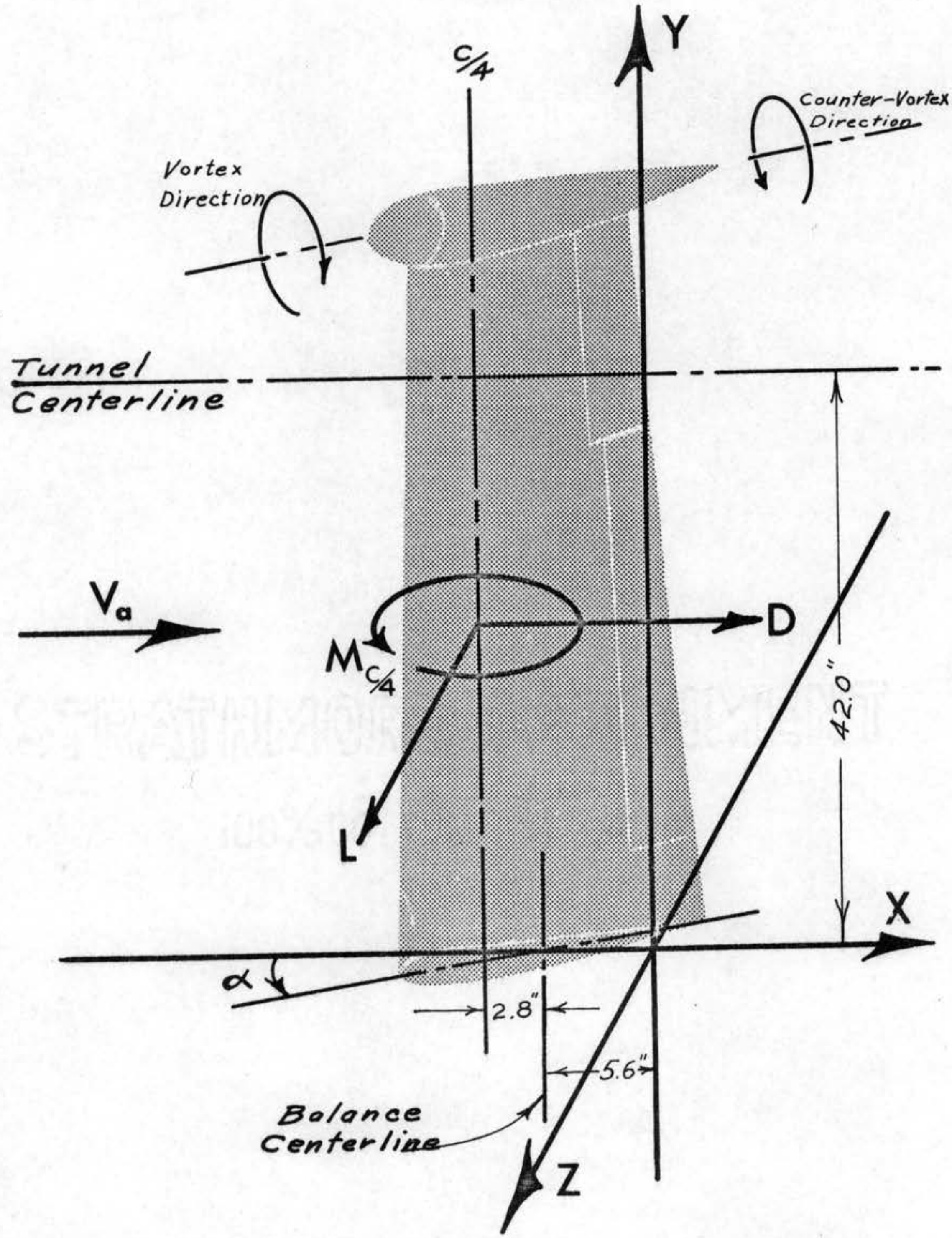

Figure 31. Wind Tunnel Coordinate System

d) Propeller turning counter-vortex at less than windmilling speed

5. Post-mount with pod (full range of α)

   a) Dummy spinner (Figure 30(a))

   b) Impeller (pro- and counter-vortex) (Figure 30(c))

   c) Propeller (3 speeds) (Figure 20(b))

The coordinate system adopted for the test is shown in Figure 31.

Results of the Test Program

Since the experimental results, when presented graphically, are quite bulky, only those figures of primary importance are included in the body of this paper; other results may be found in the Appendix.

Tuft-Grid Results

In order to interpret the results of the tuft grid survey, 140 of the pictures were printed. Figure 32 shows example pictures. These pictures show the flow field in the Y-Z plane at various distances downstream of the model trailing-edge (at the tip). All pictures were taken at a tunnel dynamic pressure of 10 psf. It is apparent that the position of the wingtip vortex core and the flap outboard core can be estimated.

Since the pictures were taken with the grid located at various positions, ranging from x = 6 inches to

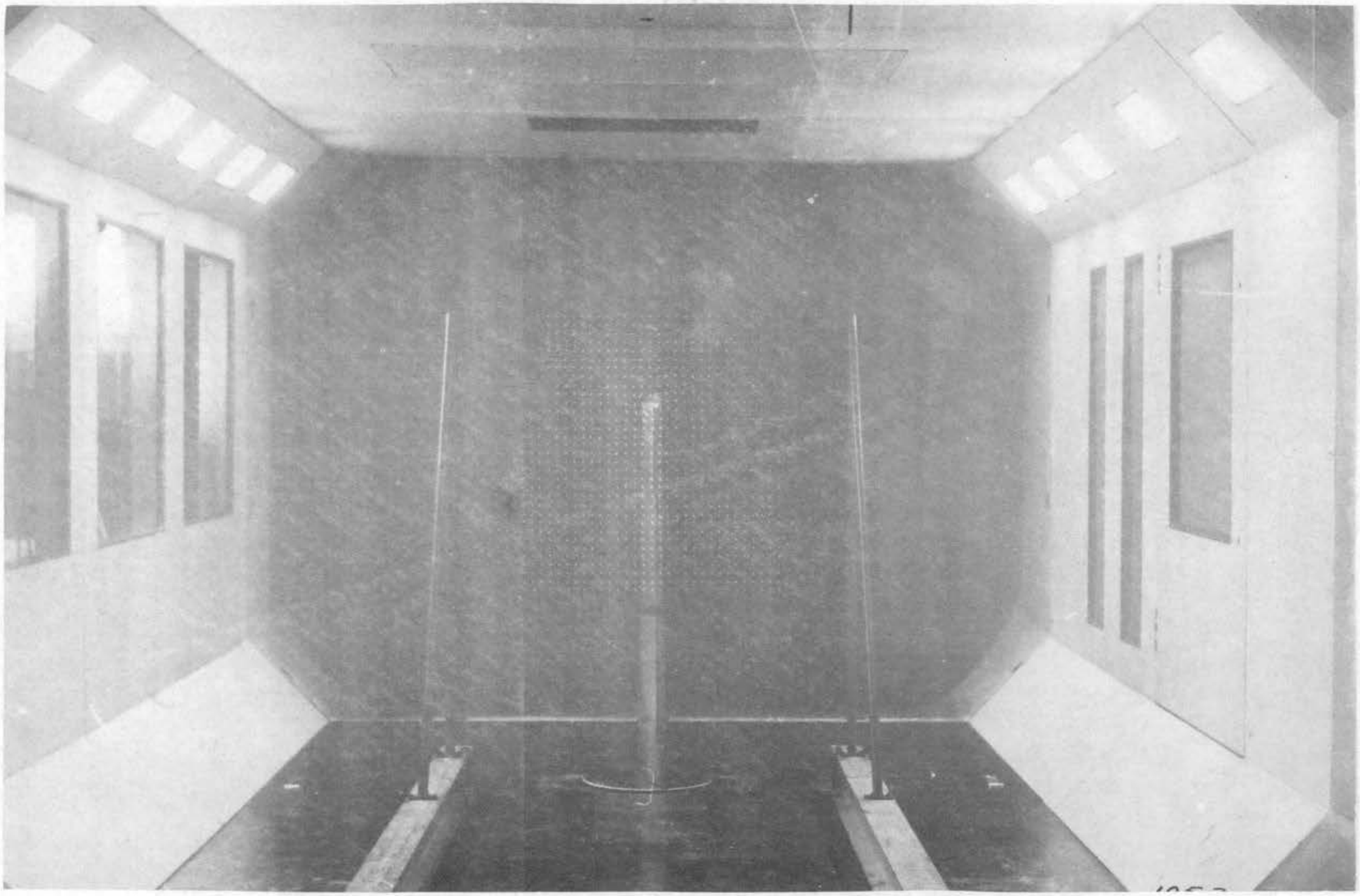

Figure 32. Examples of Tuft-Grid Photographs. (a) Wing with Plain Tip, $\alpha = 12°$, $x = 12$ in.

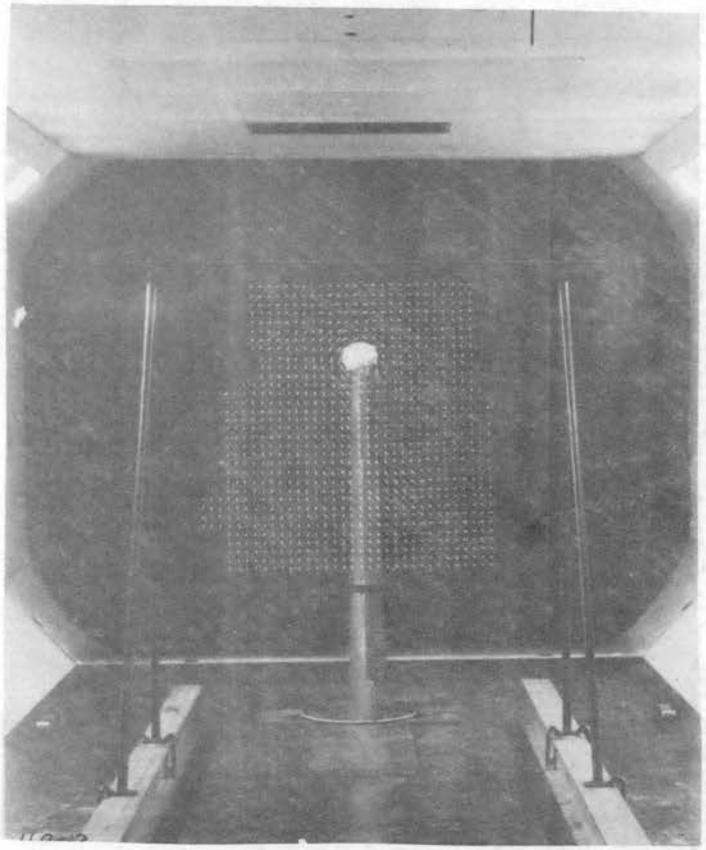

(b) Pod and Dummy Spinner,
$\alpha = 12°$, $\delta_f = 40°$, x = 48 in.

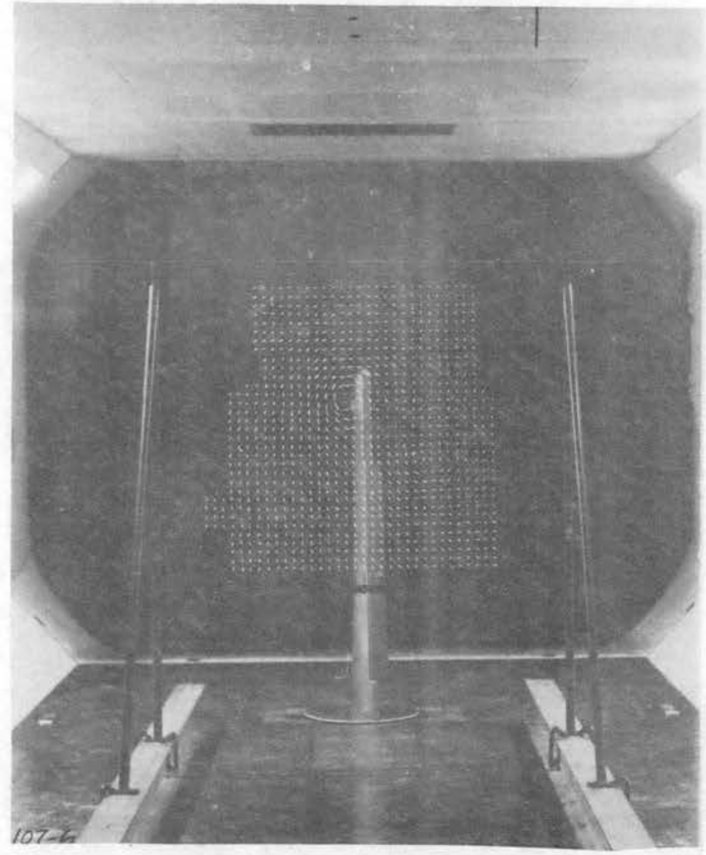

(c) Plain Tip
$\alpha = 12°$, $\delta_f = 40°$, x = 12 in.

Figure 32 (cont.). Examples of Tuft-Grid Photographs

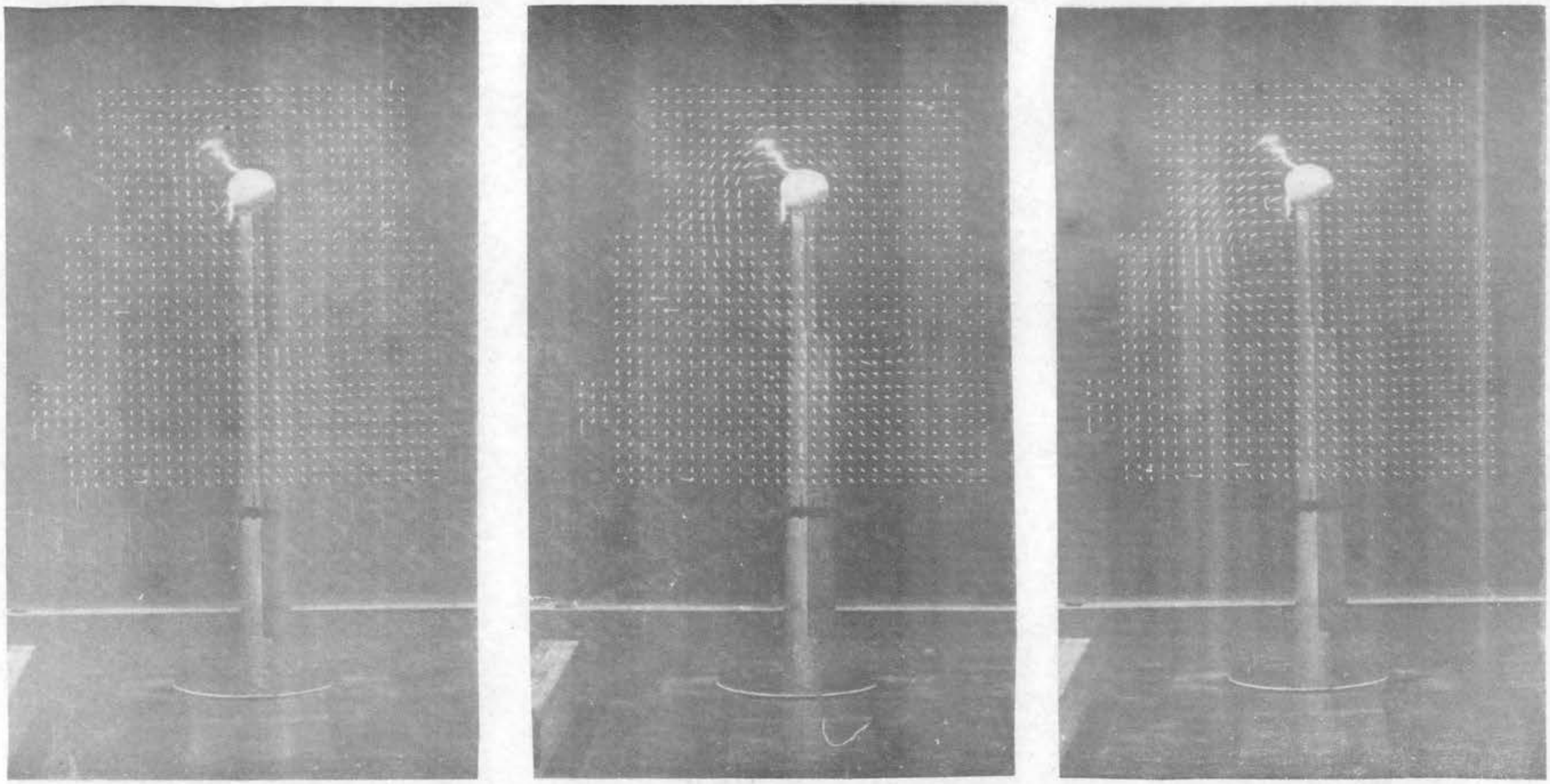

(d) N = 175 rps. (e) N = 122.5 rps. (f) N = 50 rps.

Figure 32 (cont.). Examples of Tuft-Grid Photographs: Wing with propeller, Counter-Vortex Rotation, $\alpha = 12°$, $\delta_f = 40°$, x = 48 in.

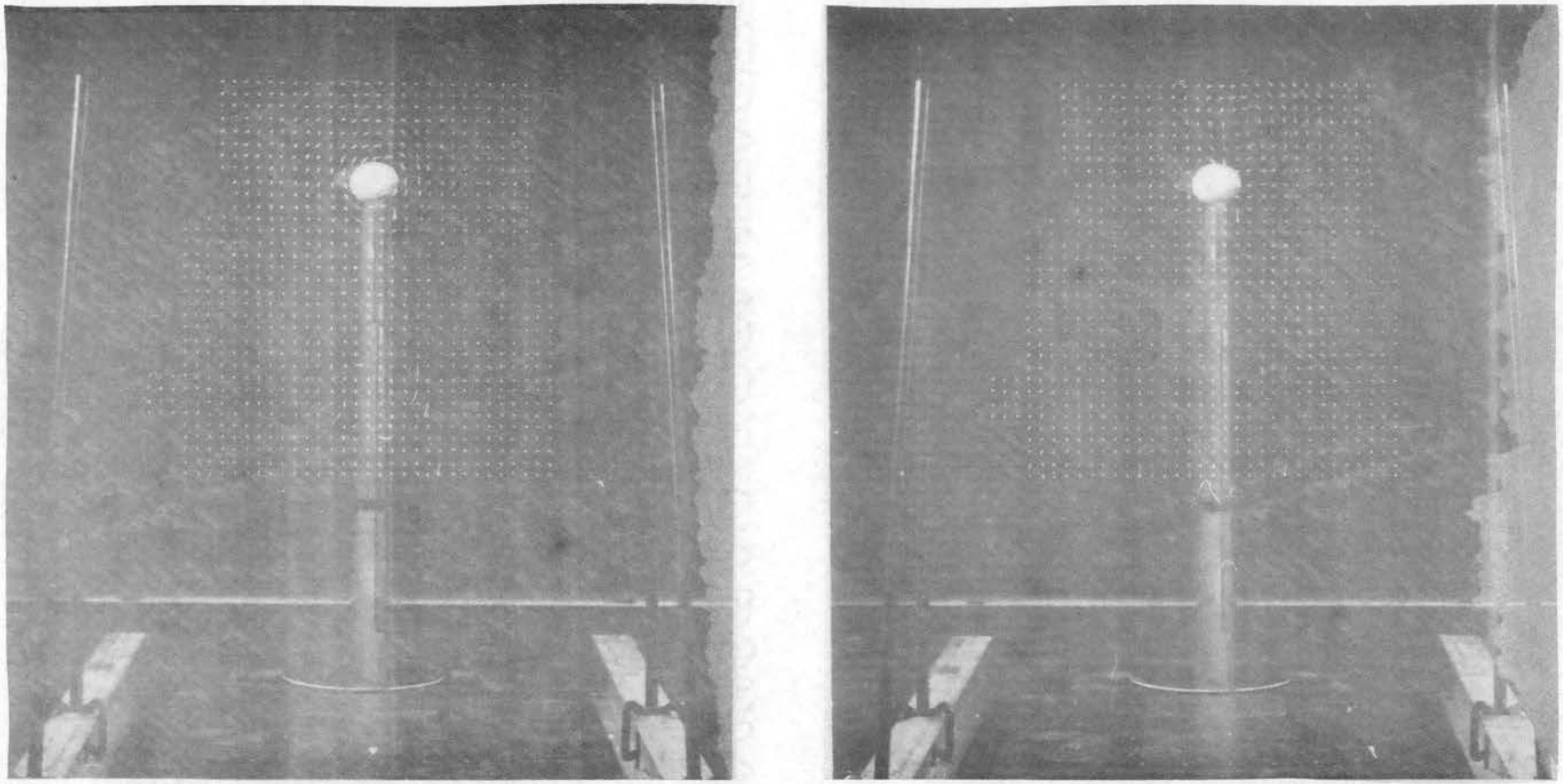

(g) Impeller Stationary

(h) N=175 rps, counter-vortex

Figure 32 (concluded). Examples of Tuft-Grid Photographs. Wing With Impeller, $\alpha = 12°$, $\delta_f = 0°$, x = 48 in.

x = 96 inches, it is possible to estimate the trajectory of the trailing vortex core as it rolls-up. Figure 33 shows the trajectories of three trailing vortices in the X-Y plane. The model configuration is the wing with the impeller installed at the tip; $\alpha = 12°$, $\delta_f = 0°$. With no rotation of the impeller, the vortex-span is 101 inches; counter-vortex rotation shifts the vortex outboard to a vortex-span of 107 inches; vortex-direction rotation reduces the vortex-span to 89 inches. Figure 34 shows these trajectories in the X-Y plane and Figure 35 shows them in the Y-Z plane.

A similar graph is shown in Figure 36 which is the X-Y plane showing the trajectory of the vortex core as affected by the propeller rotation. The largest lateral shift of the trajectory was produced by the rotation of the propeller at less than windmill speed.

Figure 37 shows the position of the center of the vortex core at a distance of one-half wingspan downstream of the trailing-edge for most of the configurations tested. The wing was at an angle of attack of 12° and with the flaps deflected 40°. The following results can be detected:

a) Adding the pod moves the trailing vortex outboard compared to the wing with a standard tip.

b) Counter-vortex rotation of the impeller and counter-vortex rotation of the

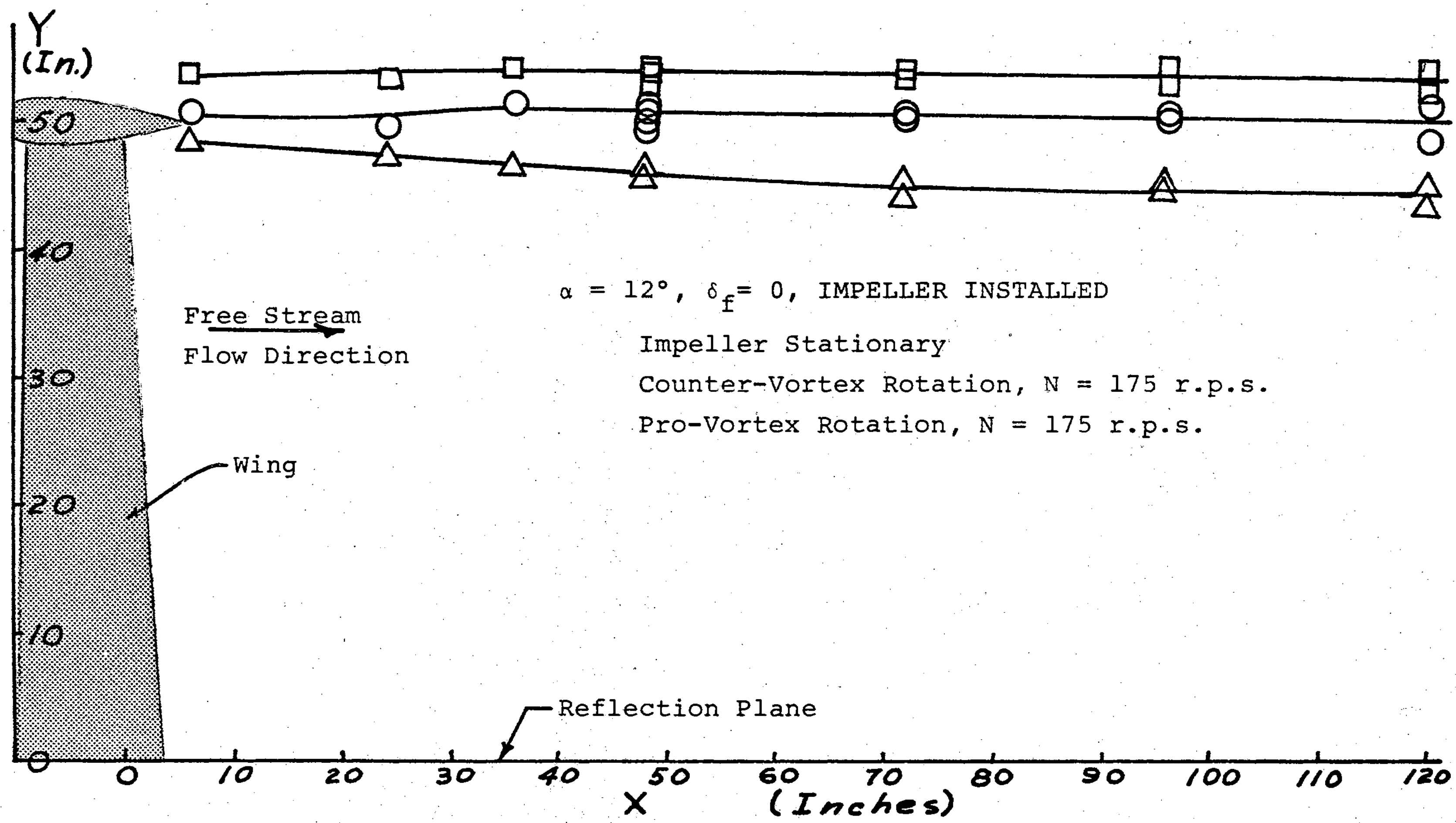

Figure 33. Trailing Vortex Core Trajectory in X-Y Plane

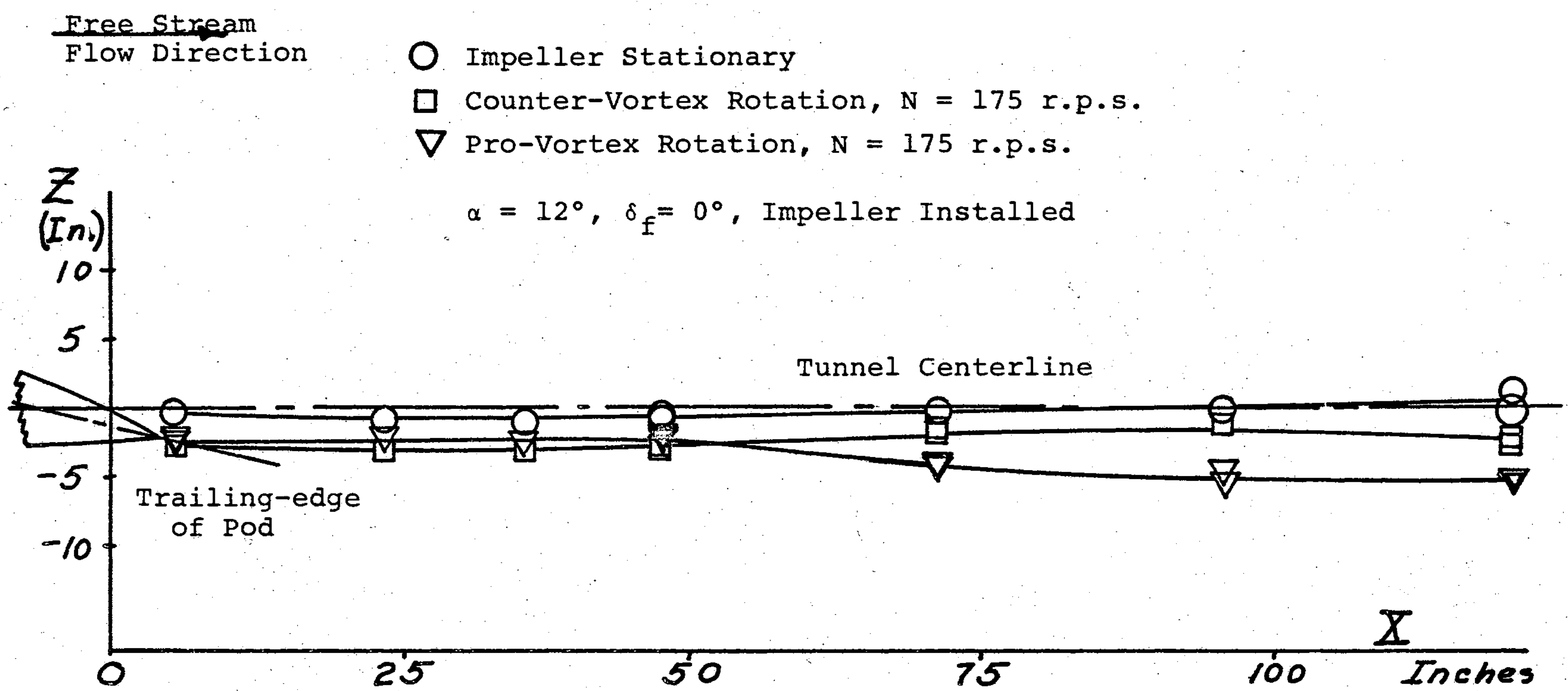

Figure 34. Vortex Core Trajectory in X-Y Plane

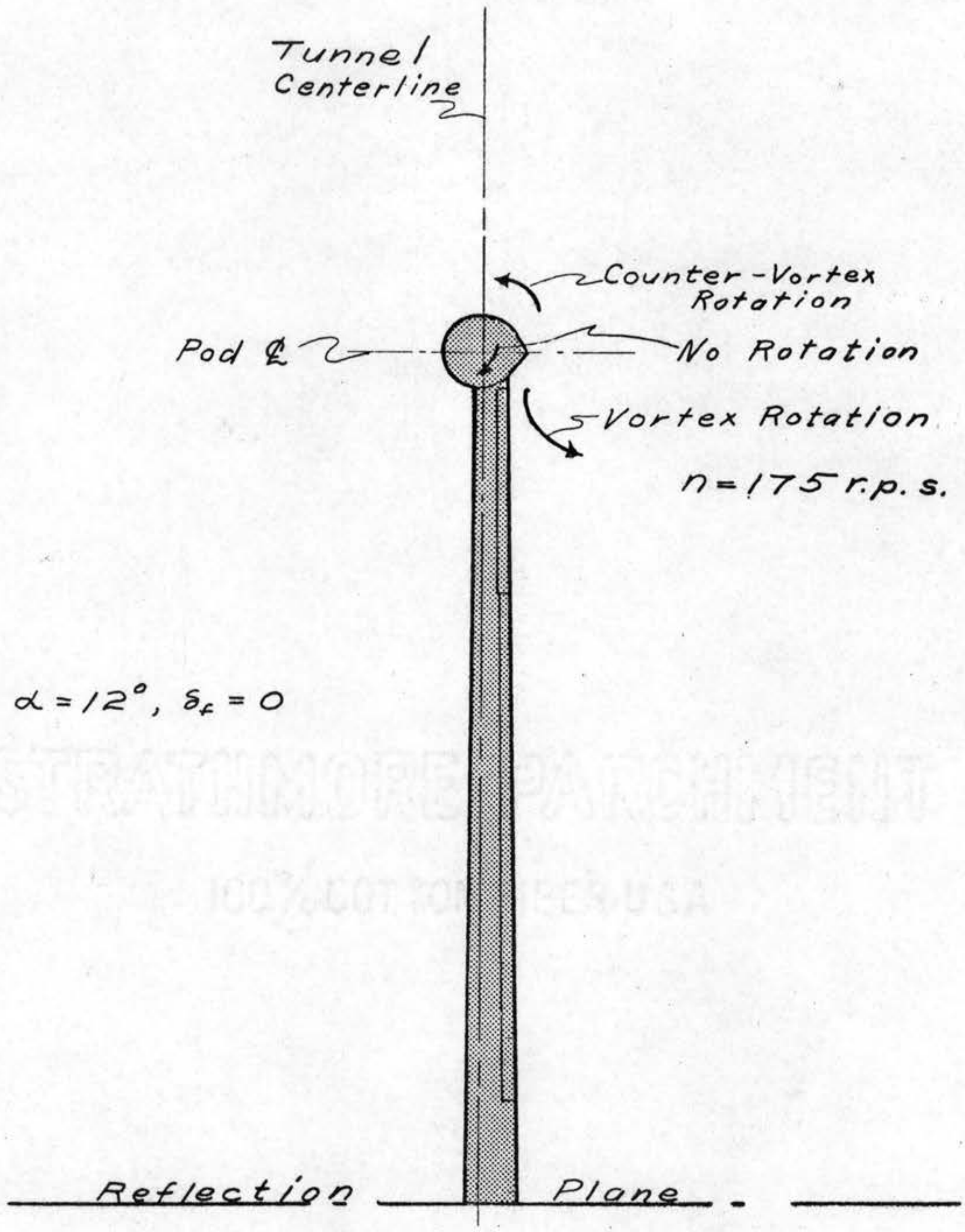

Figure 35. Trajectory of Vortex Core in the Y-Z Plane, Wing With Impeller

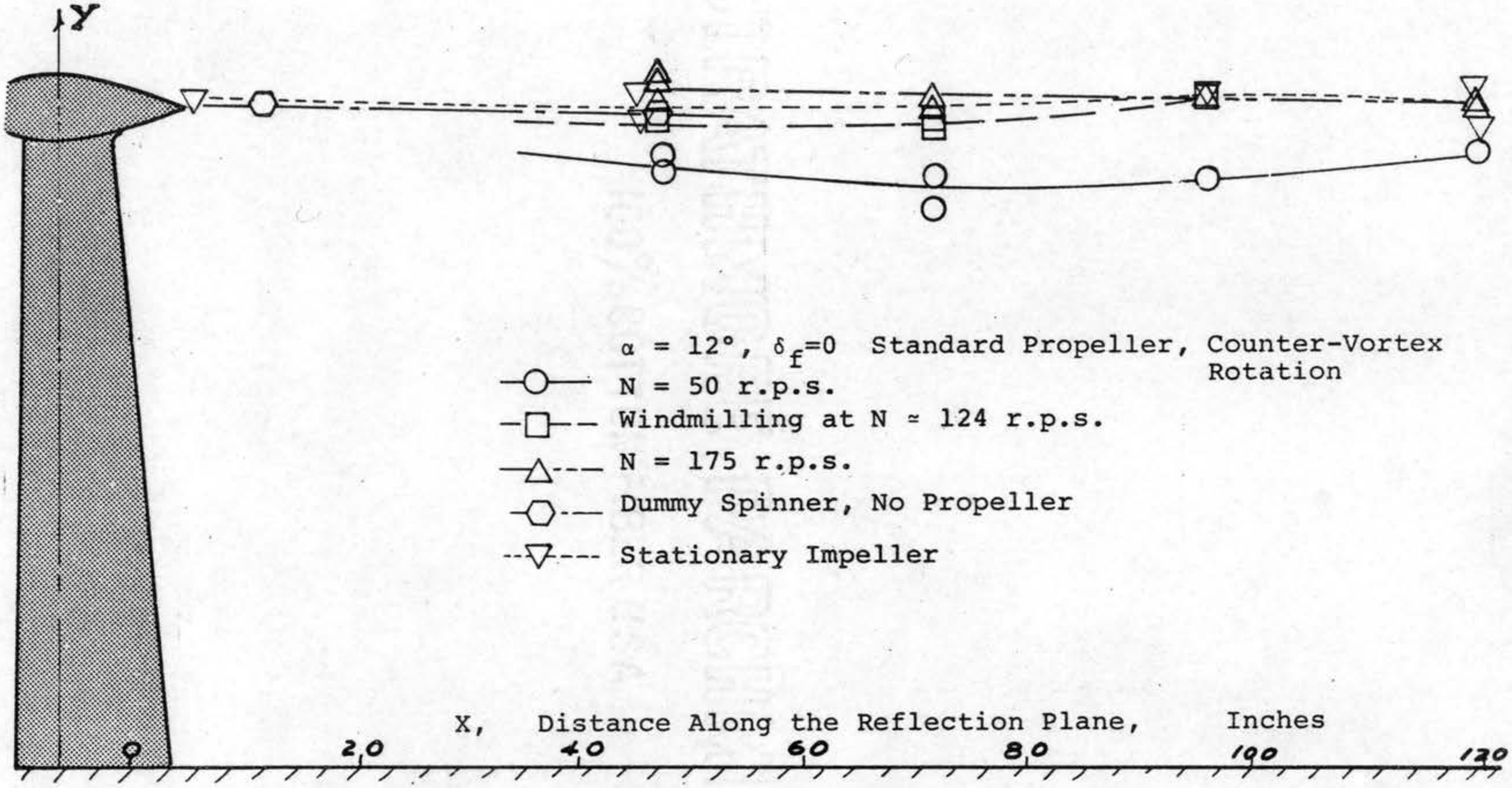

Figure 36. Trajectory of Vortex Core in XY Plane
Wing with Propeller

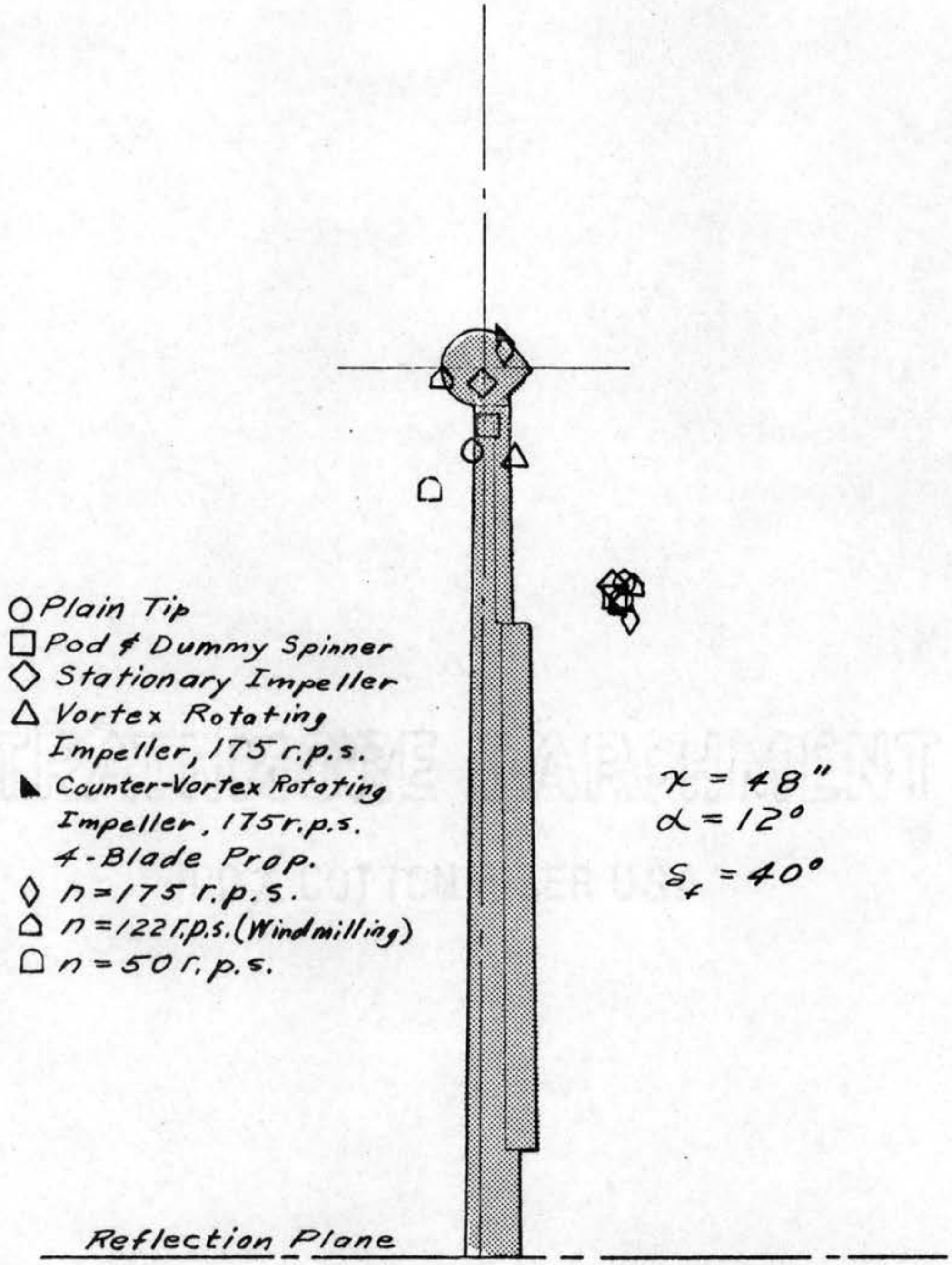

Figure 37. Position of the Center of the Vortex Core, One-Half Span Downstream, for Various Tip Configurations

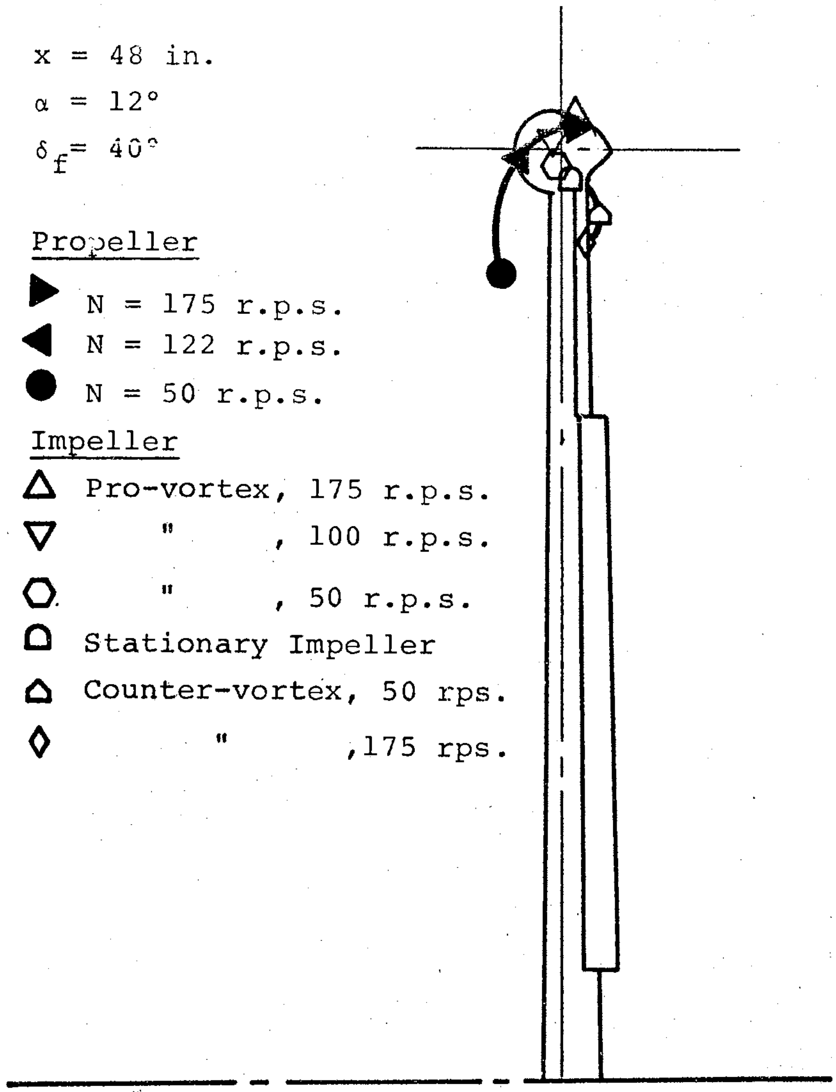

Figure 38. Effect of Rotor Speed and Direction on Position of Center of Vortex Core at One-Half Span Downstream of the Wing

propeller (at greater than windmilling speed) moves the vortex outboard.

c) Vortex rotation of the impeller and counter-vortex rotation of the propeller at less than windmill speed causes the vortex to move inboard.

d) The tip configuration and rotor rotation have little discernible effect on the position of the flap outboard vortex.

e) In the range of rotational speeds involved, the propeller produces greater shift of the trailing vortex than does the impeller.

The effect of rotation of the two types of propellers is further illustrated in Figure 38. It can be seen that as rotation becomes more strongly a counter-vortex rotation the vortex moves outboard. As the rotation becomes more strongly vortex-directed, the trailing vortex moves inboard. The vortex tends to remain in the plane of the wing with the impeller, but there is a shift in the z-direction with the propeller.

Results of the Force and Moment Measurements

The data from the balance system was reduced using the 1620 digital computer. Some of these answers were manually plotted and the remainder were plotted using a Calcomp on-line plotter controlled by the 1620.

The reflection-plane test results are compared with the full-model test in Figure 39. The complete wing test data are from reference 12. It is believed that there is satisfactory agreement of the data.

Another preliminary test was made to determine whether the proximity of the tuft grid to the wing would affect the wing lift. In run 105, the grid was only 1 foot downstream of the wing trailing-edge at the outboard tip. In run 108, the grid was 4 feet downstream. These runs are compared in Figure 40. This plot is a computer plot. Except for a bad point near the stall, the two runs show excellent agreement. Run 102 is also plotted in Figure 40 showing the effect of changing the Reynolds Number from 1.2×10^6 to 6.7×10^5.

All of the subsequent wing tests were at a Reynolds Number of 6.7×10^5. This Reynolds Number resulted from a tunnel dynamic pressure of 10 pounds/sq. ft. (about 100 ft./sec. velocity) which was dictated by two requirements:

1. The behaviour of the tufts was better at less than 10 psf. dynamic pressure (also, the replacement rate for tufts was less than at higher speeds).
2. The windmilling speed of the propeller increases as speed increases. It was desirable to have a speed low enough so that the propeller could be operated at greater than, as well as less than,

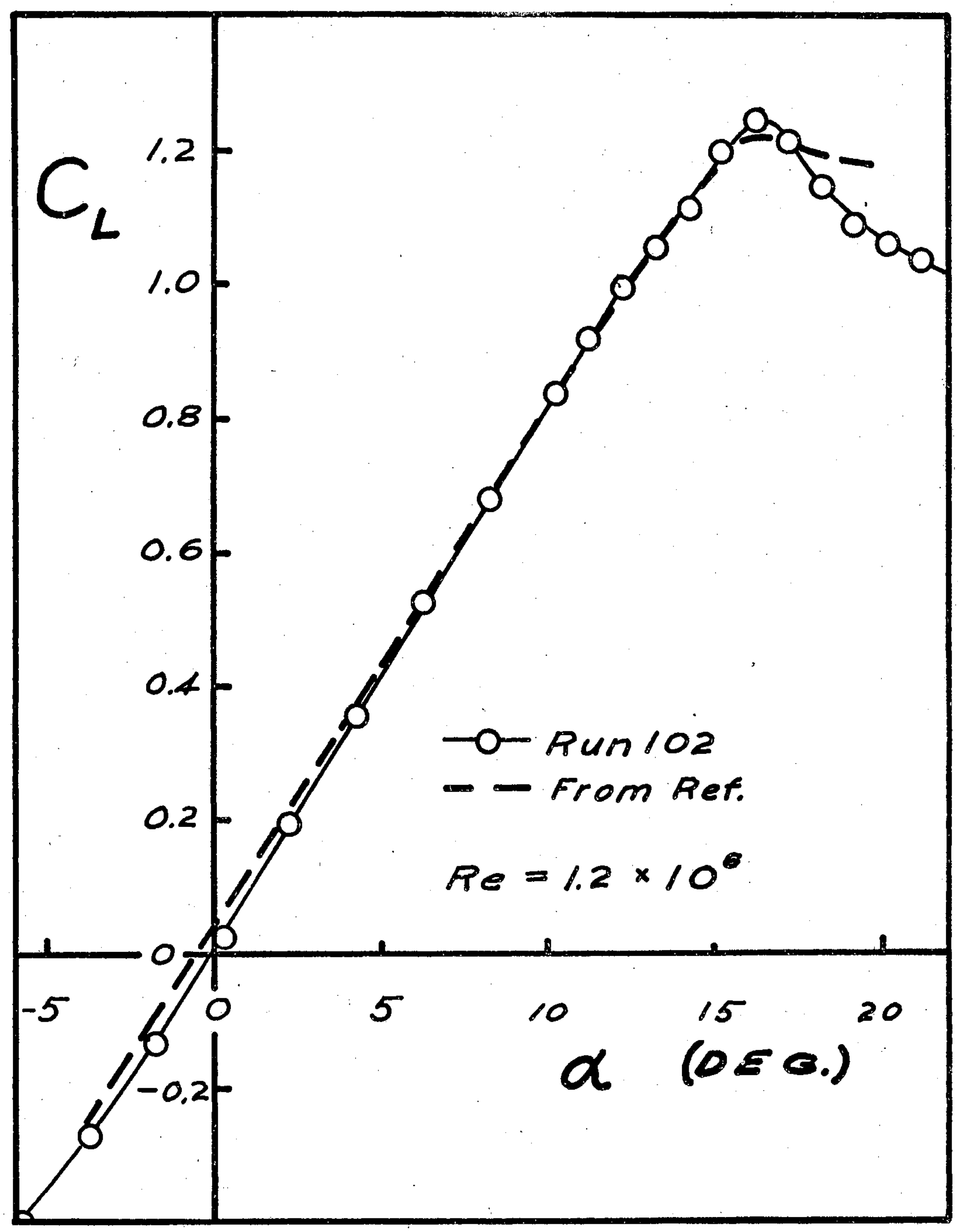

Figure 39. Comparison of Reflection Plane and Complete Models of the Same Wing

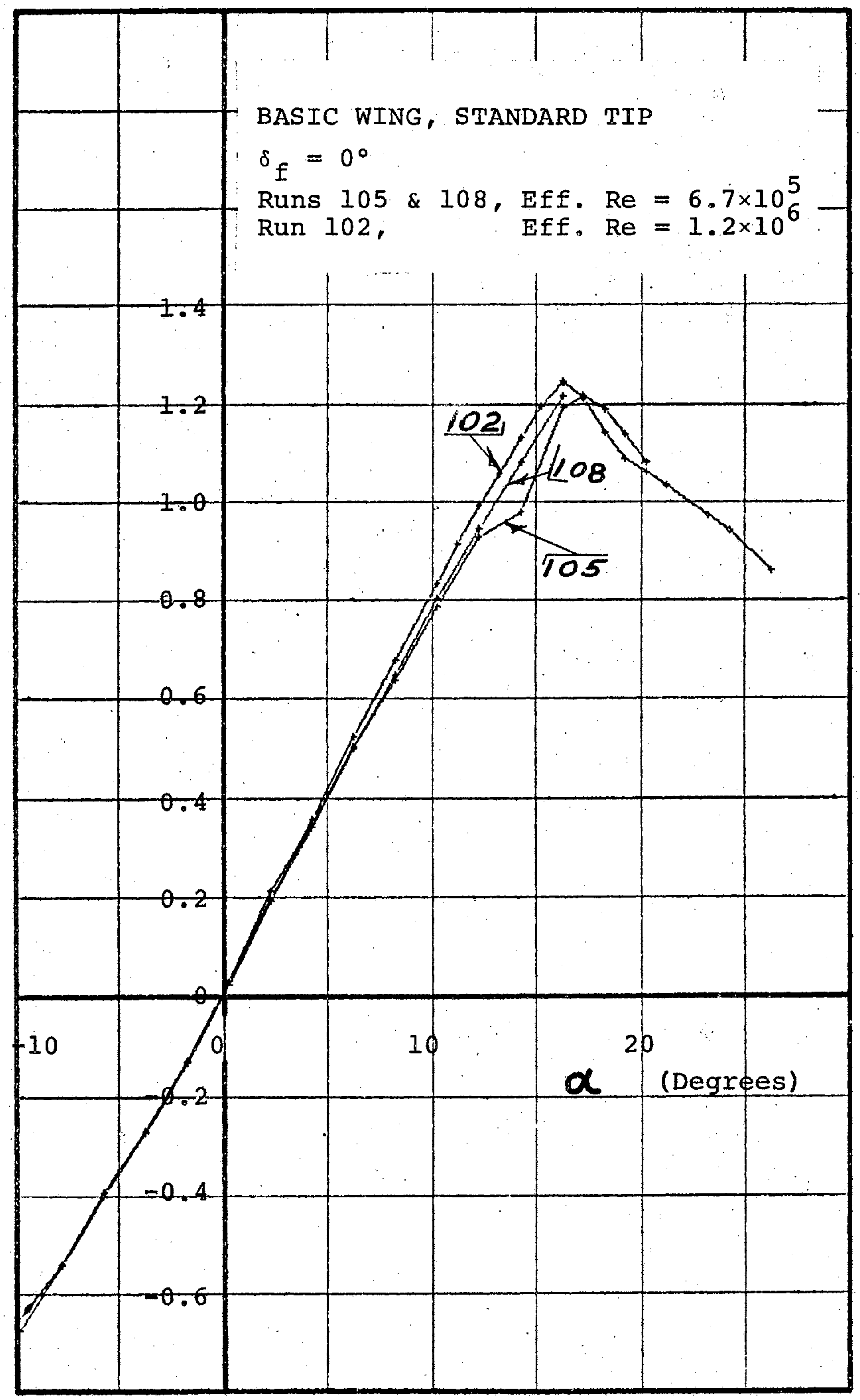

Figure 40. Lift Curve, Basic Wing

windmill speed. The maximum operating speed of the propeller motor is 200 r.p.s.

The results of the reduction of the balance readings are presented graphically in the following forms:

C_L vs. α and C_L vs. $C_{M_{c/4}}$ (<u>not</u> corrected for thrust)

C_L vs. C_D, α, $C_{M_{c/4}}$ (corrected for thrust)

C_D vs. C_L^2 (corrected for thrust)

The data were reduced both with and without tunnel-wall corrections. Since the results were to be correlated with the tuft-grid pictures, it was decided to use the results uncorrected for tunnel boundary. As stated previously, the correction for thrust consisted of determining the lift, drag, and pitching moment due to the thrust of the propeller and impeller as functions of angle of attack (see Figure 30). These values were then subtracted from those measured during the powered tests.

Figure 40 is an example of C_L vs α. The complete set is given in Appendix B, as are the C_L vs $C_{M_{c/4}}$ curves.

Figure 41 is an example of a complete wing polar: C_L vs C_D, α, and $C_{M_{c/4}}$. The complete set of these curves are in the Appendix. The figures which resulted from powered runs have been corrected for the direct effects of thrust.

Figure 42 is an example of a C_D vs C_L^2 graph. The plots for the remaining runs are presented in the Appendix.

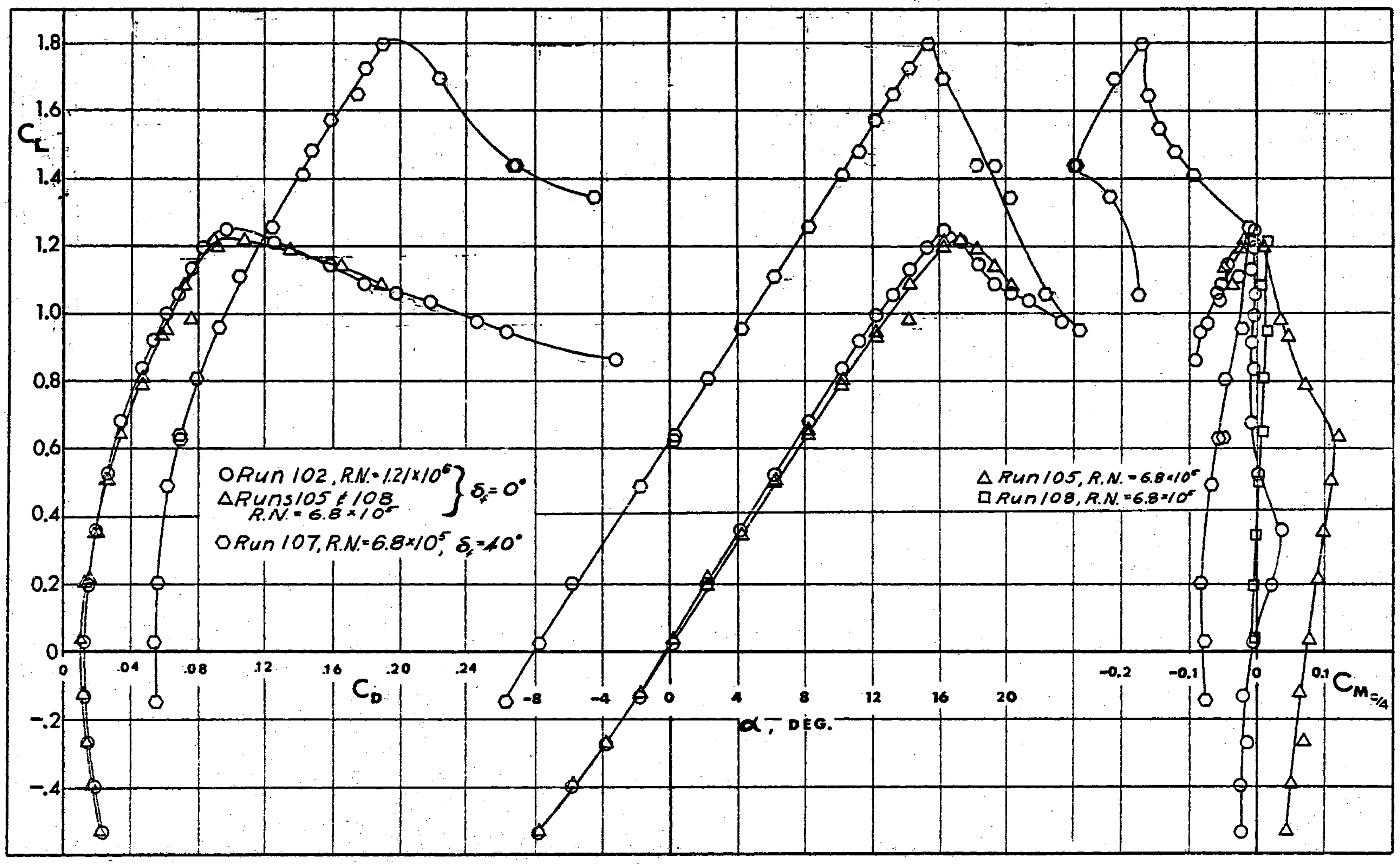

Figure 41. Wing With Plain Tip

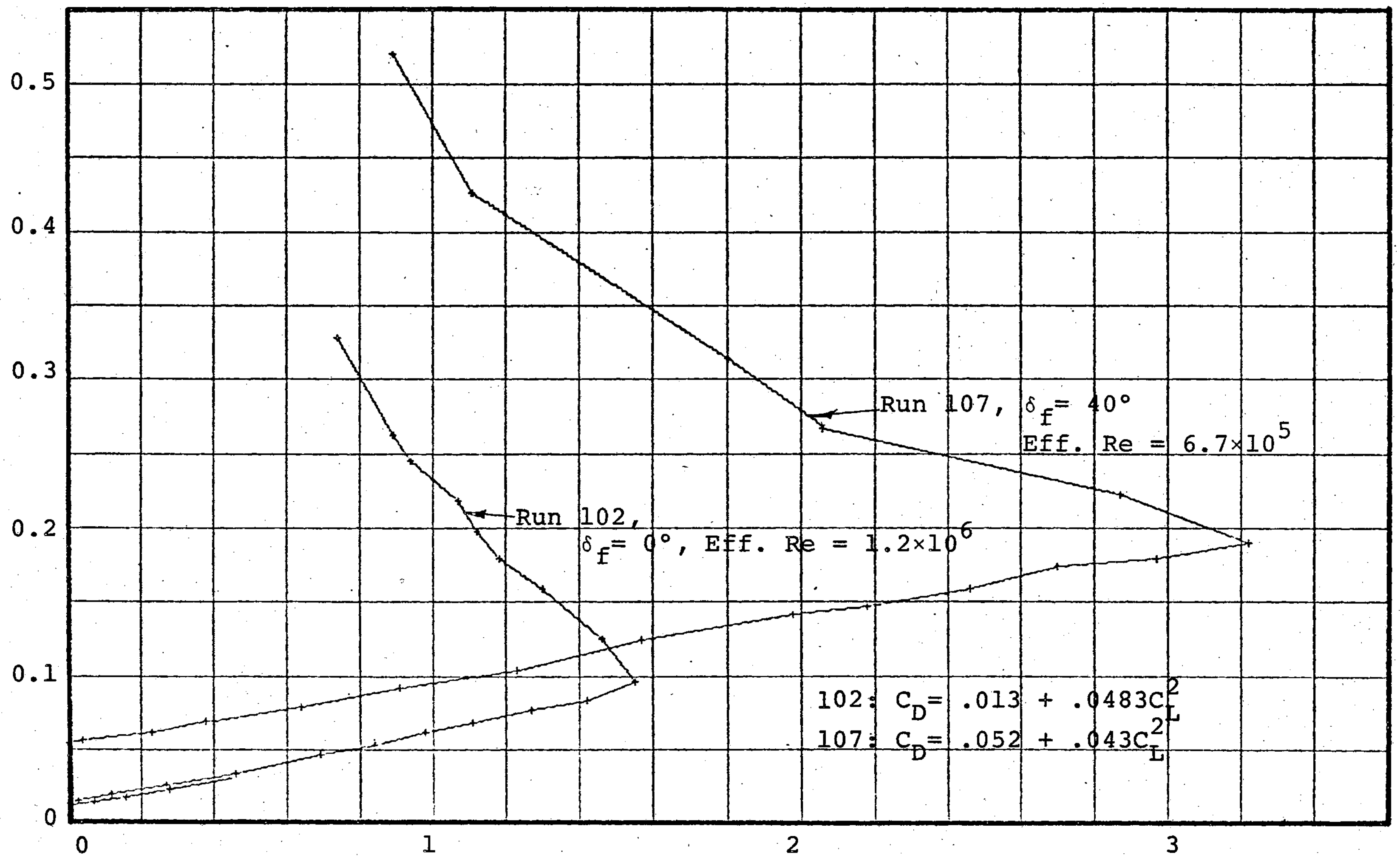

Figure 42. Basic Wing, Standard Tip, Drag Variation

The principal results have been abstracted from these curves and are tabulated in Table V.

The most interesting of these results are shown graphically in Figures 43 and 44. In each of these figures, the abscissa is the counter-vortex rotational speed of the rotor above windmill speed. In the case of the propeller, windmill speed is about 120 r.p.s., so that the propeller curve is plotted for the range 40 r.p.s. to 175 r.p.s. (counter-vortex). In the case of the impeller, the windmill speed is zero; the negative speeds are, then, rotation in the vortex-direction and the positive speeds are rotation in the counter-vortex direction.

Figure 43 shows a very pronounced relationship between impeller or propeller speed and the effective aspect ratio. Effective aspect ratio, Ae_W is defined:

From the plots of C_D vs C_L^2,

$$\frac{d\,C_D}{d\,C_L^2} = m = \frac{1}{\pi\,Ae_W}.$$

(Note: It is assumed that the graph is a straight line, i.e., $m = \frac{d\,C_D}{d\,C_L^2}$ = constant.)

$$\text{Effective aspect ratio} = Ae_W = \frac{1}{\pi\,m} = 0.318\,\frac{d\,C_L^2}{d\,C_D}.$$

The relation between $C_{L_{max}}$ and rotor speed is less obvious and less conclusive; see Figures 44 and 45.

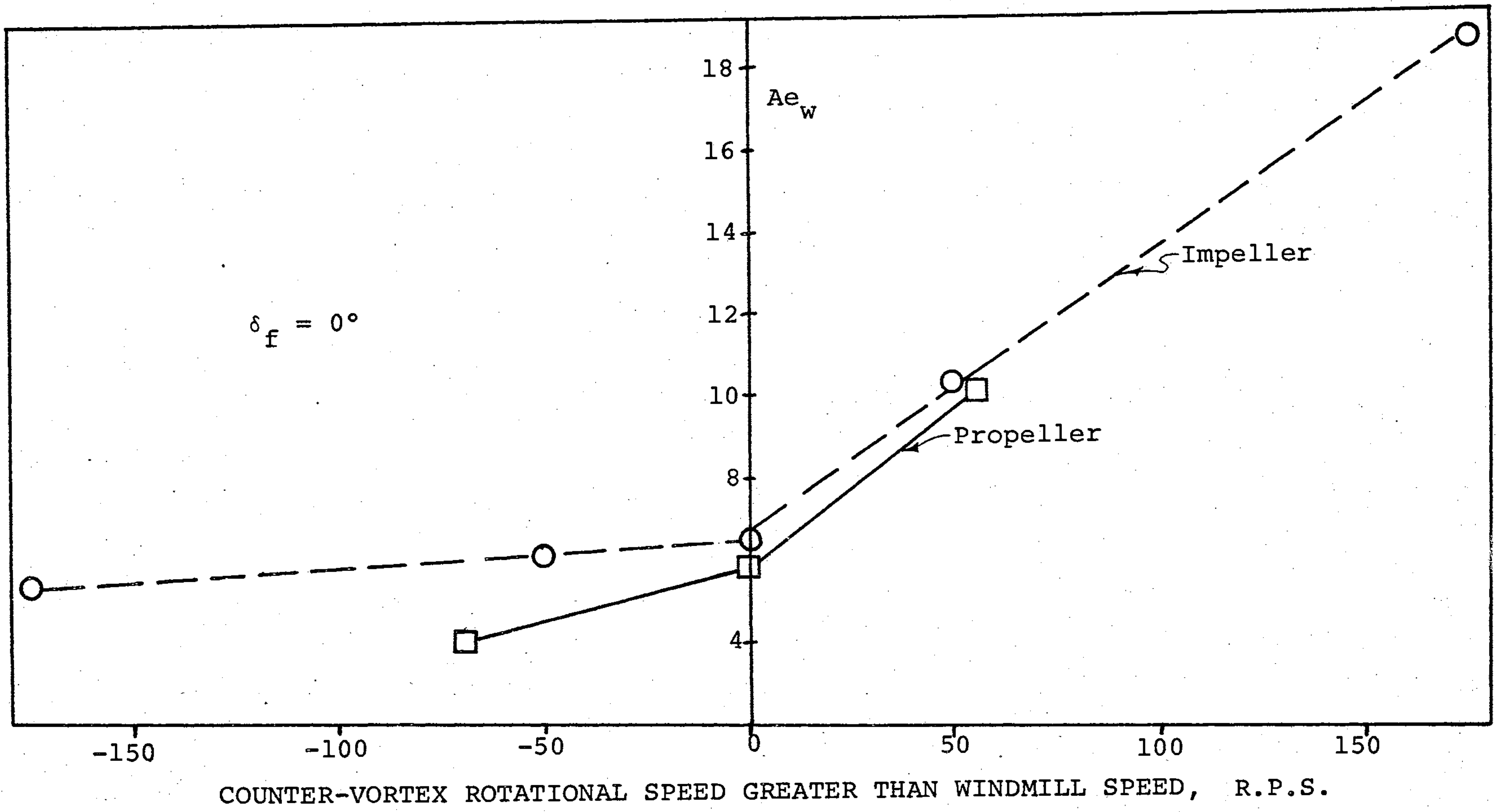

Figure 43. Variation of Effective Aspect Ratio Caused by Rotor Speed

TABLE V

SUMMARY OF WING CHARACTERISTICS

δ_f	Rotation Direction	N (r.p.s.)	$C_{L_{max}}$ not cor.	$C_{L_{max}}$ cor. for thrust	C_{L_α} not cor.	C_{L_α} cor. for thrust	$C_D = C_{D_P} + mC_L^2$ (cor. for thrust)	Eff. Aspect Ratio = Ae_w
	<u>Plain Wingtip</u>							
0	None		1.22	-	.083	-	$.012 + .0477C_L^2$	6.67
40	None		1.80	-	.08	-	$.052 + .042C_L^2$	7.48
	<u>Pod with Dummy Spinner</u>							
0	None		1.25	-	.078	-	$.013 + .0493C_L^2$	6.45
40	None		1.80	-	.093	-	$.058 + .0357C_L^2$	8.91
	<u>Impeller</u>							
0	None		1.25		.085	.085	$.013 + .0503C_L^2$	6.32
0	Vortex	50	1.26	1.215		.072	$.015 + .0517C_L^2$	6.15
0	Vortex	175	1.25	1.27		.083	$.0125 + .0595C_L^2$	5.34
0	Counter Vor.	50	1.22	1.19		.085	$.015 + .0307C_L^2$	10.35
0	Counter Vor.	175	1.31	1.26		.08	$0 + .017C_L^2$	18.7
	<u>4-Bladed Propeller</u>							
0	Counter Vor.	50	0.95	0.19	.08	.072	$.032 + .0795C_L^2$	4.0
0	Counter Vor.	119	1.2	1.22	.085	.08	$.012 + .0555C_L^2$	5.73
0	Counter Vor.	175	1.325	1.265	.10	.086	$-.013 + .0315C_L^2$	10.1

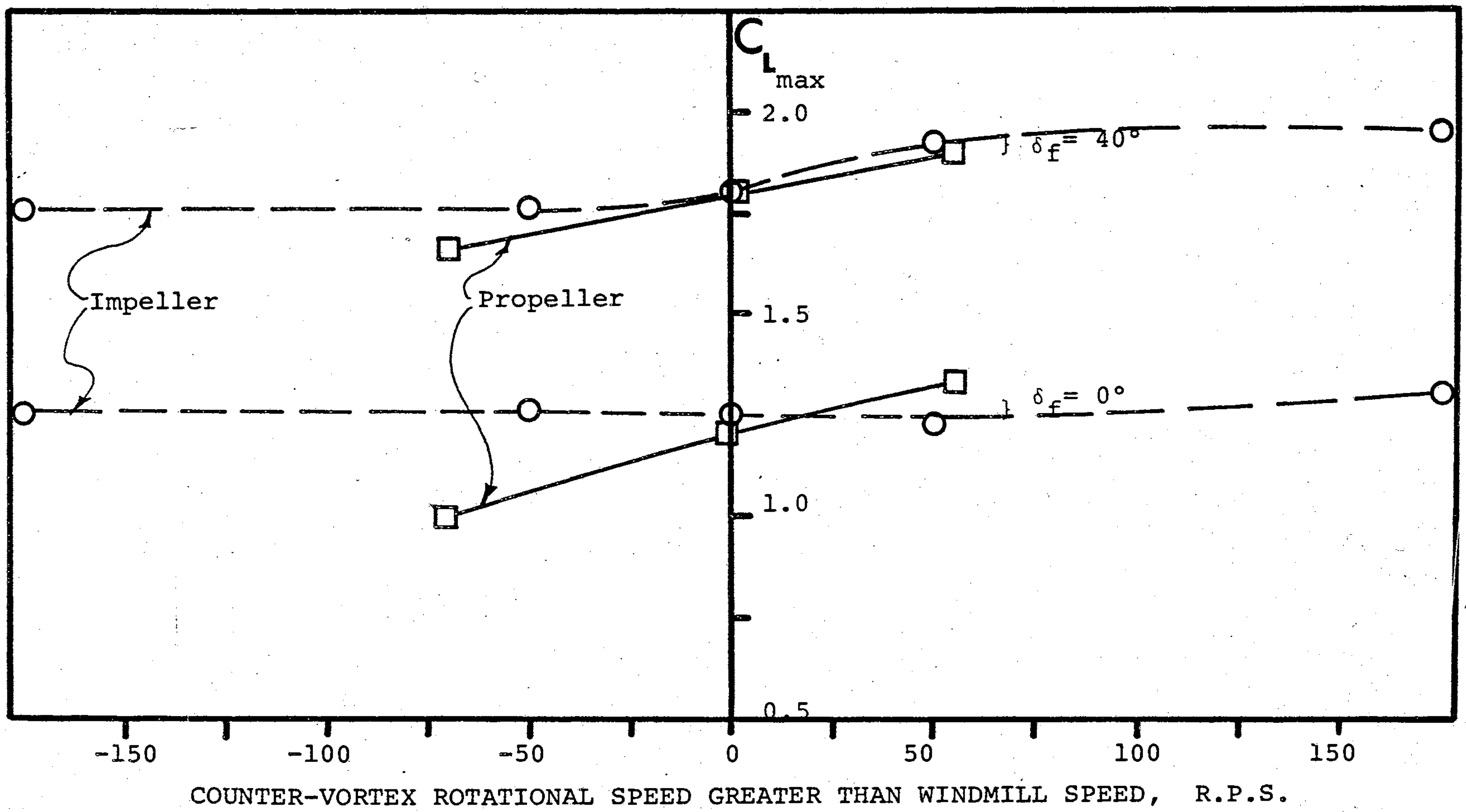

Figure 44. Effect of Rotor Speed on $C_{L_{max}}$

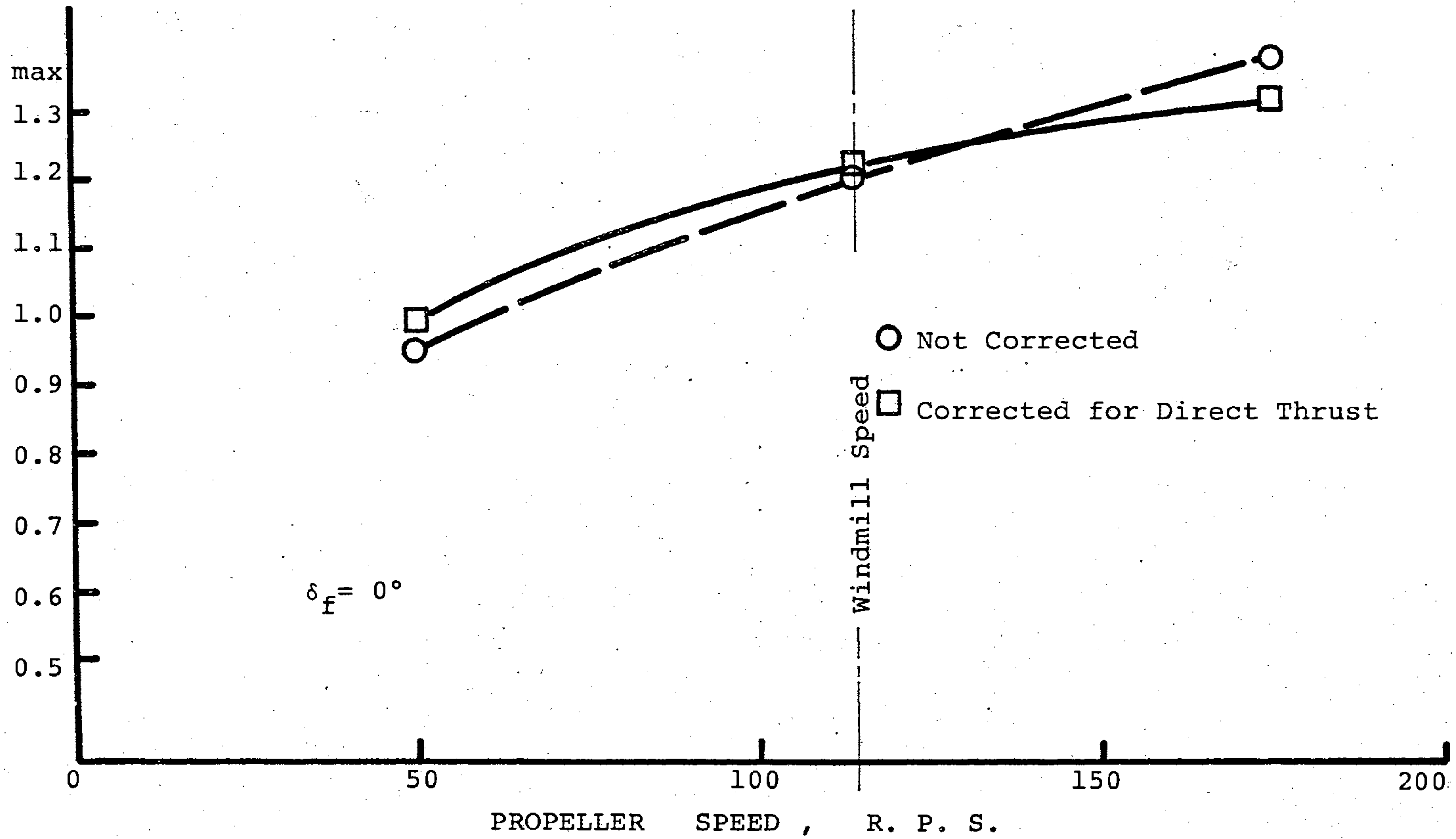

Figure 45. Effect of Rotational Speed of Propeller on Wing Maximum Lift Coefficient

CHAPTER IV

ANALYSIS OF RESULTS

The principal results expected from the experimental program are:

1. Alteration of the flow field downstream of the wing. This changed flow field would be identified by changes in the downwash and by altered trajectories of the core of the trailing vortex.
2. Changes in the wing loading, resulting in changed lift-curve slope and $C_{L_{max}}$.
3. Changes in wing drag, chiefly in the induced portion of the drag.

Vortex Trajectories

Figures 33 through 37 show the changes in the position of the core of the trailing vortex caused by rotation of the impeller and of the propeller. The chief effect is the change in the vortex span which is apparent in Figures 33 and 36. It can be seen that the change in vortex span is not the result of bending of the flow downstream of the wing. Rather, the shift apparently occurs upstream of the first grid position. This fact indicates that the vortex span is the result of the distribution of strength in the shed vortex sheet.

Table VI summarizes the vortex span and the effective aspect ratio for the various configurations tested.

TABLE VI

VORTEX SPAN AND EFFECTIVE ASPECT RATIO

Configuration	Eff. Aspect Ratio Ae_w	Vortex Span b_v, ft.
Dummy Spinner, No Propeller	6.45	8.25
Stationary Impeller	6.32	8.42
Impeller, Counter-Vortex Rotation, N = 175 r.p.s.	10.35	8.93
Impeller, Vortex-Rotation N = 175 r.p.s.	5.34	7.42
Propeller, Windmilling, N = 175 r.p.s.	5.73	8.33
Propeller, Counter-Vortex Rotation, N = 175 r.p.s.	10.1	8.42
Propeller, N = 50 r.p.s.	4.0	7.42

In an attempt to determine a relationship between effective aspect ratio and the vortex span, these quantities are graphed in Figure 46. A curve has been fit to

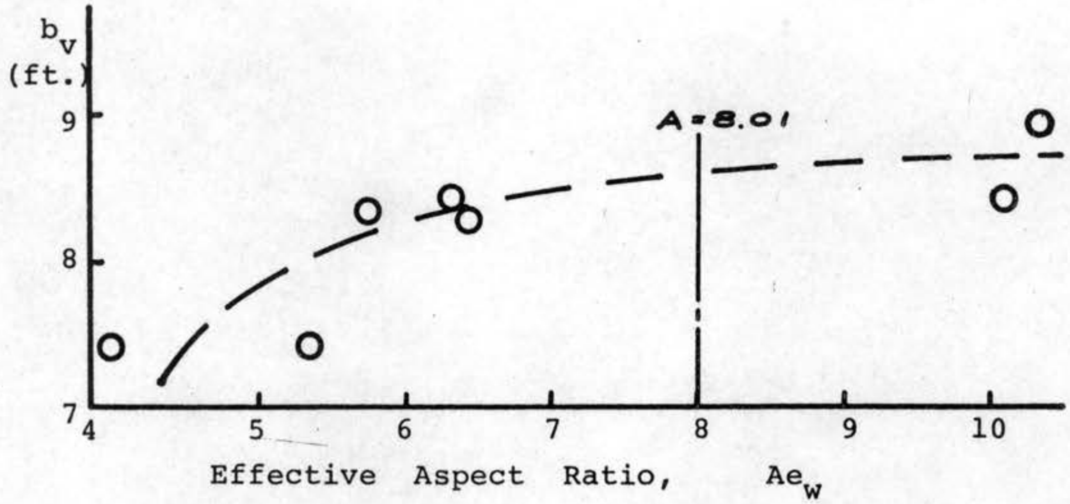

Figure 46. Vortex Span and Effective Aspect Ratio for Test Configurations

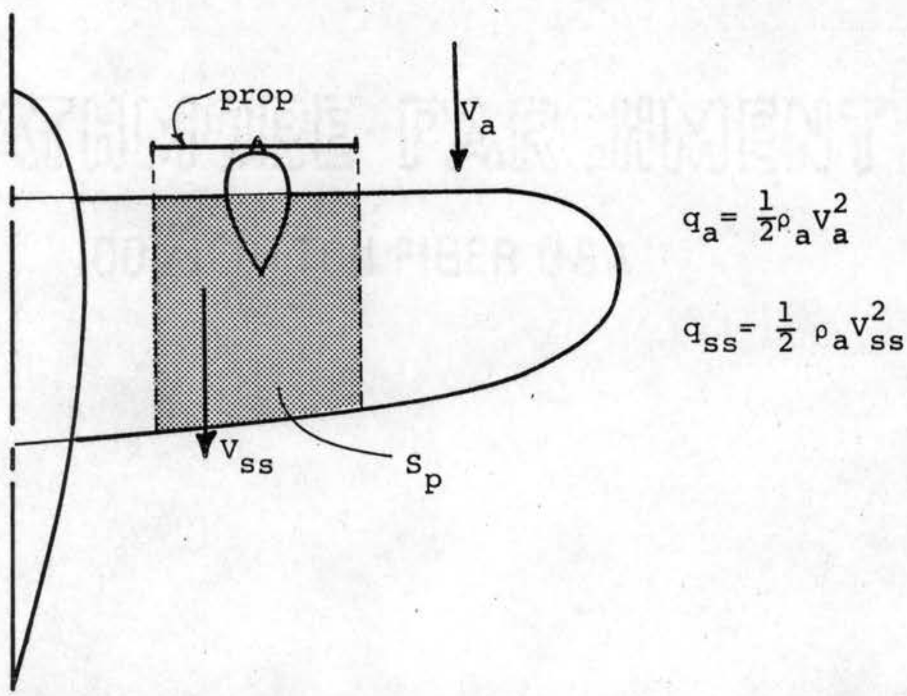

Figure 47. Nomenclature for Wing Partially Submerged in Propeller Slipstream

the data; the equation of this curve is:

$$b_v = -4.2 + 4.74(Ae_w) - 0.592(Ae_w)^2 + 0.025(Ae_w)^3 .$$

The validity of this equation is suspect because of the relatively large scatter of the data. However, it can be seen that there is an increase of vortex span as the effective aspect ratio increases.

It will be noticed, from Figures 34 and 35, that the vortex (no power) leaves the wing at the level (in the z-direction) of the trailing-edge of the wing, while with power (either direction) it is lower; i.e., roughly at the level of the tip of the pod. Figures 35 and 37 indicate that the propeller produces a greater vertical shift of the vortex core than does the impeller. This result agrees with the larger changes in effective aspect ratio caused by the four-bladed propeller.

The cause of both of these effects is the axial component of propeller/impeller slipstream. This axial velocity is higher than the stream velocity. At the 12 degree angle of attack, the axial velocity has a component in the z-direction of V_{ss} sin 12° (equals $0.208V_{ss}$). This component moves the initial point of the vortex down. Also, the component will be larger for the propeller than for the impeller because the propeller has a higher slipstream velocity, V_{ss}.

Effects of Power on Lift and Drag

It would be expected that the addition of thrust power to a wing, producing a slipstream over the wing, would result in a higher indicated lift coefficient at any given angle of attack and in a higher maximum lift coefficient. With reference to Figure 47, it may be reasoned that:

$$(C_L)_{calculated} = \frac{L}{q_a S} \quad ; \quad L = C_{L_{calc}} q_a S$$

$L = L_{ss} + L_{res}$ where, L_{ss} is lift developed by the portion of the wing in the slipstream (S_p). L_{res} is lift developed by the rest of the wing (S_{res}).

$$L = C_{L_{actual}} q_{ss} S_p + C_{L_{actual}} q_a S_{res}$$

$$= S\left[C_{L_{actual}} q_{ss} \frac{S_p}{S} + C_{L_{actual}} q_a \frac{S - S_p}{S}\right]$$

$$= C_{L_{calc}} q_a S = C_{L_{actual}} S\left[q_{ss} \frac{S_p}{S} + q_a\left(1 - \frac{S_p}{S}\right)\right]$$

$$C_{L_{calc}} = (C_L)_{actual} \left[1 + \frac{S_p}{S}\left(\frac{q_{ss}}{q_a} - 1\right)\right].$$

The number within the brackets is always greater than 1 for a thrusting propeller. The apparent C_L, i.e., $C_{L_{calc}}$, is larger than the C_L actually being developed by the wing. Note that this apparent, or effective, C_L does not include any vertical component of the propeller thrust.

As an example of this effect, data have been extracted from references 12 and 13 on the RM-9 airplane. This airplane was equipped with the same wing as the wing of this test, except that it was equipped with four engine nacelles, two on each wing. A sketch of the model is shown in Figure 48. Some effects of power are listed in Table VII.

TABLE VII

RM-9 WITH 60 DEG. FLAPS, NO TAIL

Configuration	C_L at $\alpha = 0°$	$C_{L_{max}}$
No Propellers	0.93	1.77
Propellers 1 and 2 only, Tc = .82	1.33	2.38
Propellers 3 and 4 only, Tc = .82	1.47	2.50
All Propellers, Tc $\approx$ .82	1.80	3.40

Re = 7.3×10^5, Direct Thrust Effects Removed

These data confirm the earlier statement, i.e., that the C_L in a slipstream is higher than without a slipstream, even without including any lift component of the thrust. They also confirm the known fact that it is better to turn

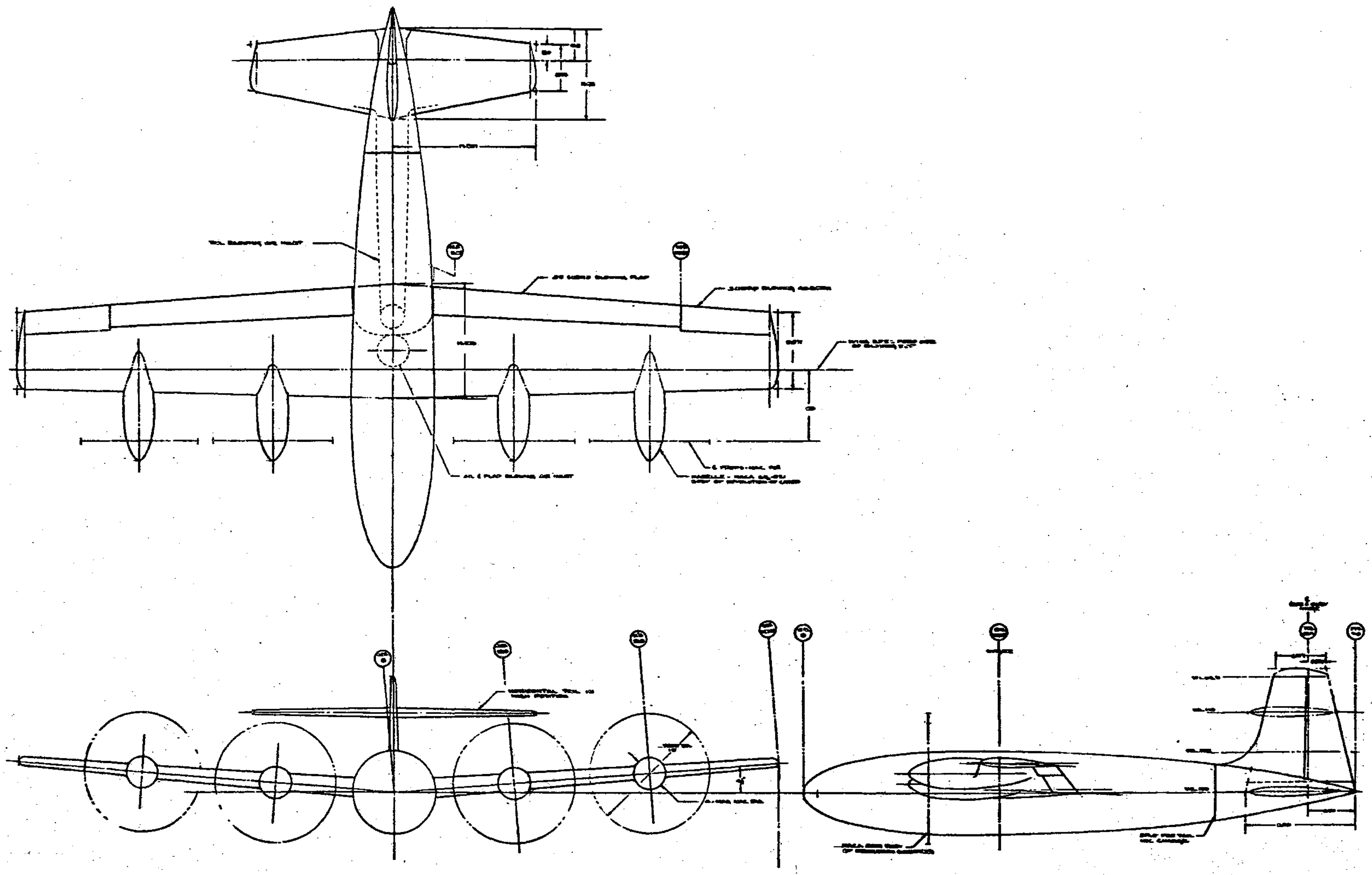

Figure 48. Three-View Drawing of RM-9 Model

the propellers in the direction opposite to the direction of the vortices being shed. Propellers 1 and 2 turn the same direction as the shed vorticity of the port wing; propellers 3 and 4 turn in the direction opposite to that of the shed vorticity of the starboard wing. The ΔC_L due to the propeller action is apparently only partly due to increased slipstream velocity. It is also due to the amplification or attenuation of wing lift due to interaction of the rotating propeller slipstream with the wing.

Figures 44 and 45 indicate a similar effect with a single impeller or propeller mounted at the wingtip, i.e., as the counter-vortex speed of the rotor increases, the value of $C_{L_{max}}$ increases. Figure 45 indicates that correcting $C_{L_{max}}$ for thrust produces negligible change in $C_{L_{max}}$.

It is apparent that direction of rotation of the propeller, and also the spanwise position of the propeller affect the wing performance. In order to analyze these effects, additional data were abstracted from reference 54. The advantage of using these data is that both the wing and propeller used in the current test are the same as those used on the RM-9 (54). However, the propeller pitch was different (15.5 deg. in present test, 19 deg. on RM-9).

It was possible to calculate, from the tunnel tests, the thrust characteristics of the propeller and of the impeller. These are shown in Figures 49 and 50. Thrust

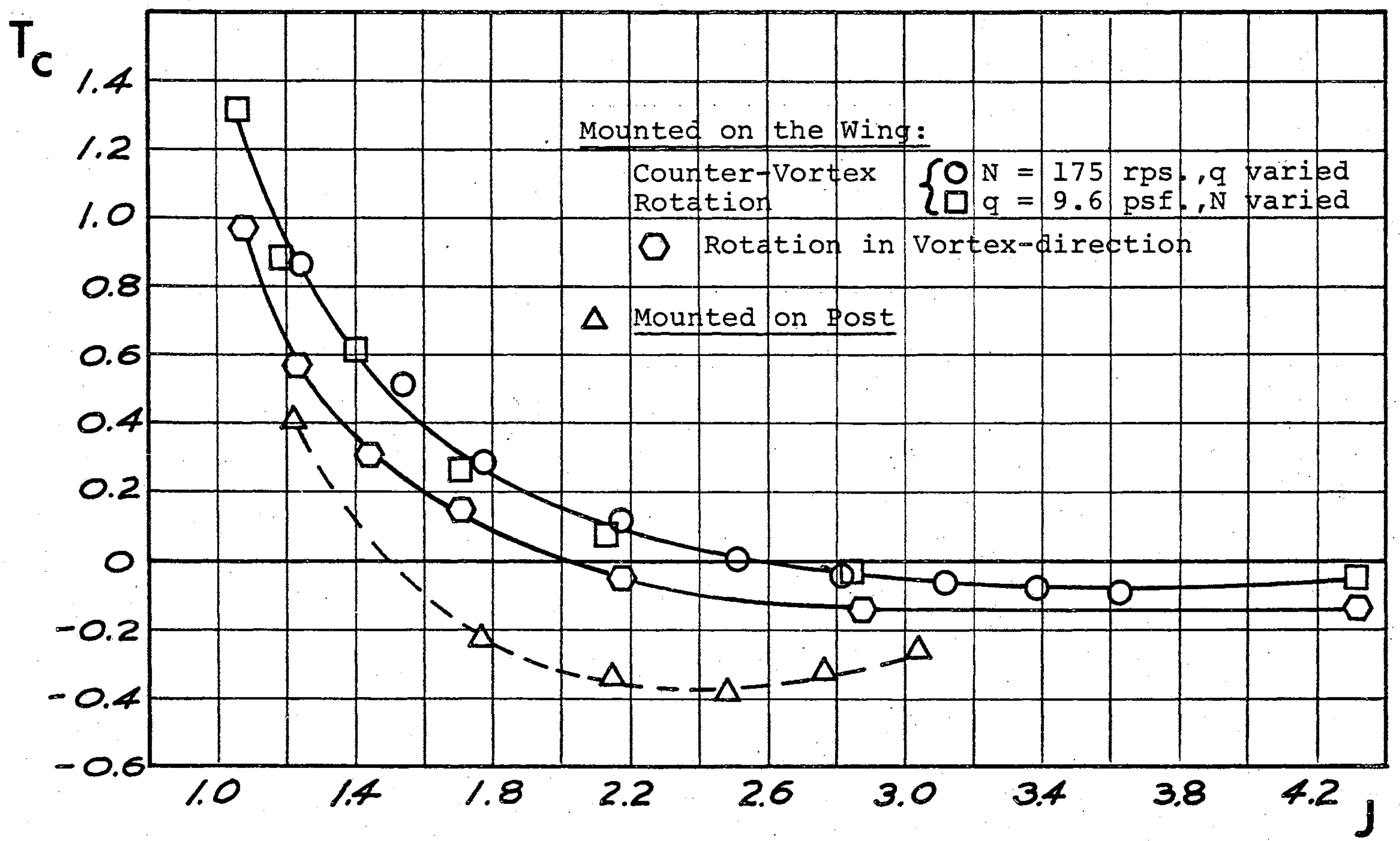

Figure 49. Thrust Coefficient of Impeller.

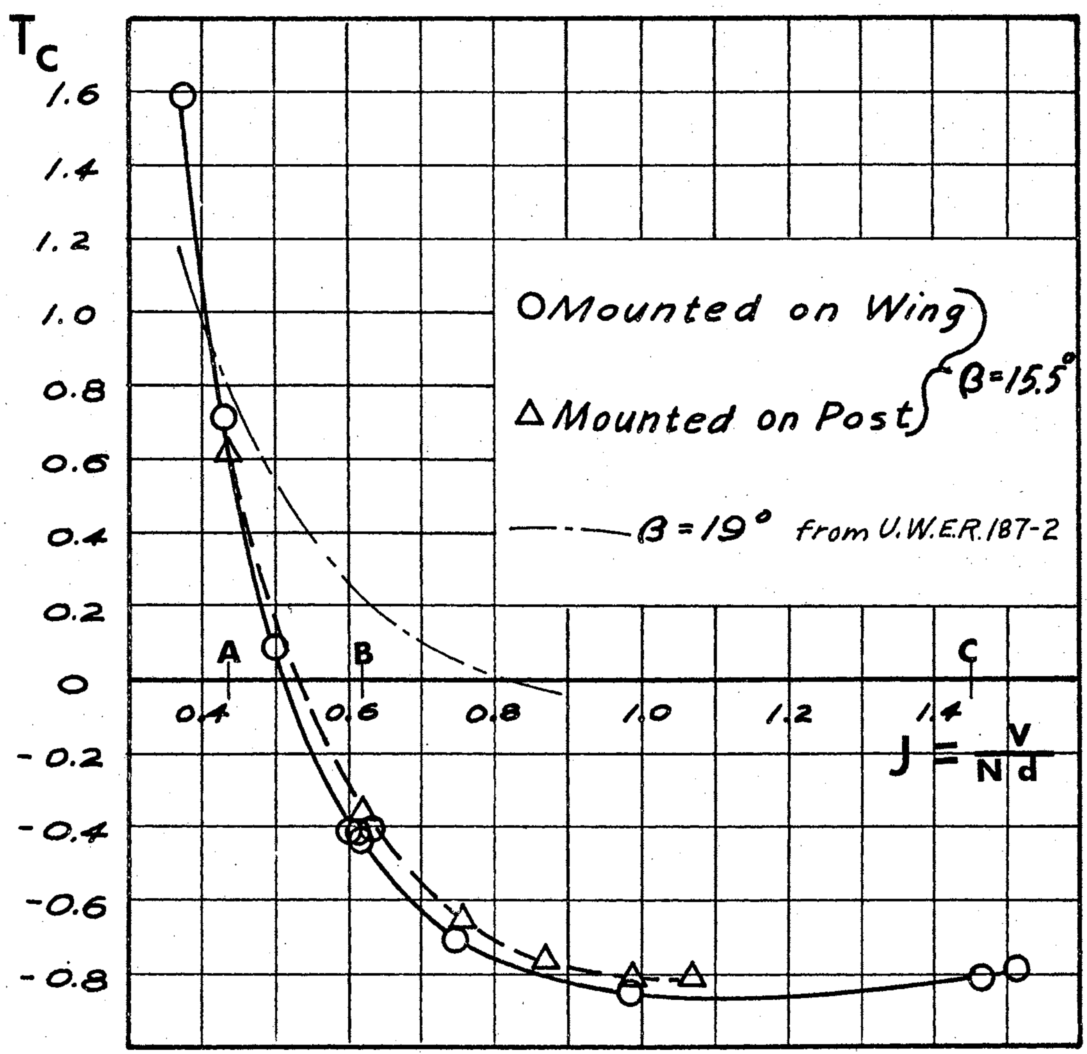

A corresponds to N = 175 r.p.s. at test dynamic pressure.

B corresponds to N = 122 r.p.s. (windmilling speed) at test dynamic pressure.

C corresponds to N = 50 r.p.s. at test dynamic pressure.

Figure 50. Thrust Coefficient of Propeller

coefficient may be defined as $C_T = \frac{\text{Thrust}}{\rho N^2 \ d^4}$ or $T_C = \frac{\text{Thrust}}{\frac{\rho}{2} V^2 d^2}$, and $C_T = T_C \ J^2$. T_C is used in Figures 49 and 50 chiefly for comparison with values from reference 54. It will be noticed that the operational range of $J = \frac{V}{Nd}$ for the impeller is considerably above that of the propeller. The curves for the propeller are extended into the negative thrust region, for this range corresponds to the rotational speeds less than windmill speed. Also in Figure 50, there is a graph of the thrust coefficient curve for the propeller at the blade angle used in the RM-9 tests.

Most of the RM-9 powered data is reported at $T_C = .82$ or $T_C = .44$. The $T_C = .44$ was developed at a rotational speed of approximately 188 r.p.s. This combination was the nearest to the $T_C \approx .65$ and N = 175 r.p.s. in this test.

Lift curve data was abstracted from Figures 9 and 10 of reference 54 for the RM-9 wing, body and nacelles combination with $\delta_f = 0$. The data were corrected to the cases of single propeller operation and these corrected curves are plotted in Figures 51 and 52. The effect of propeller position on the lift and drag of the wing is tabulated in Table VIII. The values of effective aspect ratio, lift-curve slope, and D/L at $C_L = 1.0$ from Table VIII are plotted in Figure 53.

Figure 53 illustrates, very well, the effects of spanwise position of the propeller on the wing

TABLE VIII

EFFECT OF PROPELLER POSITION ON WING CHARACTERISTICS

Propeller Position	Direction of Rotation	$C_{L_\alpha} = \frac{dC_L}{d\alpha}$	C_D Equation	Ae_w	D/L at $C_L = 1.0$
Reflection Plane Wing, $\delta_f = 0$					
No Propeller (with Pod)	None	0.078	$C_D = .013 + .0493C_L^2$	6.45	0.062
Tip, $\frac{y}{b/2} = 1.0$	*	0.072	$C_D = .032 + .0795C_L^2$	4.0	0.112
Tip, $\frac{y}{b/2} = 1.0$	Counter-Vortex	0.086	$C_D = .013 + .0313C_L^2$	10.1	0.018
RM-9 Model - Wing, Body, Nacelles, $\delta_f = 0$					
No Propeller (with Nacelles)	None	0.0785	$C_D = .018 + .0483C_L^2$	6.58	0.066
No. 1, $\frac{y}{b/2} = 0.66$	Vortex	0.0825	$C_D = .02 + .08C_L^2$	3.98	0.10
No. 2, $\frac{y}{b/2} = 0.31$	Vortex	0.0825	$C_D = .025 + .0583C_L^2$	5.46	0.083
No. 3, $\frac{y}{b/2} = 0.31$	Counter-Vortex	0.0831	$C_D = .016 + .0633C_L^2$	5.03	0.079
No. 4, $\frac{y}{b/2} = 0.66$	Counter-Vortex	0.0788	$C_D = .009 + .0508C_L^2$	6.26	0.060

*Counter-vortex rotation, but at negative thrust and N less than windmill speed.

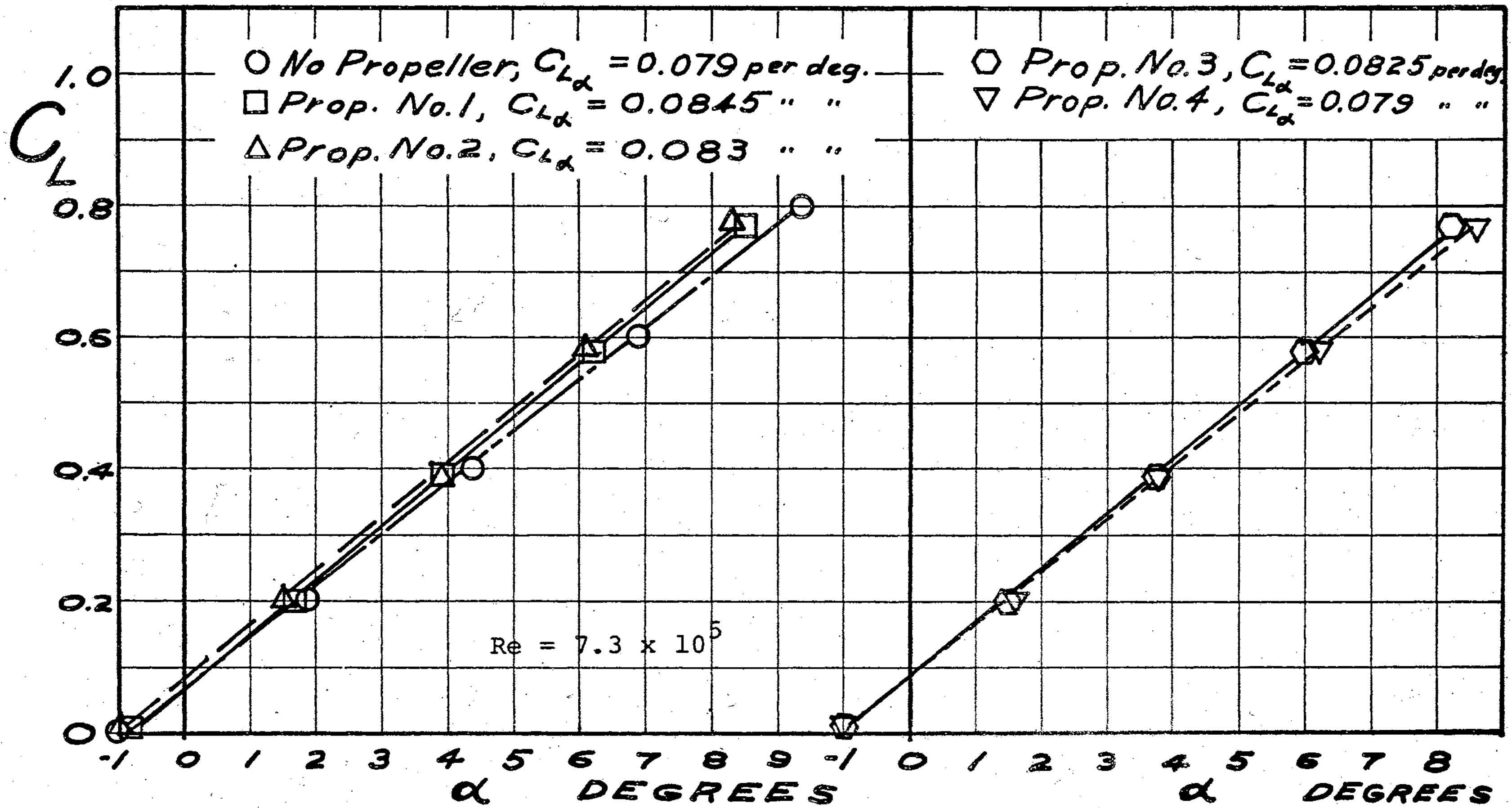

RM-9 Wing, Body, & Nacelles, $\delta_f = 0$, $T_c = 0.44$, N = 188 r.p.s.

Figure 51. Effect of Propeller Position on Lift Curve

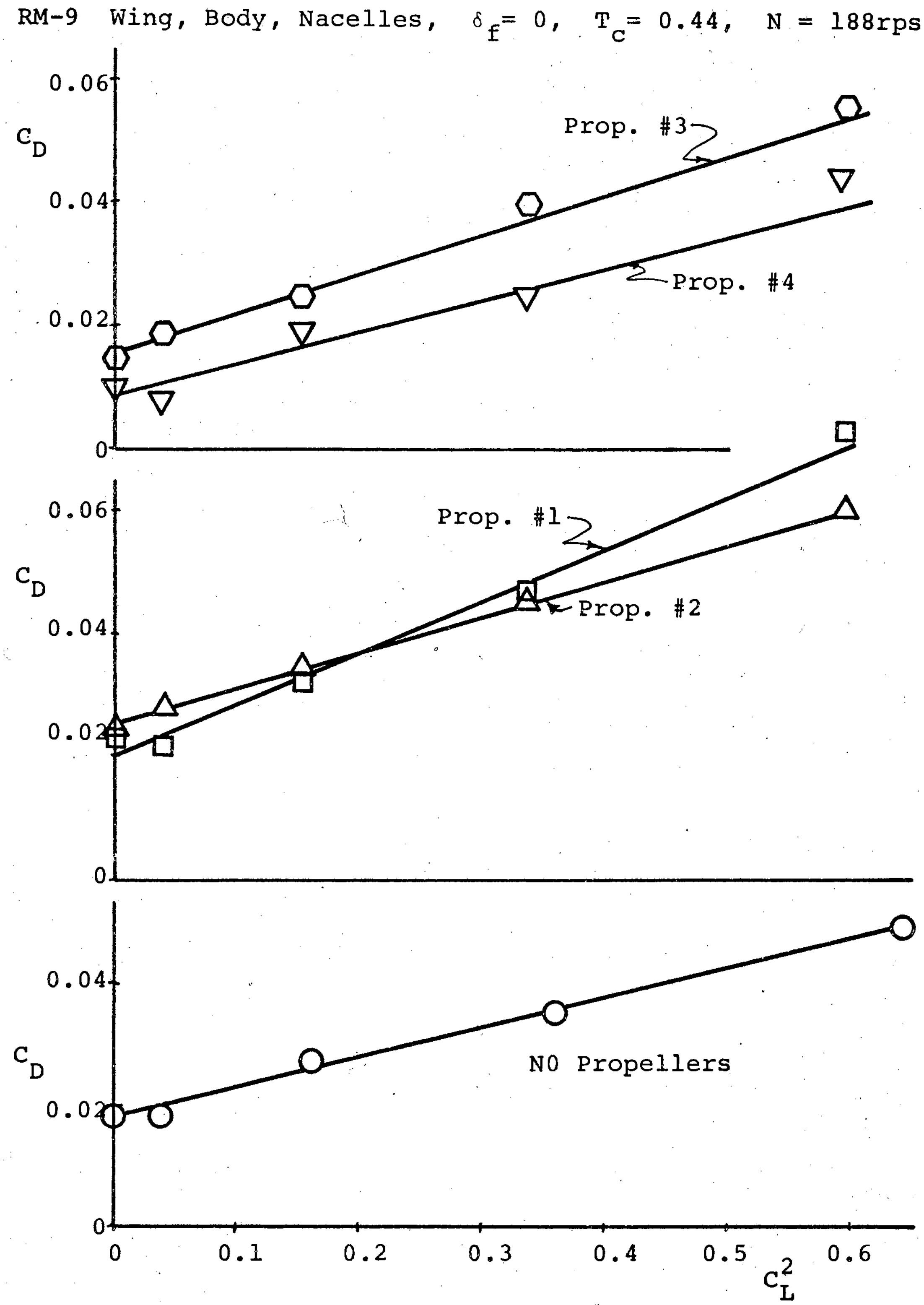

Figure 52. Effect of Propeller Position

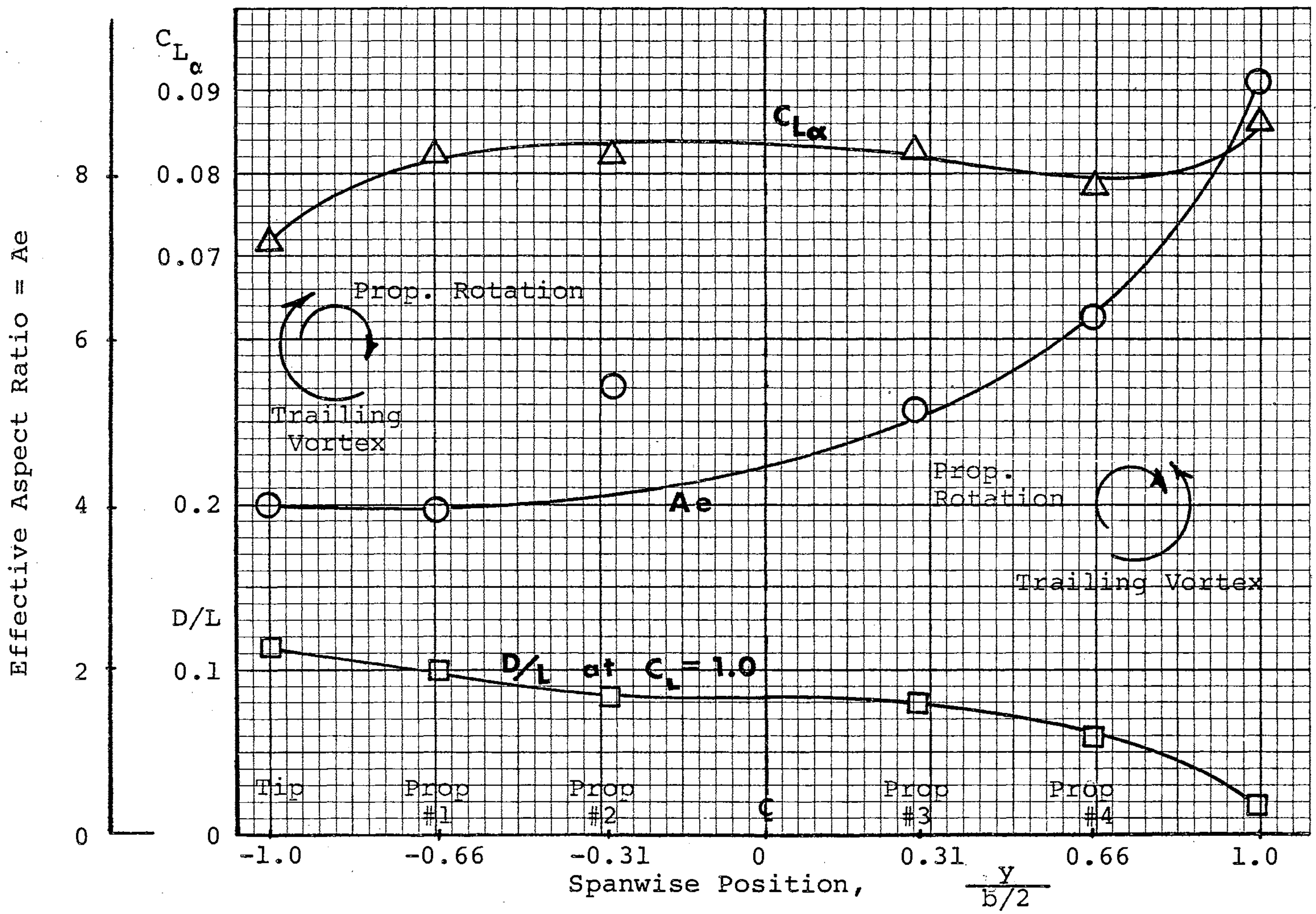

Figure 53. Effect of Propeller Position on Wing Characteristics

performance. In each case listed, there is only one propeller operating; it is operating at the spanwise position listed. All points plotted in Figure 53 correspond to $N = 175$ or 188 r.p.s. and $T_C = .42$ or .65, except the ones corresponding to the left-hand wingtip ($\frac{y}{b/2} = -1.0$). These points are for the propeller turning in the counter-vortex direction at less than windmill speed and at negative thrust (speed is about 70 r.p.s. less than windmill speed, and $T_C \approx -0.8$).

In considering the effect of wing lift characteristics, distinction must be made between the two effects of power:

1. Increased slipstream velocity.
2. Rotation of slipstream.

The effects of (1) were discussed above; i.e., as the slipstream velocity increases, the wing C_L increases (at any given α). The effect of (2) is that the wing is experiencing a lower angle of attack in one portion of the slipstream and a higher angle of attack in the other portion.

The effect of these two factors is sketched in Figure 54. It will be noted that experimental data from reference 15 confirms this analysis. More recent data in reference 16 indicates the same effects. The result of (2) is that the effects of the $\Delta\alpha$ and $-\Delta\alpha$ due to slipstream practically cancel for the propeller located inboard. However, when the propeller is near or at the

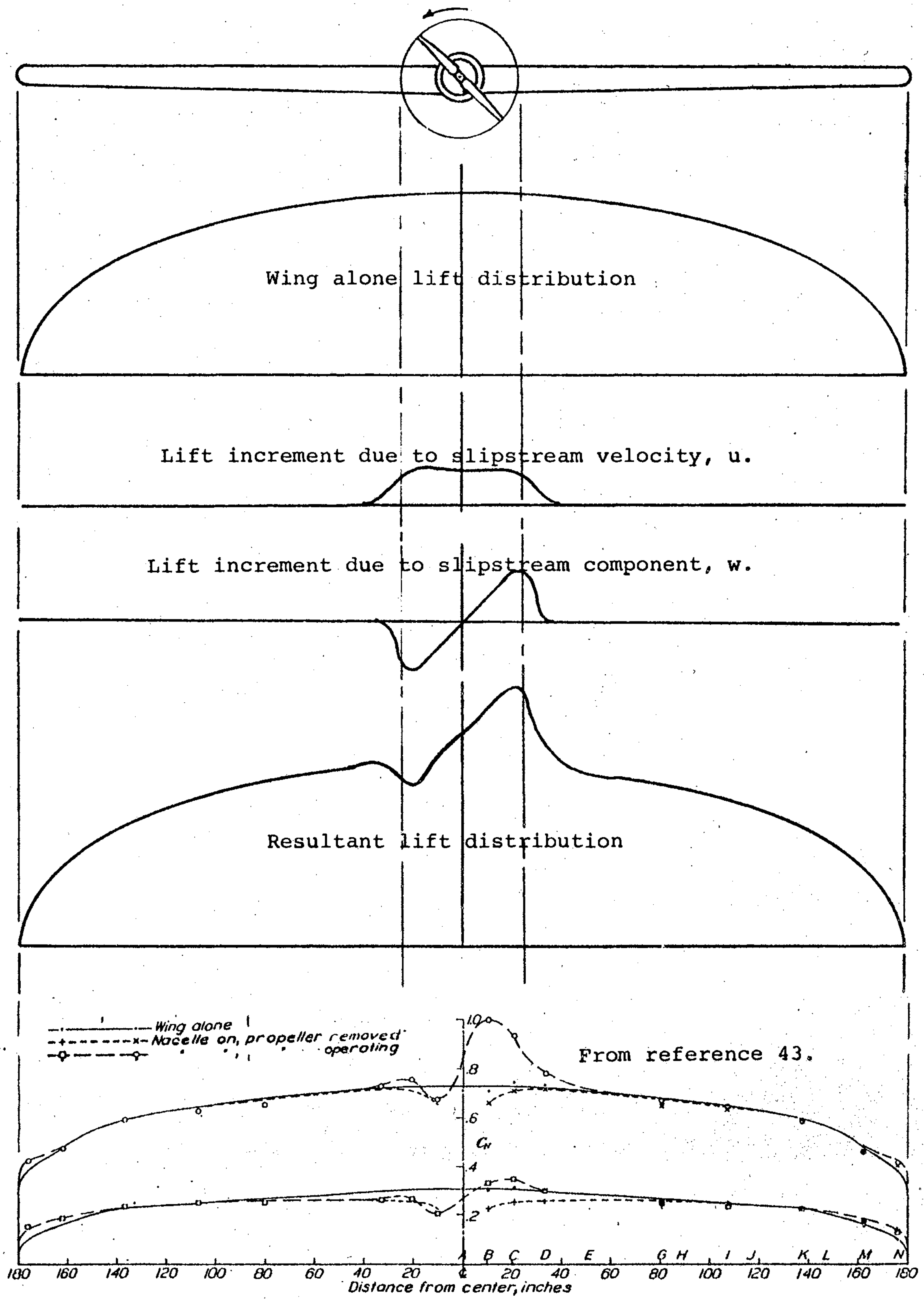

Figure 54. Effect of Propeller Operation Span-Load

tip, so that part of the slipstream is beyond the wingtip, the effects do not cancel. If the propeller at the tip is turning in the vortex-direction so that the propeller blades move down in front of the wing, there is a decrease in lift of the wing; the effect is like washout. If the wingtip propeller is turning in the counter-vortex direction, so that the propeller is moving up in front of the wing, there is an increase in the lift of the wing; the effect is like washin. For this reason, the effect of propeller location on lift is practically confined to locations near the wingtips (see C_{L_α} in Figure 53).

The most notable effects of propeller spanwise position are those involving drag. Figure 53 shows a marked increase in effective aspect ratio as a counter-vortex turning propeller is moved toward the wingtip (4.6 with propeller on centerline; 9.1 at wingtip). The effective aspect ratio decreases as a pro-vortex turning propeller is moved toward the wingtip. There is a corresponding effect on drag.

Table V and Figure 43 summarize the effective aspect ratio and the induced drag due to wingtip-mounted impeller or propeller. The values tabulated and plotted were obtained by fitting straight lines to the graphs of C_D vs C_L^2. The equation of the line is $C_D = C_{D_p} + m\, C_L^2$, where

$$m = \frac{\Delta\ C_D}{\Delta\ C_L^2} = \frac{1}{\pi\ Ae_w}.$$

The change in the induced drag due to a wingtip rotor may be explained by Figure 55. In the case of the vortex-direction rotation, the downwash due to the rotor combines with the wing downwash to produce greater downwash at the wing and an increase in the induced drag. Figure 55 also shows that a counter-vortex rotation of the rotor produces a smaller downwash at the wing, and a smaller induced drag.

In terms of the trailing vortex strength, the vortex-direction turning rotor may be called a "vortex source", while the counter-vortex turning rotor may be called a "vortex sink".[2] These functions are the results of the rotating vortex sheet downstream of the propeller which are superimposed on the shed vortex sheet of the wing. The wing vortex sheet is thus attenuated or amplified. It is possible to conceive of counter-vortex rotating propellers distributed along a wing of sufficient strength to absorb completely the vortices shed by the wing, resulting in infinite effective aspect ratio.

It will be noticed, in Table V, that in some cases there is a decrease of parasite drag accompanying the applications of power. There may be some error in correcting for direct thrust effects. There is also some "cleaning-up" of wing flow and nacelle flow due to the propeller slipstream. Similar effects are noted in references 54 and 5. The effect is more pronounced with the

---

[2]"Vortex source" and "vortex sink" were used in this sense by Maurice Roy, Director of the O.N.E.R.A. See his article in reference 51.

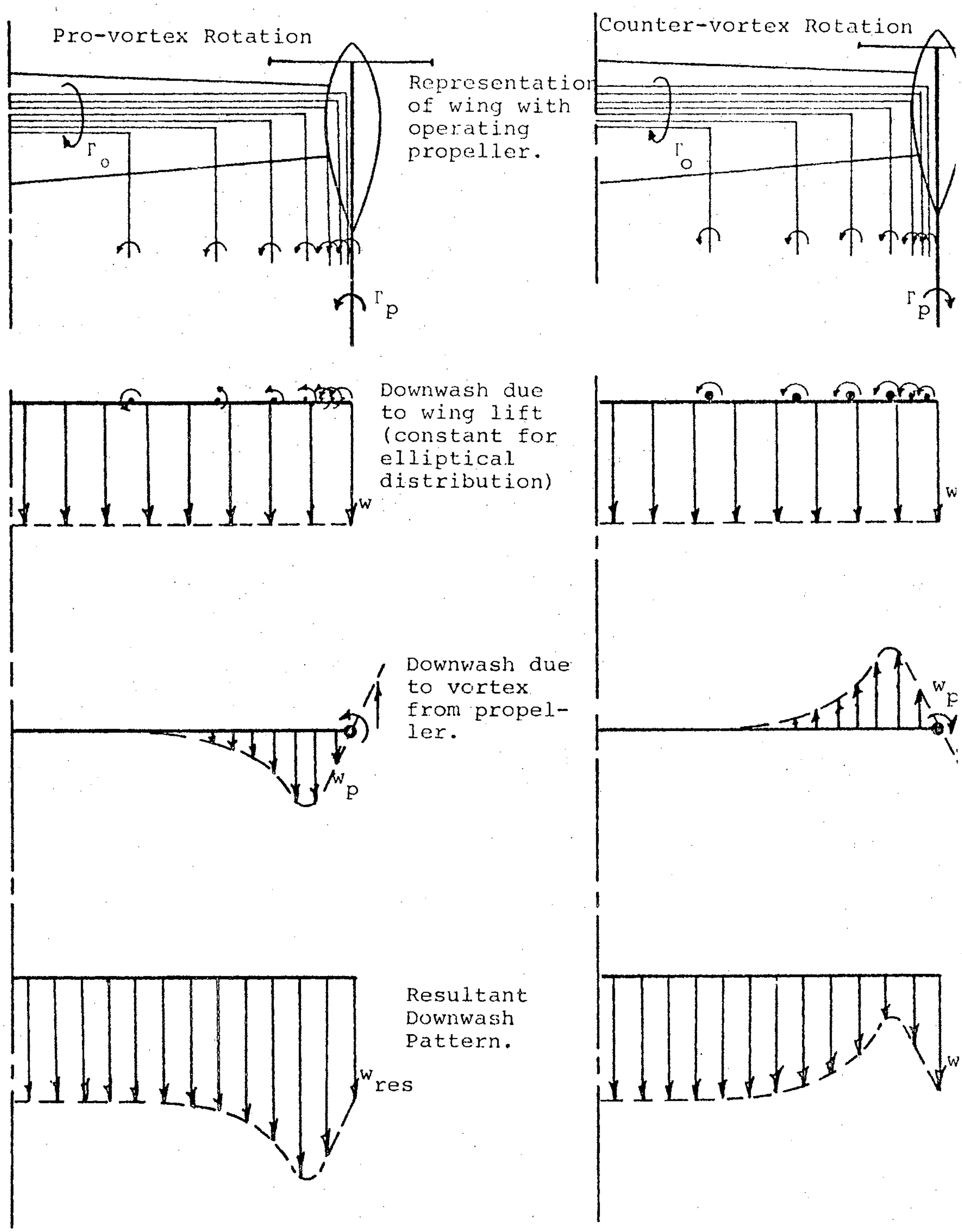

Figure 55. Representation of Changing Pattern of Downwash Due to Propeller-Produced Tip Vortex

propeller than with the impeller (probably due to the higher slipstream velocity of the propeller).

Effect on Aircraft Performance

In order to provide an example of the effects of wingtip propellers on aircraft performance, a hypothetical aircraft has been modified. The aircraft is an anti-submarine warfare (ASW) aircraft. It is a mid-wing, twin engine monoplane with fully retractable landing gear. The chief specifications are:

Wingspan	80 ft.
Gross Weight	40,000 lb.
Power Loading	8.34 lb.
Wing Loading	50.2 lb.
Wing Area	796.5 sq. ft.
Aspect Ratio	8.0

Engines: 2 P. and W. R-2800-CB16

Propellers: 13 ft., 4 blades

Additional specifications are contained in reference 39, which contains a detailed description of the design and performance of the airplane.

The drag equation for the airplane was predicted to be $C_D = 0.0188 + 0.0378C_L^2$.

If the engine nacelles and propellers were moved to the wingtips with each propeller turning in the counter-vortex direction, it is reasonable to expect, from the results cited earlier, that the drag equation would be altered to:

$$C_D \approx 0.018 + 0.022\, C_L^2 \quad \text{(Full Throttle).}$$

The power required, at sea-level, has been calculated using these two equations; these curves are plotted in Figure 56. In addition, a part-throttle power-required curve has been plotted in Figure 56. The basis of this curve is that the effective aspect-ratio is a function of T_C. This curve was used to determine the endurance and range improvement using the Brequet formulas. The changes in sea-level performance resulting from the wingtip propellers are listed in Table IX.

TABLE IX

PERFORMANCE COMPARISON FOR ASW AIRCRAFT

Performance Item	ASW as Designed	With Wingtip Propellers	% Change
Velocities			
Max. Vel.	262 knots	270.5 knots	3.4%
For Max. Range	143.8 knots	139 knots	
For Max. Endur.	108.2 knots	97 knots	
For Best R.C.	142 knots	137 knots	
Best Rate of Climb	1562 fpm.	1750 fpm.	12%
Best Angle of Climb	8.4 deg.	9.7 deg.	15.4%
Max. Range	1 unit	1.165 units	16.5%
Max. Endurance	1 unit	1.27 units	27%

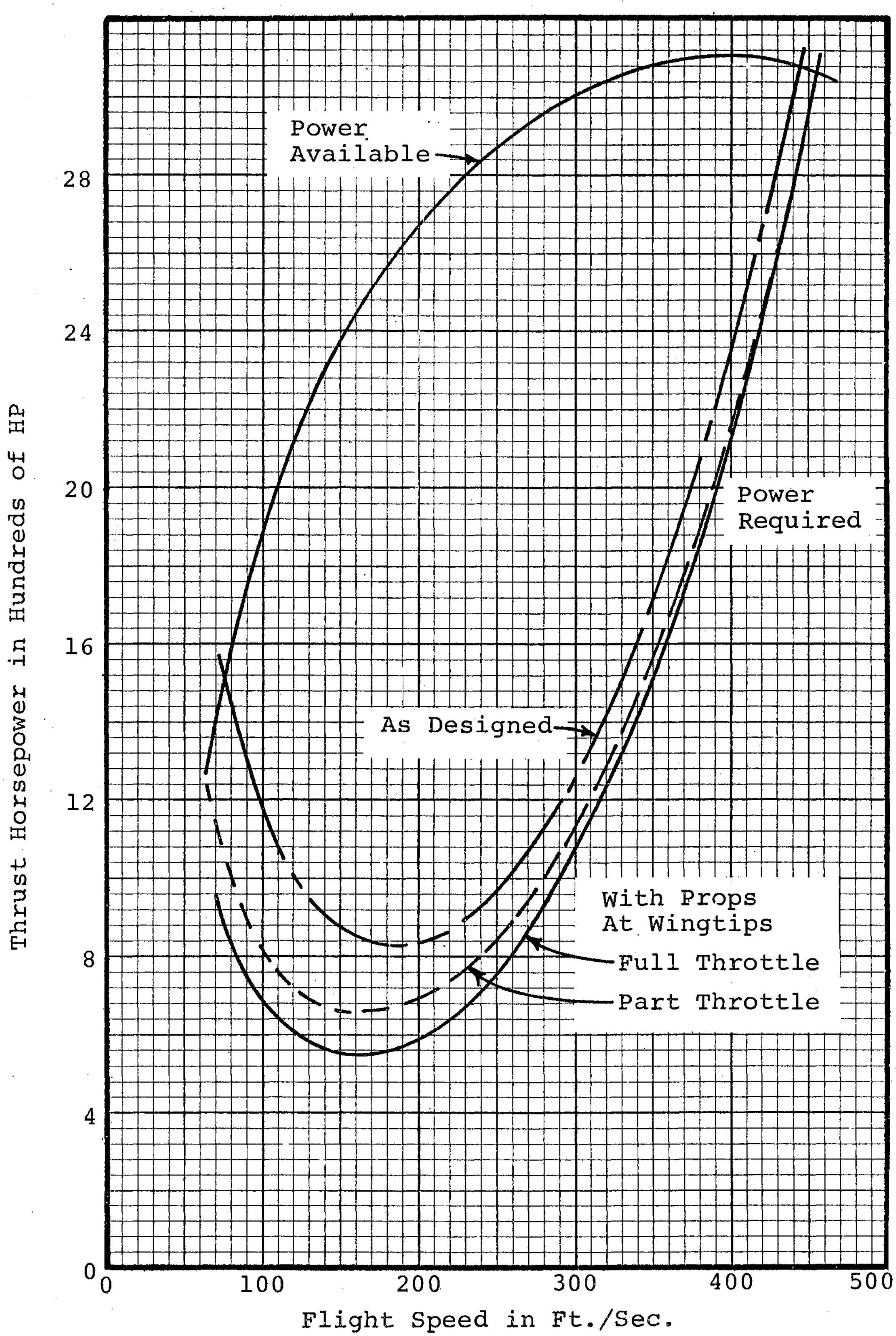

Figure 56. Power Required and Available for Original and Modified ASW Aircraft

It will be noted that this configuration is particularly suited to aircraft of this type -- long range and patrol aircraft. A 16.5% increase in range and a 27% increase in endurance are significant improvements.

The disadvantage of this design change is the problem of trim and control for one-engine-out flight. There will be a weight penalty due to the necessity of adding an oversize vertical tail. The alternative is the weight and complexity of cross shafting or some other method of insuring no inequality of power to the two propellers.

Another, and more feasible, design configuration would be to adopt a four-engine design with two engines at the wingtips and two engines inboard.

Generalized Results

In order to increase the usefulness of the results of this investigation, an attempt has been made to generalize them by examining the relationship between the strength of the vortex of the propeller and that of the wing vortex, together with the concept of the propeller acting as a vortex sink (or source) with respect to shed vortex sheet.

Each blade of a propeller sheds a vortex sheet. This helical vortex sheet combines with those of the other blades to produce a trailing vortex system consisting of two parts - a cylindrical vortex sheet encasing the slipstream and a vortex collinear with the propeller axis of rotation. The cylindrical vortex sheet may be considered to be composed of ring vortices; the result of these vortices is that the slipstream velocity is greater than freestream velocity. The axial vortex produces the rotation of the slipstream core.

The angular velocity, according to Konig (26), is $2\,a'\Omega$, where $\Omega = 2\pi N$ and $a' = \frac{8}{\pi^2}\,\frac{C_Q}{1+a}\,\frac{V}{Nd}$. The maximum tangential velocity is $V_{t_{max}} = \frac{16}{\pi}\,\frac{C_Q}{1+a}\,V$. Measurements indicate that, instead of this maximum tangential velocity occurring at the propeller tip, it occurs at $r/R = 0.4$. V_t falls to approximately zero at $r/R = 1$.

There is, then, a trailing vortex system superimposed on the wing trailing vortex system. Schaffer (44) has shown that the vortices will combine to strengthen the trailing vortex (if they have the same sense) or to decrease the strength (if they have opposite sense).

For a given diameter, the vortex strength of a propeller will be proportional to the blade lift and, therefore, to the propeller thrust.

$$T = T_C \frac{\rho}{2} V^2 \; d^2$$

circulation (i.e., vortex strength of the wing) is proportional to the wing lift.

$$L = C_L \frac{\rho}{2} V^2 \; S$$

$$\frac{\Gamma_{prop.}}{\Gamma_{wing}} = \frac{T}{L} = \frac{T_C\,\rho/2\,V^2 \;\; d^2}{C_L\,\rho/2\,V^2 \;\; d^2} = \frac{T_C \;\; d^2}{C_L \;\; S}$$

This ratio has been used to examine $\Delta C_D / C_L$ and $\Delta C_D / C_D$. Figure 57 shows the dependence of $\Delta C_D / C_D$ on $\frac{T_C d^2}{C_L S/2}$. There appears to be a functional relation and a single curve has been fit to the data.

Data for the impeller is also plotted in Figure 57. As would be expected, these data do not fit the propeller data for the reason that the rotation of the slipstream of the impeller is a direct function of N, rather than of thrust.

Figure 58 shows the relation between $\Delta C_L / C_L$ and $\frac{T_C d^2}{C_L S/2}$. It is not clear that there is as strong dependence of ΔC_L on the parameter. It does appear that ΔC_L is roughly proportional to $\frac{T_C d^2}{S}$.

It is felt that the strong dependence of span efficiency factor, $e = \frac{A_e}{A}$, on the positioning of the propeller on the wing, as shown in Figure 53, is a general result. Although the wing is common to all tests, the nacelle shapes are all different, and some tests are with full-wing and fuselage and others are from a reflection-plane wing test without fuselage. The agreement of the values is good.

A similar parameter, $\frac{\Delta C_{D_i}}{C_L^2}$, has been evaluated for various values of $N \frac{d}{b}$, where N is the difference between rotor speed and windmilling speed. It was found that $(\Delta C_{D_i} / C_L^2)$ varies with the cube root of $(N \frac{d}{b})$. This relation is shown graphically in Figure 59.

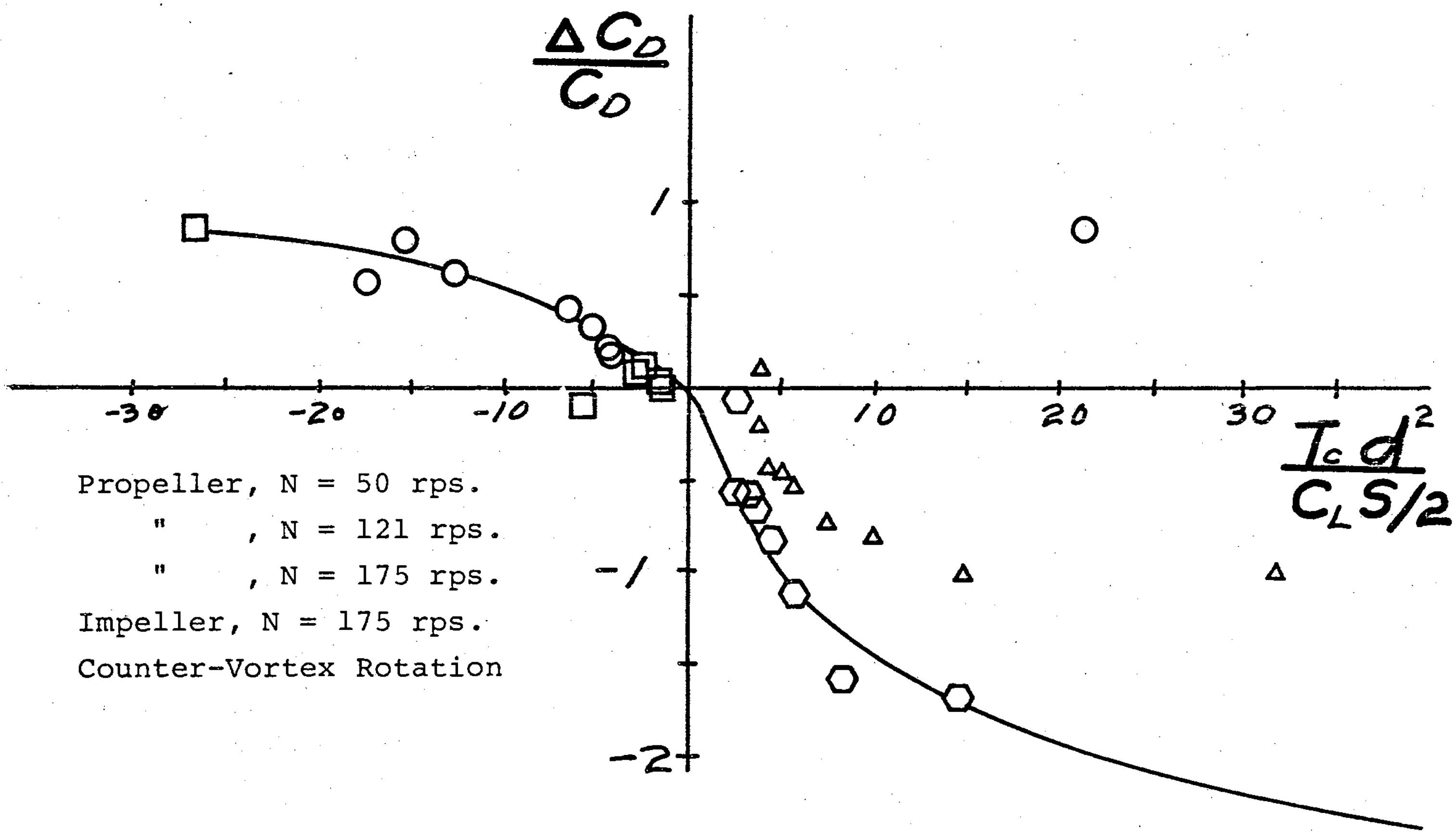

Figure 57. Correlation of Drag Coefficient Increment Due to Wingtip-Mounted Propellers

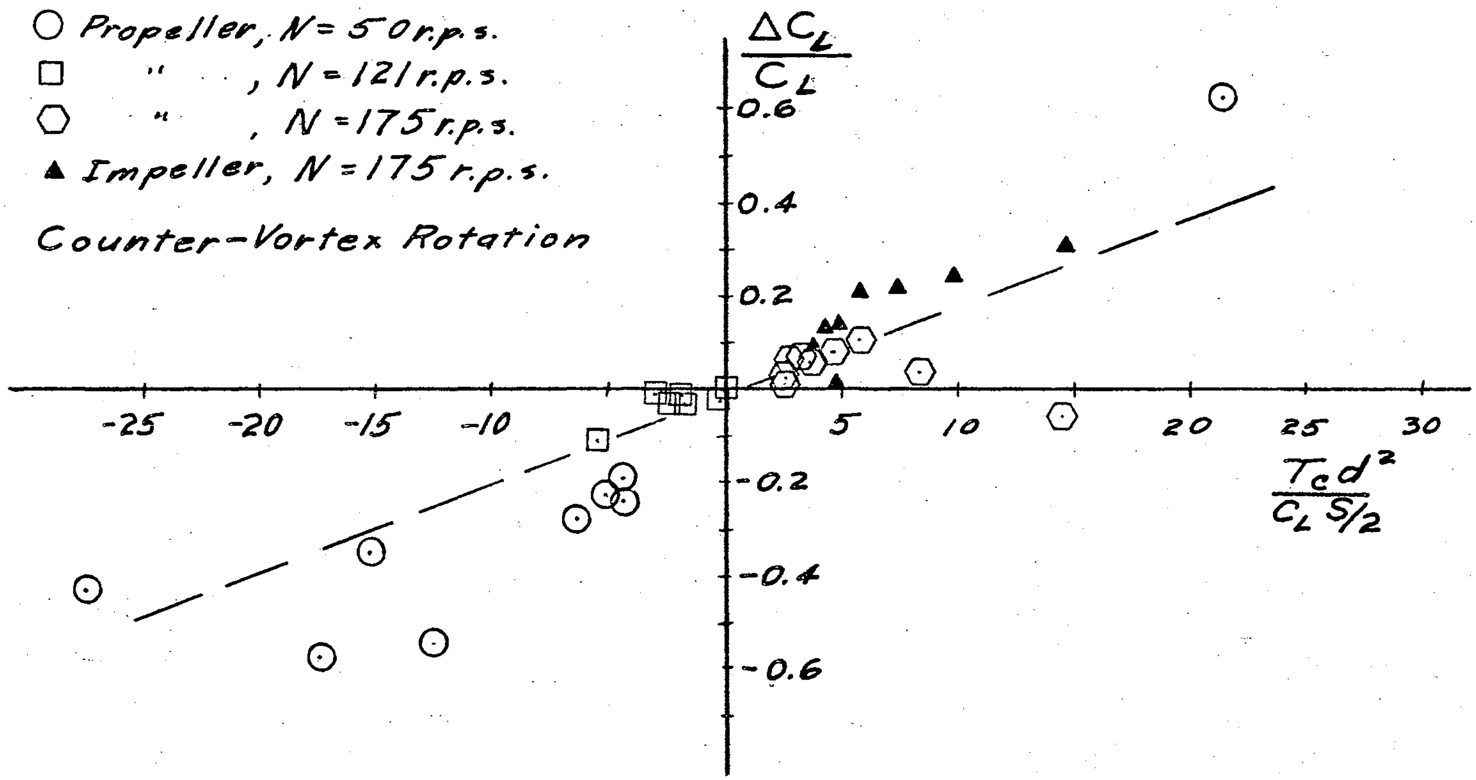

Figure 58. Correlation of Lift Coefficient Increment Due to Wingtip Propellers

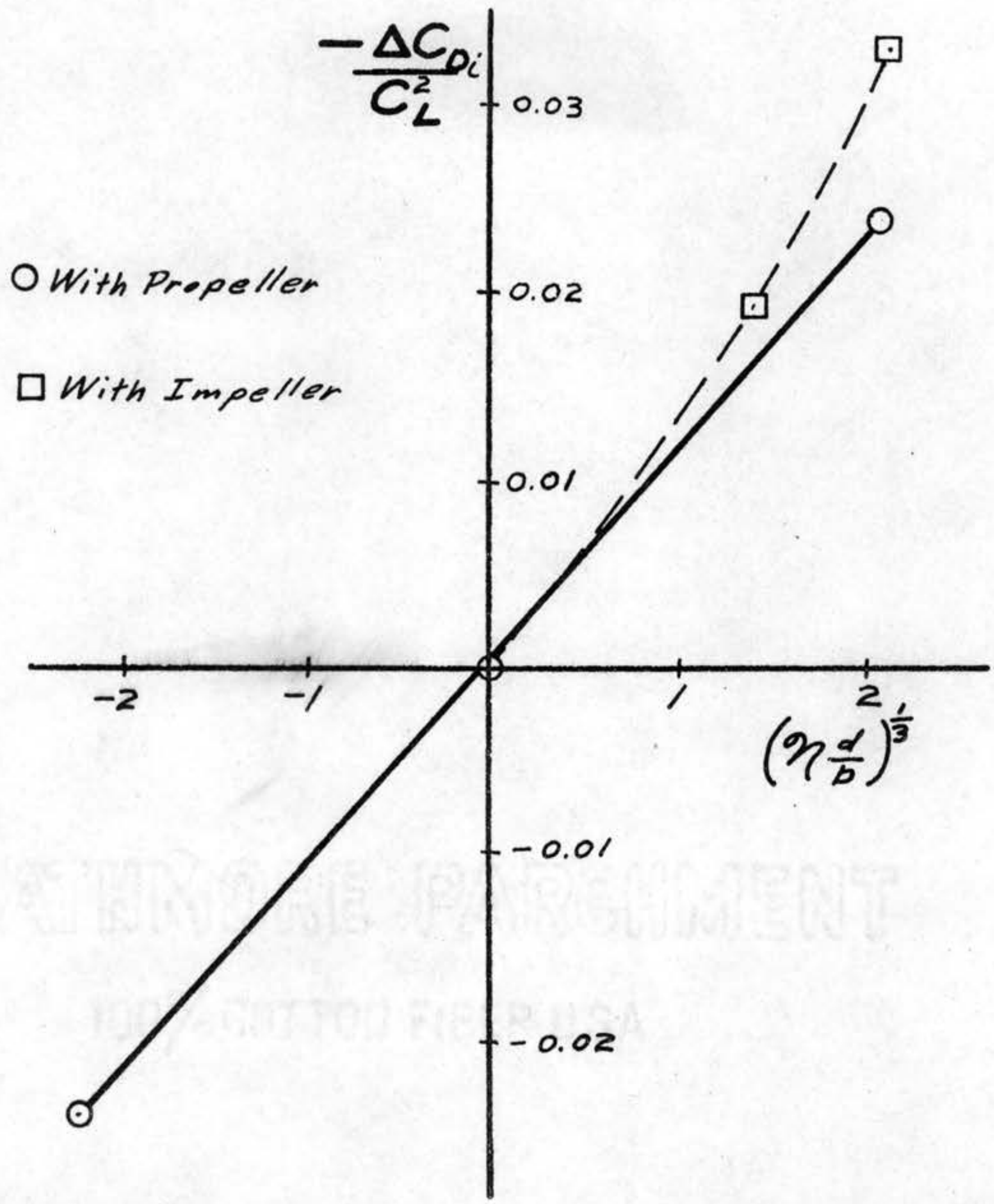

Figure 59. Effect of Propeller Speed and Size Ratio on Induced Drag Coefficient Increment

CHAPTER V

SUMMARY AND CONCLUSIONS

The traditional method of simulating higher aspect ratio has been examined; i.e., the use of end-plates. A new method, that of using mechanical rotors at the wing-tips, has been proposed and tested. The principal conclusions are:

1. End-plates are not effective in obtaining the desired effect; i.e., increasing effective aspect ratio and decreasing induced drag.
2. The use of propellers mounted at the wingtips can produce simultaneous lift increase and drag decrease. The fractional changes in both drag coefficient and lift coefficient are functions of $\frac{T_C \, d^2}{C_L \, S}$.

The detailed results of the investigation include the following:

1. End-plates increase the effective aspect ratio of the wing. They function by shifting the wing-loading (more lift

toward the tip) and by decreasing the downwash.

2. For STOL aircraft, in which operation at high C_L is important, end-plates are effective in decreasing take-off distance but they do not decrease landing distance. In some cases their use will increase landing distance.
3. It is more effective to use the same airfoil area as an extension of the wingspan than it is to use it in the form of end-plates.
4. Energy may be employed to affect the wing's flow field and lift distribution by mounting the aircraft's propellers at the wingtips.
5. Use of a rotor turning in the direction opposite to that of the wing's trailing vortex shifts the core of the trailing vortex outboard and downward.
6. Use of a pro-vortex turning rotor (or counter-vortex propeller turning at less than windmill speed) moves the core of the trailing vortex inboard.
7. Wingtip configuration and/or rotor rotation have little effect on the position of the vortex trailing from the outboard

end of a deflected flap.

8. There is a mutual dependence between vortex span and effective aspect ratio. As one increases, the other does also. Actual functional relation is not yet clearly defined.
9. Effect of power on C_L is mainly due to higher slipstream velocity for inboard propellers. However, for propellers at the wingtips, the effect is chiefly due to the altered angle of attack in, and adjacent to, the slipstream as well as to increased slipstream dynamic pressure.
10. A counter-vortex turning propeller decreases wing drag (mainly, induced drag); a vortex-turning propeller increases drag. The rotor at the tip serves as a trailing vortex sink (counter-vortex) or source (vortex).
11. The effectiveness of the propeller in affecting the lift and drag increases as it is moved outboard toward the wingtip.
12. Counter-vortex propellers at the wingtips improve an aircraft's climb and cruise performance compared to conventional positioning.

The following recommendations are made for further work in this field:

1. It would be desirable to obtain more data on the relation between vortex span and effective aspect ratio. Additional experimental work using a rotating or non-rotating vorticity meter is needed.
2. It would be interesting to see whether a wingtip jet, with variable amounts of vorticity, would have similar effects to those found with the propellers.
3. Additional data with wings of different aspect ratio, taper ratio, and d/b would help establish the relation between $\frac{\Delta C_D}{C_D}$ and $\frac{T_C}{C_L}\frac{d^2}{S}$.

SELECTED BIBLIOGRAPHY

1. Betz, A. Behaviour of Vortex Systems. NACA Technical Memorandum 713, Washington, June, 1933.

2. Betz, A. "How Originates a Vortex in a Slightly Viscous Fluid?" Naturwissenschaften, Vol. 37, No. 9, pp. 193-196, 1950. Translated by F. Wagner and published as UWER65, University of Wichita, Wichita, Kansas, July, 1952.

3. Bird, John D. "Visualization of Flow Fields by Use of a Tuft Grid Technique," Journal of the Aeronautical Sciences, Vol. 19, No. 7, July, 1952.

4. Bird, J. D., and D. R. Riley. Some Experiments on Visualization of Flow Fields Behind Low Aspect Ratio Wings by Means of a Tuft Grid. NACA Technical Note 2674, Washington, May, 1952.

5. Brenckmann, M. E. "Experimental Investigation of the Aerodynamics of a Wing in a Slipstream," Journal of the Aeronautical Sciences, Vol. 25, No. 5, p. 324, May, 1958. Also published as U.T.I.A. Tech. Note 11, Toronto, April, 1957.

6. Clements, Harry R. "An Investigation of Canted Adjustable End-Plates for the Control of Drag." M. S. thesis, University of Wichita, April, 1954.

7. Clements, Harry R. "Canted Adjustable End-Plates for the Control of Drag," Aeronautical Engineering Review, Vol. 14, No. 7, July, 1955.

8. Davidson, Marvin. "Information for Users of the Walter H. Beech Low-Speed Wind Tunnel," Aeronautical Engineering Department, Wichita State University, Wichita, July, 1966.

9. Dommasch, D. O., S. S. Sherby, and T. F. Connolly. Airplane Aerodynamics, 3rd ed. New York: Pitman Publishing Corp., 1961.

10. Durand, W. F. A Proof of the Theorem Regarding the Distribution of Lift Over the Span for Minimum Induced Drag. NACA Report 349, Washington, 1929.

11. Eisenbuth, J. J., and B. W. McCormick. "An Observation on the Vortex System of Dual-Rotation Propellers," Readers Forum -- Journal of the Aeronautical Sciences, June, 1953.

12. Ellis, N. D. A Computer Study of a Wing in a Slipstream. UTIAS Technical Note 101, Institute for Aerospace Studies, University of Toronto, February, 1967.

13. Fage, A., and F. C. Johansen. "The Structure of Vortex Sheets," Philosophical Magazine, S. 7, Vol. 5, No. 28, February, 1928.

14. Franke, A., and F. Weining. The Effect of the Slipstream on an Airplane Wing. NACA Technical Memorandum 920, November, 1939.

15. Garbell, Maurice A. "Theoretical Principles of Wing-Tip Fins for Tailless Airplanes and Their Practical Application," Journal of the Aeronautical Sciences, Vol. 13, No. 10, October, 1946.

16. Gillis, C. L., E. C. Polhamus, and J. L. Gray. Charts for Determining Jet-Boundary Corrections for Complete Models in 7 x 10 Closed Rectangular Wind Tunnels. NACA Wartime Report L-123 (ARRL5G31), Washington, 1945.

17. Glauert, H. The Elements of Aerofoil and Airscrew Theory. Cambridge University Press, 1926.

18. Goldstein, S., ed. Modern Developments in Fluid Dynamics, Vol. II. New York: Dover Publications, Inc., 1965.

19. Graham, E. W., P. A. Lagerstrom, R. M. Licher, and B. J. Beane. "A Preliminary Theoretical Investigation of the Effects of Propeller Slipstream on Wing Lift." Report No. S M-14991, Santa Monica, California: Douglas Aircraft Co., November, 1953.

20. Hamelet, Jean H. "Opposite Propeller Rotation--Shall it be Inboard or Outboard?" Aviation, May, 1943.

21. Hemke, Paul E. Drag of Wings With End Plates. NACA Report 267, Washington, 1927.

22. Hoerner, S. F. Fluid-Dynamic Drag, publ. by author, New Jersey, 1958.

23. Hopkins, E. J., S. J. Keating, and A. Bondettini. Photographic Evidence of Streamwise Arrays of Vortices in Boundary-Layer Flow. NASA Technical Note D-328, Washington, 1962.

24. Hopkins, E. J., and N. E. Sorensen. "A Device for Vortex-Core Measurements," Journal of the Aeronautical Sciences, Vol. 23, No. 4, p. 396, April, 1956.

25. von Karman, Theodore. Aerodynamics, Ithaca, N. Y.: Cornell University Press, 1954.

26. Koning, C. "Influence of the Propeller on Other Parts of the Airplane Structure," Aerodynamic Theory, Vol. IV (W. F. Durand, ed.), Berlin: Julius Springer, 1935.

27. Lanchester, F. W. Aerodynamics. London: Archibald Constable and Co., 1907.

28. Lowry, J. G, and R. D. Vogler. Wind Tunnel Investigation at Low Speeds to Determine the Effect of Aspect Ratio and End Plates on a Rectangular Wing With Jet Flaps Deflected 85 Degrees. NACA Technical Note 3863, Washington, 1956.

29. Mangler, W. The Lift Distribution of Wings With End Plates. NACA Technical Memorandum 856, Washington, April, 1938.

30. May, D. M. "The Development of a Vortex Meter." Thesis, Pennsylvania State University, University Park, Pa., June, 1964.

31. Millikan, C. B. Aerodynamics of the Airplane. New York: John Wiley and Sons, 1941.

32. von Mises, Richard. Theory of Flight. New York: McGraw-Hill Book Co., 1945.

33. Morris, P. E. Three Dimensional Wind Tunnel Test to Determine the Effect of End Plates on Induced Drag. UWAR 29, University of Wichita, Wichita, Kansas, October, 1950.

34. Morris, P. E. and V. TenEyck. An Analysis of the Effects of End Plates and Circulation Control for Different Aspect Ratios on the Take-Off and Landing Distances of an L-19 Type Airplane. UWER 50, University of Wichita, Wichita, Kansas, November, 1951.

35. Munk, M. M. Note on Vortices and on Their Relation to the Lift of Airfoils. NACA Technical Note 184, Washington, 1924.

36. Polhamus, E. C. Jet-Boundary-Induced-Upwash Velocities for Swept Reflection-Plane Models Mounted Vertically in 7- by 10-foot, Closed, Rectangular Wind Tunnels. NACA Technical Note 1752, November, 1948.

37. Pope, Alan. Basic Wing and Airfoil Theory. New York: McGraw-Hill Book Company, 1951.

38. Pope, A., and J. J. Harper. Low-Speed Wind Tunnel Testing. New York: John Wiley and Sons, 1966.

39. Razak, Kenneth. An Analysis of the Effects of Boundary-Layer-Control and Propeller Configuration on the Performance of an ASW Type Airplane. UWES No. 155, University of Wichita, Wichita, Kansas, August, 1954.

40. Razak, K., and M. H. Snyder. A Review of the Planform Effects on the Low-Speed Aerodynamic Characteristics of Triangular and Modified Triangular Wings. NASA Contractor Report 421, Washington, April, 1966.

41. Rethorst, S. "Lift on a Wing in a Propeller Slipstream as Related to Low Speed Flight," Aeronautical Engineering Review, Vol. 15, No. 10, pp. 42-48, October, 1956.

42. Riley, D. R. Wind-Tunnel Investigation and Analysis of the Effects of End Plates on the Aerodynamic Characteristics of an Unswept Wing. NACA Technical Note 2440, Washington, August, 1951.

43. Robinson, R. G., and W. H. Herrnstein. Wing-Nacelle-Propeller Interference for Wings of Various Spans. Force and Pressure Tests. NACA Report 569, Washington, 1936.

44. Schaffer, Allan. "A Study of Vortex Cancellation," Journal of the Aero/Space Sciences, Vol. 27, No. 3, P. 193, March, 1960.

45. Schrenk, O. Model Experiments on the Forces and Moments Acting on an End Plate Fitted to a Wing. NACA Technical Memorandum 855, Washington, April, 1938.

46. Sherman, Albert. "An Integrator for Evaluating the Downwash From a Span-Loading Curve," Journal of the Aeronautical Sciences, Vol. 5, No. 4, pp. 148-150, February, 1938.

47. Sivells, J. C., and O. J. Deters. Jet-Boundary and Planform Corrections for Partial-Span Models With Reflection Plane, End Plate, or No End Plate in a Closed Circular Wind Tunnel. NACA Report 843, Washington, 1946.

48. Smelt, R., and H. Davies. Estimation of Increase in Lift due to Slipstream. Aeronautical Research Council, R. and M. 1788, London, 1937.

49. Smith, D. R. L. Fluid Mechanics. London: J. Houghton, 1960.

50. Snyder, M. H. A Non-Rotating Vorticity Meter, AR66-3, Wichita State University, Wichita, Kansas, 1966.

51. Snyder, M. H., ed. On the Theory of Delta Wings, AR66-4, Wichita State University, Wichita, Kansas, 1966.

52. Spreiter, J. R., and A. H. Sacks. "The Rolling up of the Trailing Vortex Sheet and its Effect on the Downwash Behind Wings." Institute of the Aeronautical Sciences, 18th Annual Meeting, January, 1950, Preprint No. 250. Also published in the Journal of the Aeronautical Sciences, Vol. 18, No. 1, pp. 21-32, January, 1951.

53. Stalter, J. L. Investigation of the Basic Aerodynamic Characteristics of a Circulation Control, Research Model. UWER 187, pt. 1, University of Wichita, Wichita, Kansas, December, 1956.

54. Stalter, J. L., and R. K. Wattson. Effects of Power on the Aerodynamic Characteristics of a Circulation Control, Research Model. UWER 187, p. 2, University of Wichita, Wichita, Kansas, March, 1957.

55. Swanson, R. S., and T. A. Toll. Jet-Boundary Corrections for Reflection-Plane Models in Rectangular Wind Tunnels, NACA Report 770, Washington, 1943.

56. Theodorsen, Theodore. Theory of Propellers. New York: McGraw-Hill Book Company, 1948.

57. Truitt, Robert W. "Comments on Vortex-Core Measurements," Journal of the Aeronautical Sciences, Readers' Forum, Vol. 23, No. 9, September, 1956.

58. Wentz, W. H., and M. C. McMahon. An Experimental Investigation of the Flow Fields About Delta and Double-Delta Wings at Low Speeds. Report AR65-2, Wichita State University, August, 1965.

APPENDIX

RESULTS OF EXPERIMENTAL PROGRAM

This appendix presents results of the experimental program additional to those presented in Chapters III and IV.

Tuft Grid Survey

In order to interpret the results of the tuft grid survey, 140 of the pictures were printed. Examples are shown in Figures 60 and 61. Figure 60 illustrates how clearly the position of both the tip vortex and the flap outboard vortex may be located.

Figure 61 illustrates the tracing of the vortex trajectory. In this figure the impeller is mounted on the wing. In the left column of pictures (a, d, g, j, and m), the impeller is turning at 175 r.p.s. in the vortex direction. In the center column of pictures (b, e, h, k, and n), the impeller is stationary. In the right column of pictures (c, f, i, l, and o) the impeller is turning at 175 r.p.s. in the counter-vortex direction.

Performance Calculations

The power required for the ASW airplane, with and without modification, was calculated using the 1620 computer. The results are listed in Tables X and XI. Table XII tabulates the significant values for power required for part-throttle operation. The improvement in induced drag is a function of power. Thus, in level flight, it is a function of flight speed (e.g., at $V = 100$ ft./sec., $C_{D_i} \approx .026\ C_L^2$; at $V = 300$ ft./sec., $C_{D_i} \approx .029\ C_L^2$). The computer program for the parabolic drag airplane was used repeatedly at various values of m to obtain the part-throttle power required curve.

Figure 85 is the sea-level climb performance curve for the aircraft.

Balance Measurements

The balance data taken during the test program were reduced using the 1620 computer. The reduced data in coefficient form were read-out in two forms -- corrected for tunnel boundary and uncorrected. Since changes due to power were of primary interest (rather than absolute values) and since the changes were to be coordinated with flow field data, it was decided to use the uncorrected answers throughout.

The answers were also corrected to remove the apparent lift, drag, and pitching moment due to thrust.

The graphical presentation of the coefficients is done two ways. Most of the answers uncorrected for thurst were plotted using the 1620 computer and a Calcomp plotter. In addition, the data which were manually corrected for thrust were manually plotted.

TABLE X

POWER REQUIRED, ASW AIRPLANE

CD = .0188+ .0378(CL**2), AREA = 796.5SQ.FT.

SEA-LEVEL ALTITUDE 40,000 LBS. GROSS WEIGHT

VEL FT/SEC	VEL KNOTS	LIFT COEF	DRAG POUNDS	PWR REQ HP
50.00	29.6	16.901	25600.13	2327.28
75.00	44.4	7.511	11458.17	1562.47
100.00	59.2	4.225	6566.87	1193.97
125.00	74.0	2.704	4366.97	992.49
150.00	88.8	1.877	3239.94	883.62
175.00	103.6	1.379	2631.20	837.20
200.00	118.4	1.056	2309.10	839.67
225.00	133.3	.834	2162.97	884.85
250.00	148.1	.676	2134.52	970.24
275.00	162.9	.558	2190.70	1095.35
300.00	177.7	.469	2311.59	1260.86
325.00	192.5	.400	2484.65	1468.20
350.00	207.3	.344	2701.65	1719.23
375.00	222.1	.300	2957.00	2016.13
400.00	236.9	.264	3246.80	2361.30
425.00	251.8	.233	3568.26	2757.29
450.00	266.6	.208	3919.36	3206.75
475.00	281.4	.187	4298.57	3712.40
500.00	296.2	.169	4704.76	4277.05
525.00	311.0	.153	5137.05	4903.54
550.00	325.8	.139	5594.74	5594.74
575.00	340.6	.127	6077.31	6353.55
600.00	355.4	.117	6584.33	7182.90

TABLE XI

POWER REQUIRED, MODIFIED ASW AIRPLANE

CD = .0180+ .0220(CL**2), AREA = 796.5SQ.FT.

SEA-LEVEL ALTITUDE 40,000 LBS. GROSS WEIGHT

VEL FT/SEC	VEL KNOTS	LIFT COEF	DRAG POUNDS	PWR REQ HP
50.00	29.6	16.901	14916.25	1356.02
75.00	44.4	7.511	6706.36	914.50
100.00	59.2	4.225	3888.80	707.05
125.00	74.0	2.704	2646.02	601.36
150.00	88.8	1.877	2036.01	555.27
175.00	103.6	1.379	1736.01	552.36
200.00	118.4	1.056	1611.18	585.88
225.00	133.3	.834	1597.12	653.37
250.00	148.1	.676	1659.91	754.50
275.00	162.9	.558	1780.30	890.15
300.00	177.7	.469	1946.71	1061.84
325.00	192.5	.400	2151.83	1271.54
350.00	207.3	.344	2390.88	1521.47
375.00	222.1	.300	2660.60	1814.04
400.00	236.9	.264	2958.72	2151.79
425.00	251.8	.233	3283.62	2537.34
450.00	266.6	.208	3634.12	2973.37
475.00	281.4	.187	4009.34	3462.61
500.00	296.2	.169	4408.61	4007.83
525.00	311.0	.153	4831.42	4611.81
550.00	325.8	.139	5277.37	5277.37
575.00	340.6	.127	5746.15	6007.34
600.00	355.4	.117	6237.51	6804.56

TABLE XII

PART-THROTTLE POWER, MODIFIED ASW AIRPLANE

SEA-LEVEL ALTITUDE 40,000 LBS. GROSS WEIGHT

VEL FT/SEC	VEL KNOTS	LIFT COEF	DRAG POUNDS	PWR REQ HP
CD = .0180+ .0150(CL**2), AREA = 796.5SQ.FT.				
500.00	296.2	.169	4361.29	3964.81
525.00	311.0	.153	4788.50	4570.84
550.00	325.8	.139	5238.26	5238.26
CD = .0180+ .0260(CL**2), AREA = 796.5SQ.FT.				
75.00	44.4	7.511	7908.27	1078.40
100.00	59.2	4.225	4564.88	829.97
125.00	74.0	2.704	3078.71	699.70
375.00	222.1	.300	2708.68	1846.82
400.00	236.9	.264	3000.97	2182.53
425.00	251.8	.233	3321.05	2566.27
CD = .0180+ .0290(CL**2), AREA = 796.5SQ.FT.				
200.00	118.4	1.056	1906.96	693.44
225.00	133.3	.834	1830.83	748.97
250.00	148.1	.676	1849.21	840.55
275.00	162.9	.558	1936.75	968.37
300.00	177.7	.469	2078.17	1133.54

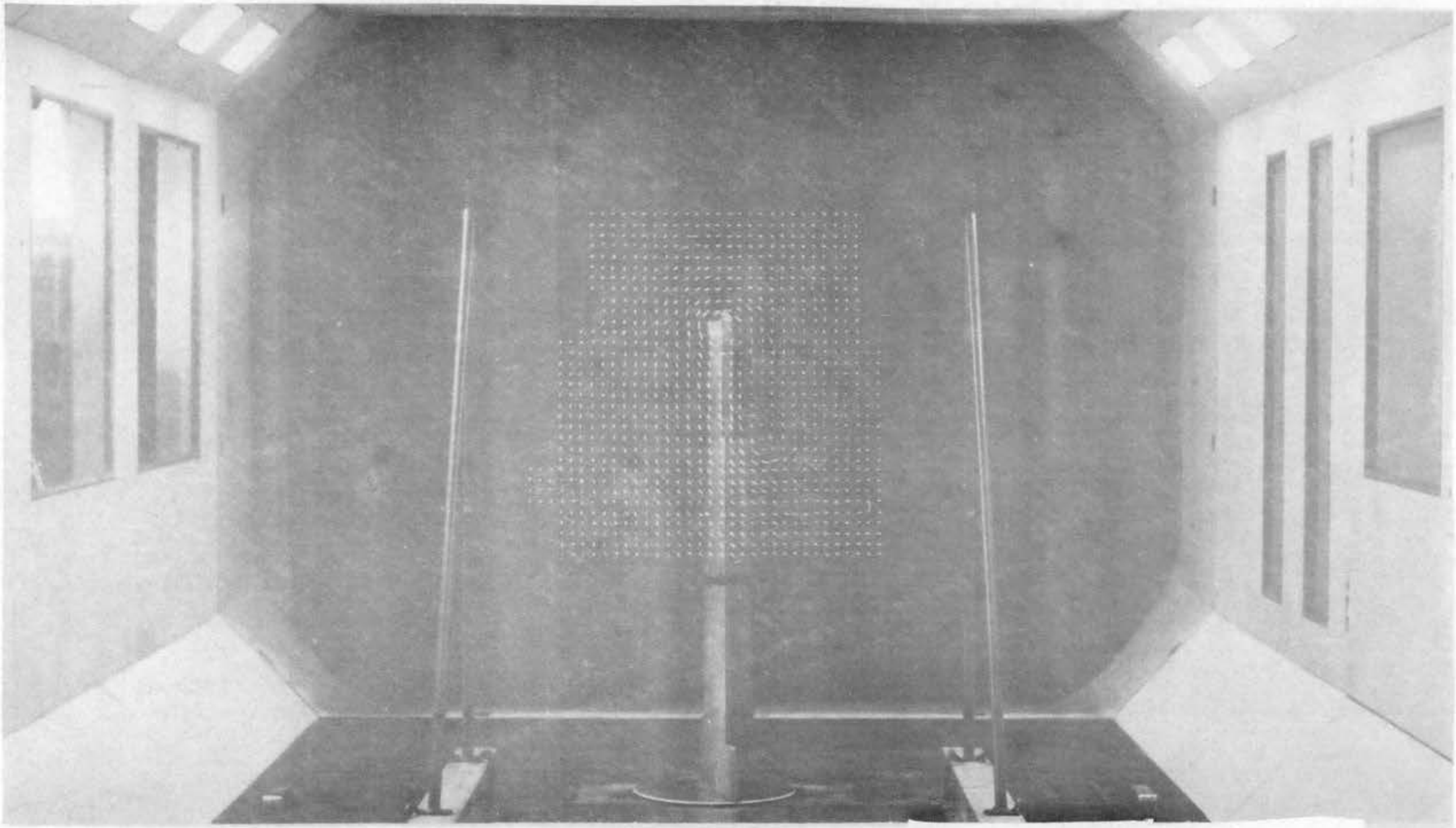

Figure 60. Basic Wing With Plane Tip, $\alpha = 12^\circ$, $\delta_f = 40^\circ$, $x = 12M$

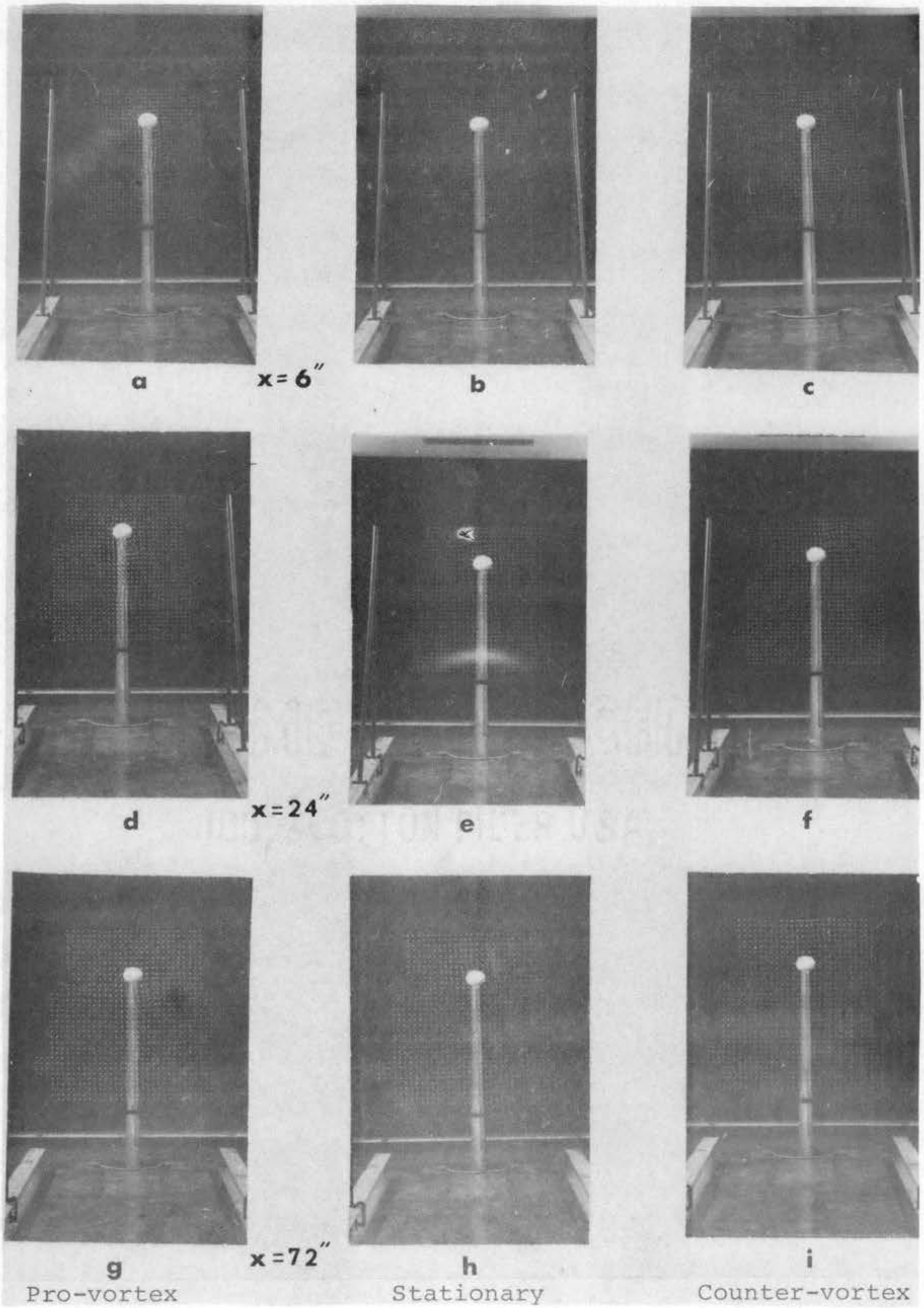

Figure 61. Impeller, $N = 175$ r.p.s., $\alpha = 12$, $\delta_f = 0$

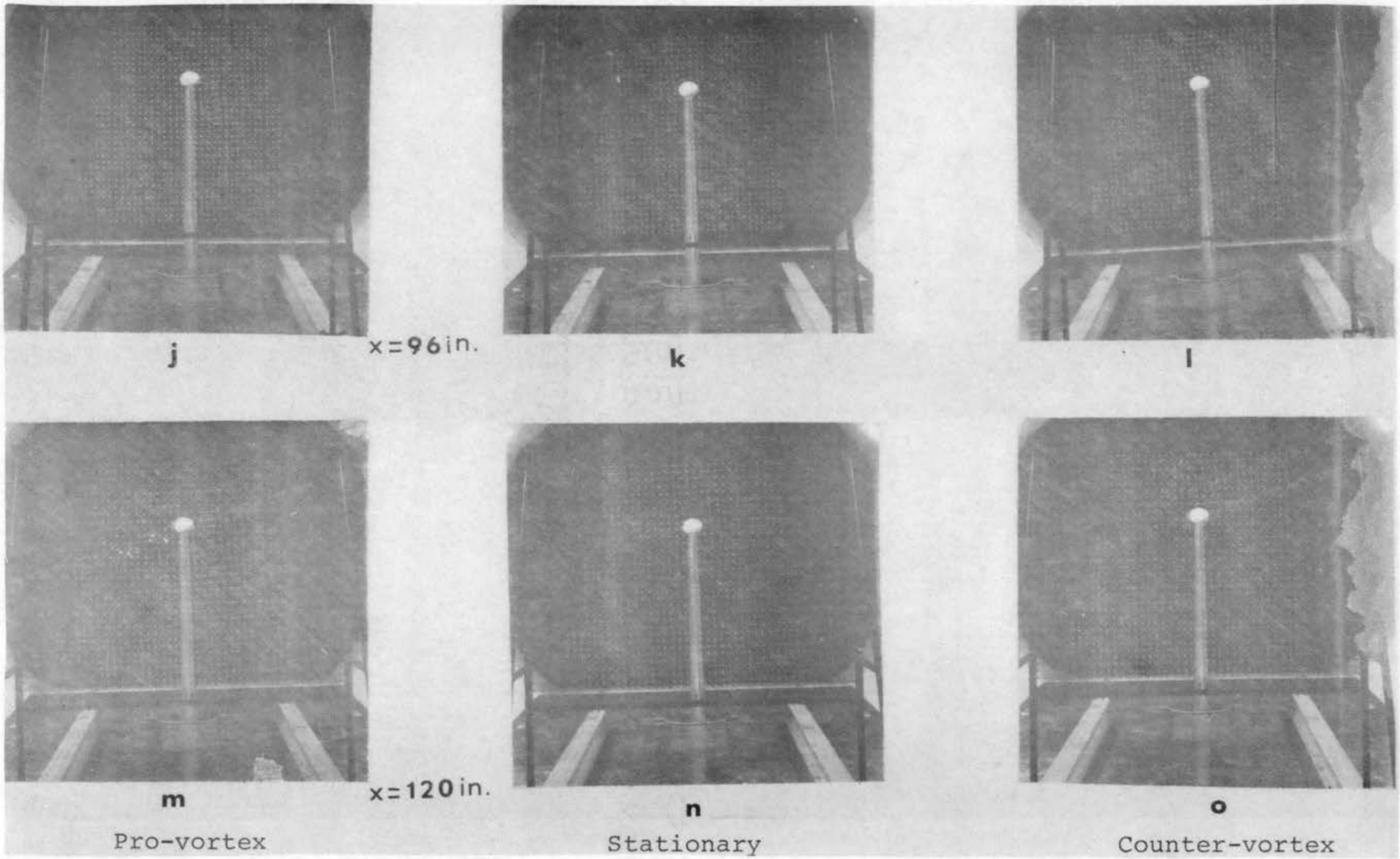

Figure 61. (Continued)

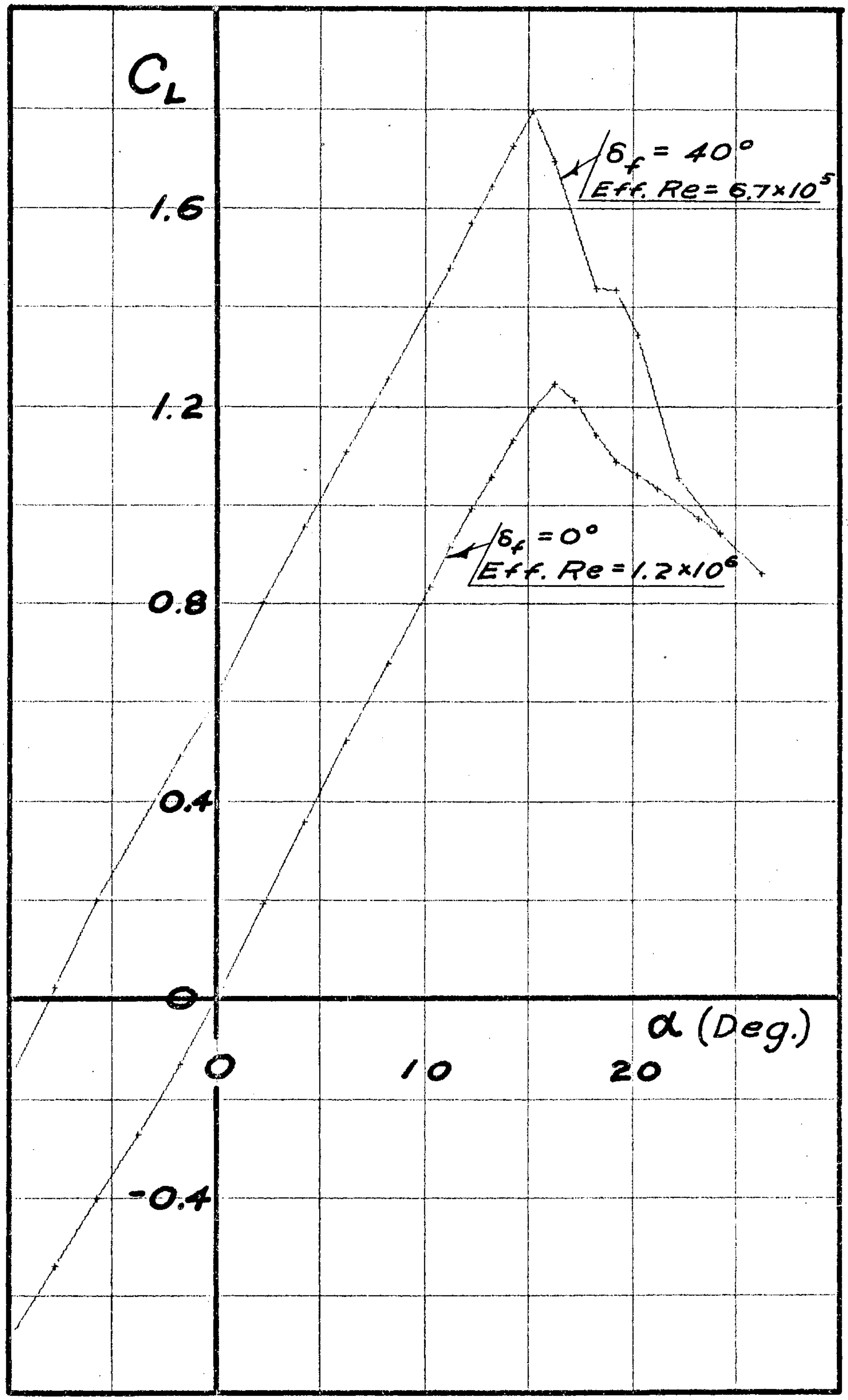

Figure 62. C_L vs α, Basic Wing

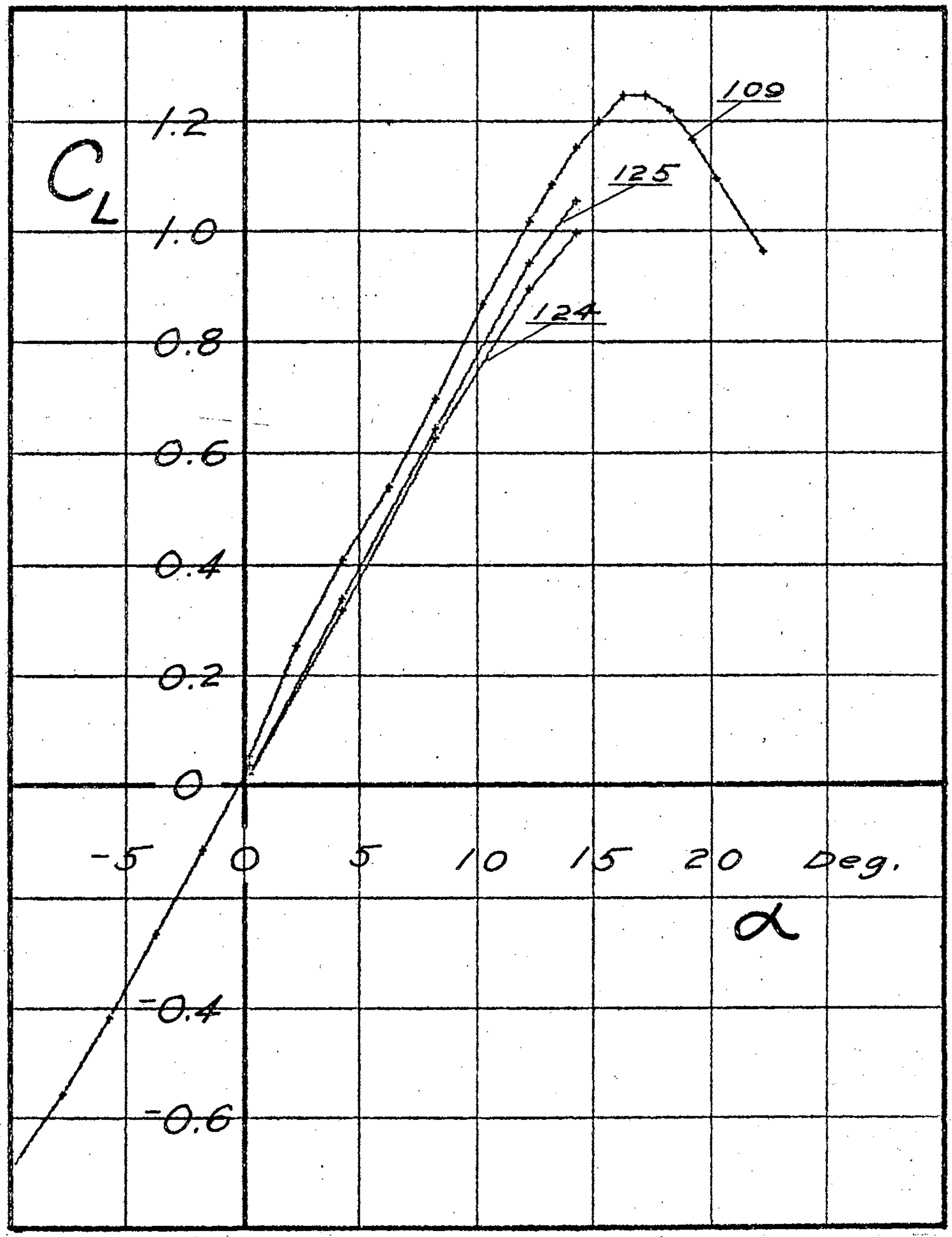

109 -- Dummy Spinner.
124 -- Stationary Propeller, 2 Blades Aligned with the Wing.
125 -- Stationary Propeller, Blades 45° to Wing.

Figure 63. Dummy Spinner

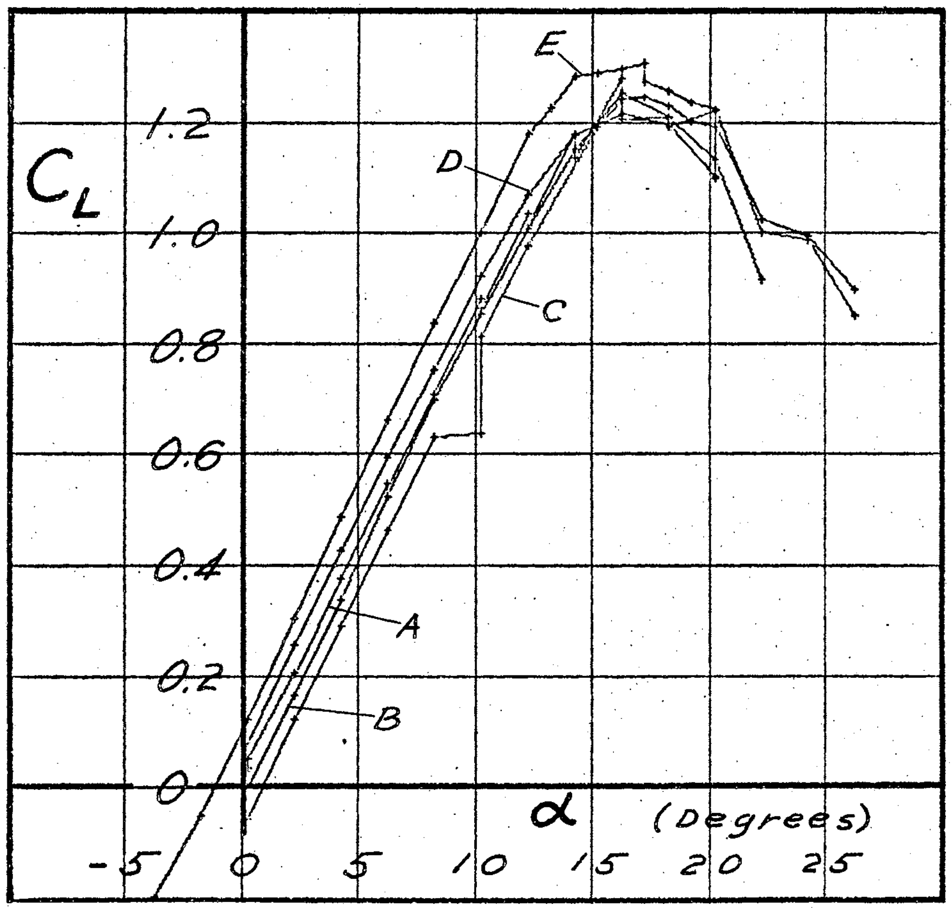

Wing, Pod, and Impeller, $\delta_f = 0$.

A No Rotation -- Runs 114 and 123.
B Vortex-Direction Rotation, N = 50 r.p.s. } 117
C " " " , N = 175r.p.s. }
D Counter-Vortex Rotation, N = 50 r.p.s. } run 123
E " " " , N = 175 " }

Figure 64. Impeller, $\delta_f = 0°$

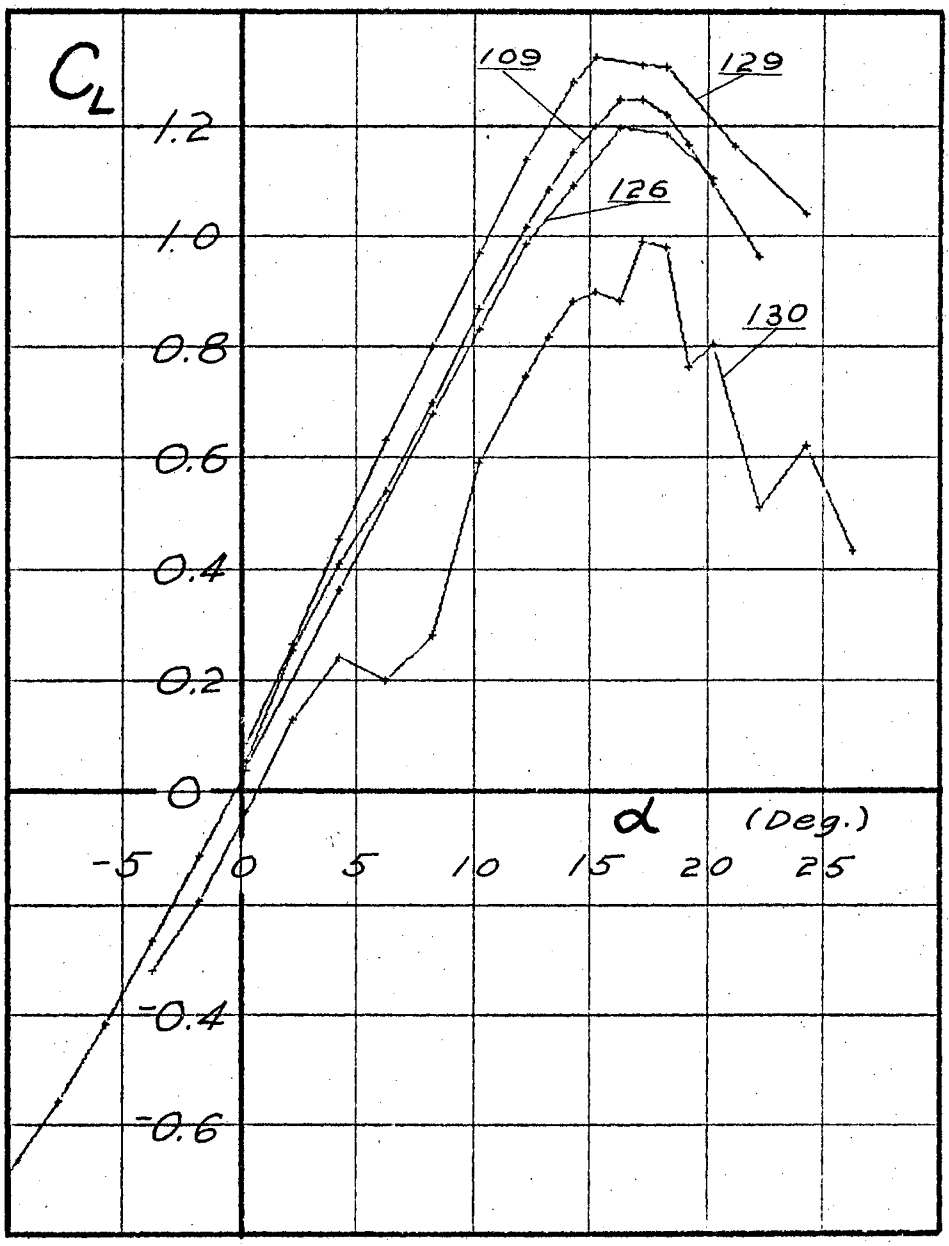

Wing with Pod, $\delta_f = 0.$

109 - Dummy Spinner

126 - Propeller, N = 119 r.p.s. (windmilling)

129 - " , N = 175 r.p.s.

130 - " , N = 50 r.p.s.

Figure 65. Propeller, $\delta_f = 0°$

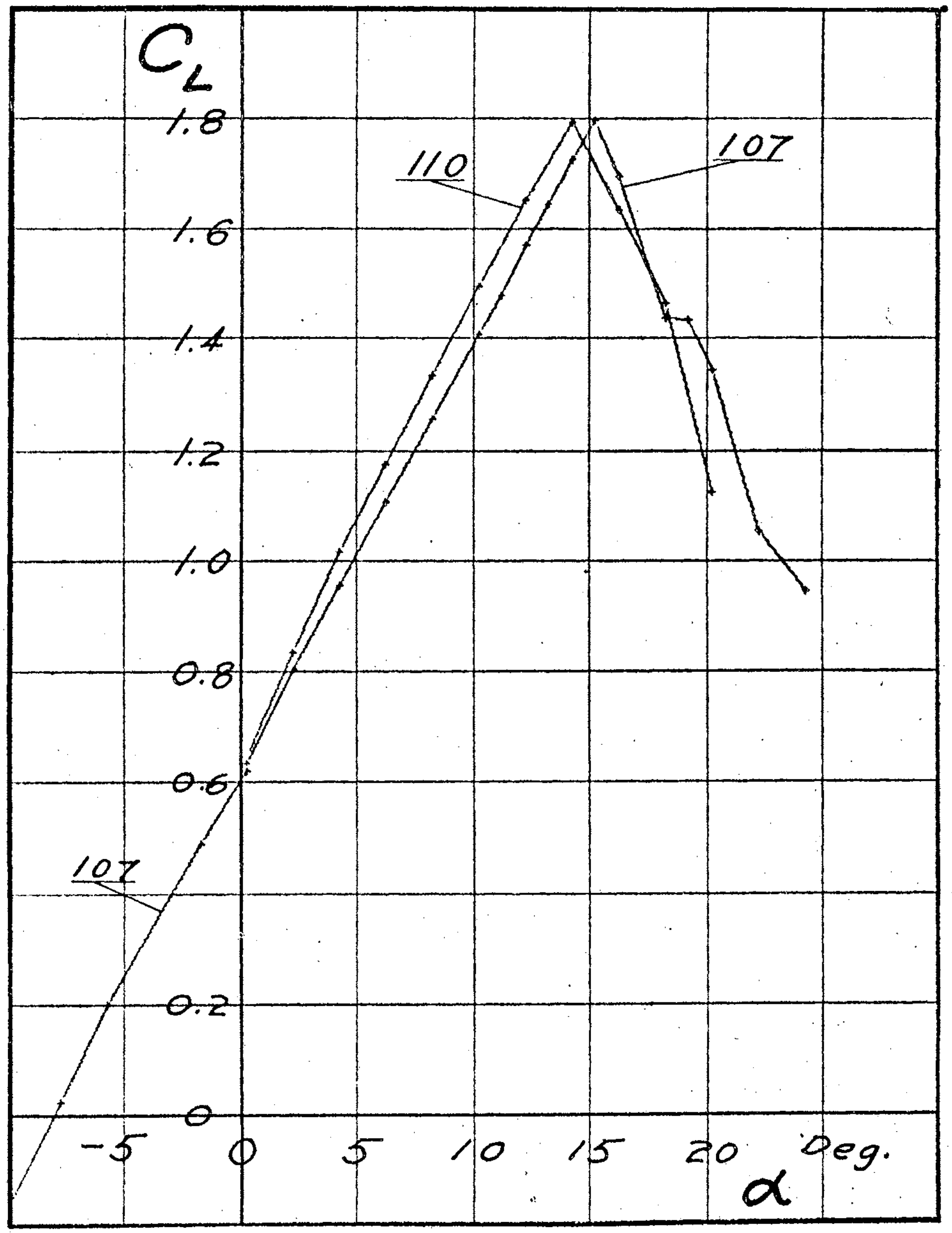

107 -- Wing with Standard Tip.
110 -- Wing, Pod, Dummy Spinner. $\delta_f = 40°$

Figure 66. Basic Wing and Pod, $\delta_f = 40°$

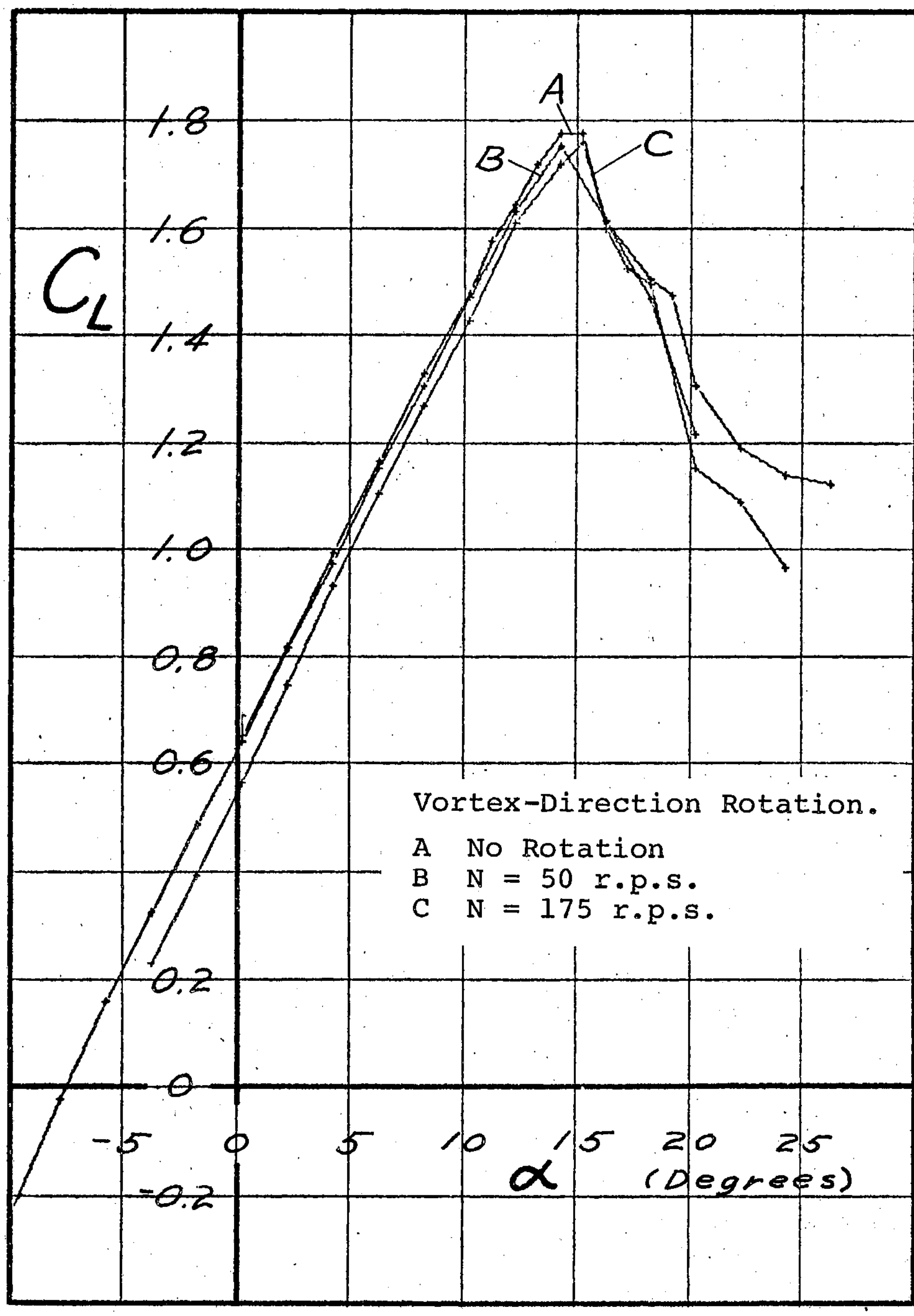

Figure 67. C_L vs α, Impeller, Vortex Rotation

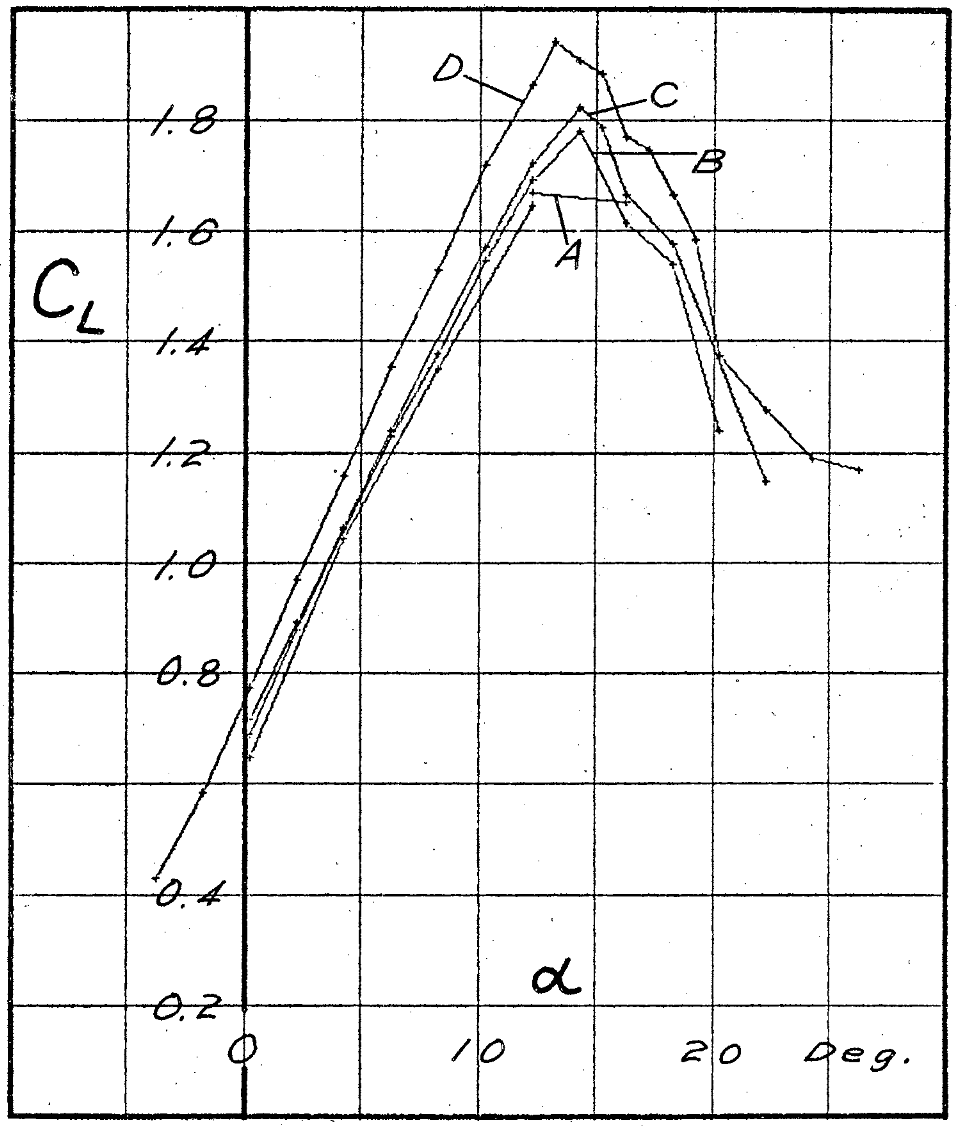

Wing, Pod, and Impeller, $\delta_f = 40°$, Counter-Vortex Rotation.

A - No Rotation
B - N = 50 r.p.s.
C - N = 50 r.p.s.
D - N = 175 r.p.s.

Figure 68. C_L vs α, Impeller, Counter-Vortex Rotation

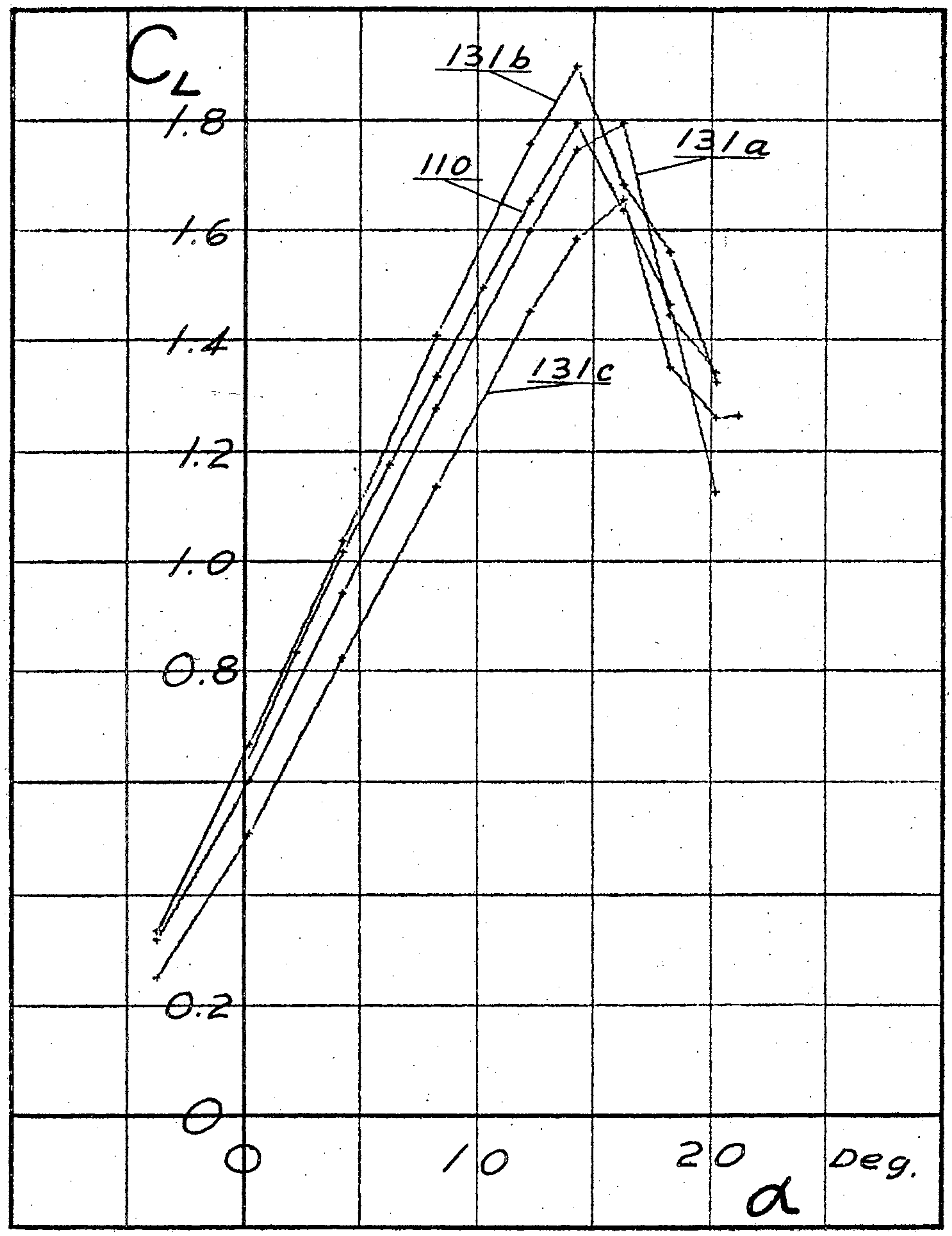

110 -- Dummy Spinner
131a - Windmilling Propeller, N = 120 r.p.s.
131b - Propeller, N = 175 r.p.s.
131c - " , N = 100 r.p.s.

Figure 69. C_L vs α, Propeller, $\delta_f = 40°$

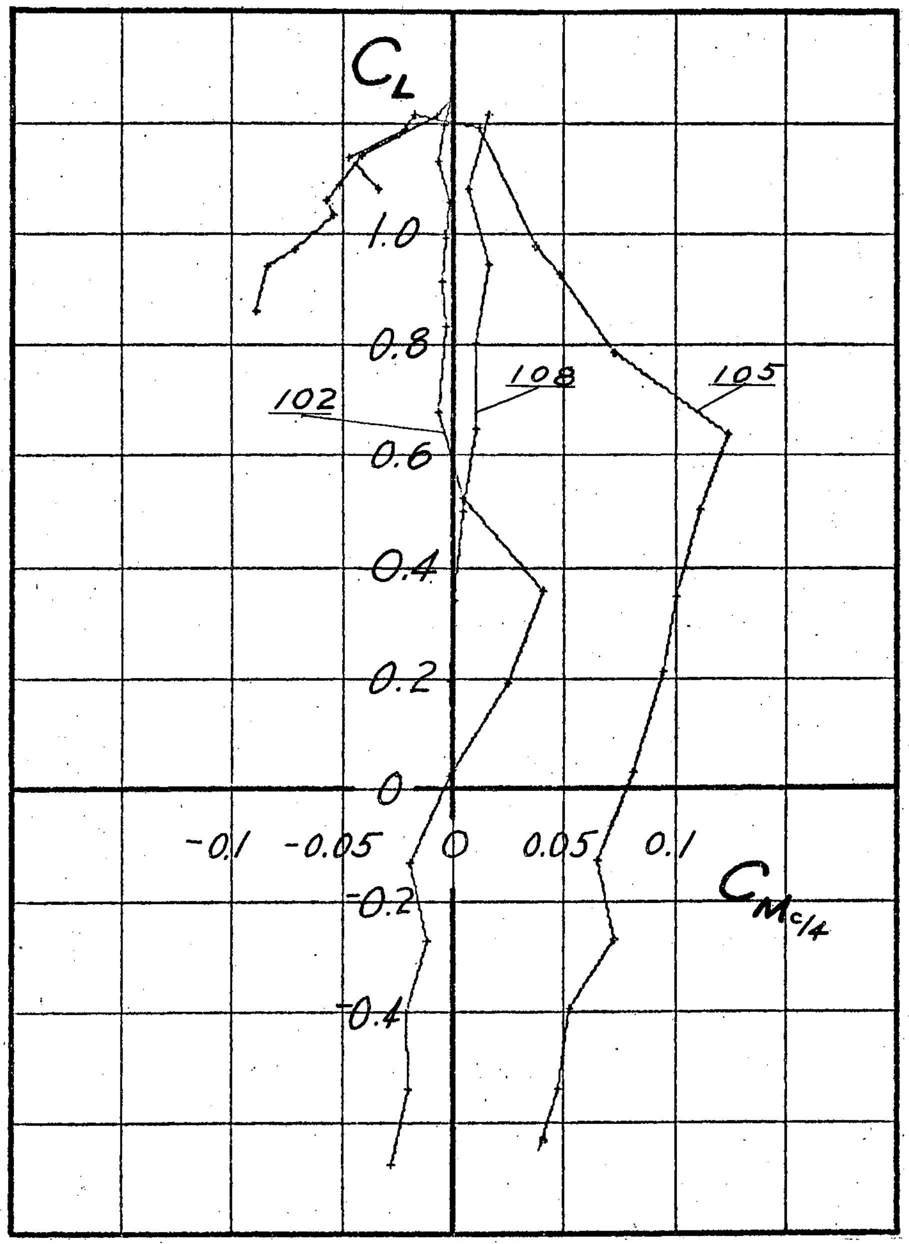

Basic Wing, Standard Tip, $\delta_f = 0$

Runs 105 & 108 -- Eff. Re = 6.7×10^5.

Run 102 -- Eff. Re = 1.2×10^6.

Figure 70. C_L vs $C_{M_{c/4}}$, Basic Wing

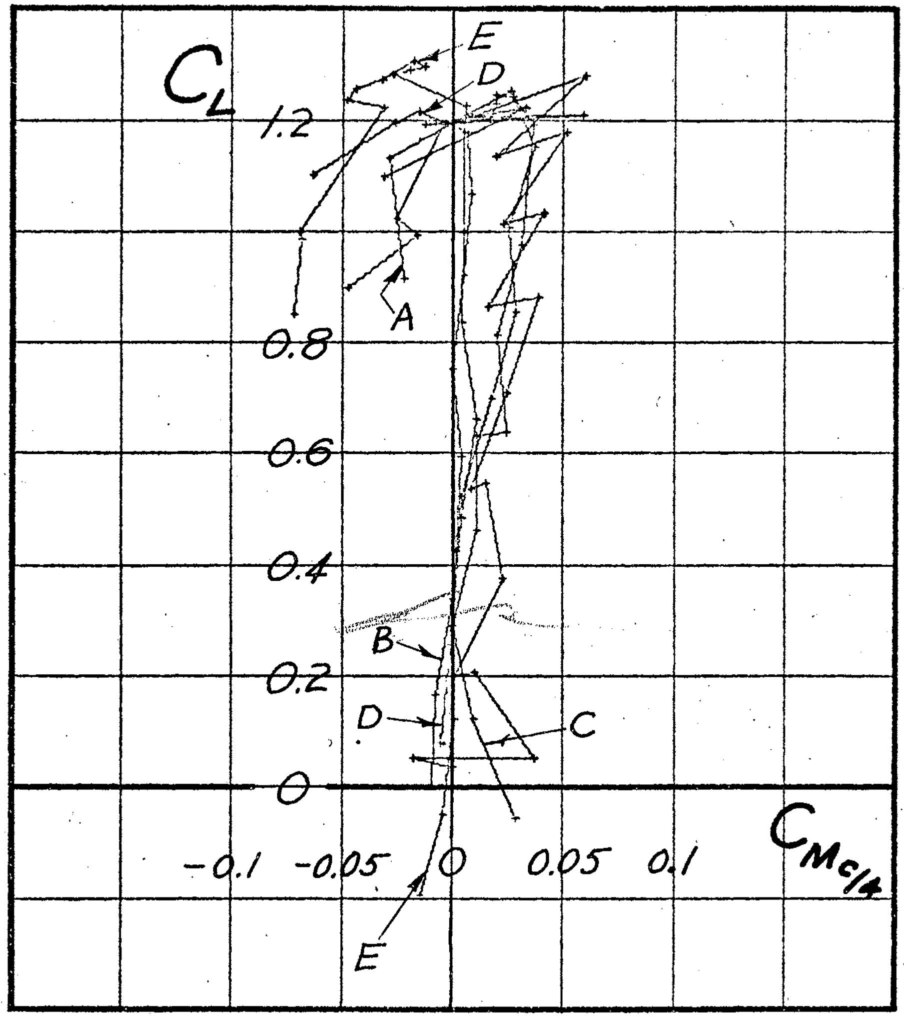

A - No Rotation: Runs 114, 123.

B - Vortex-Direction Rotation, N = 50rps.(117)

C - Vortex-Dir. Rotation, N = 175 rps.(117).

D - Counter-Vortex Rotation, N = 50 rps.(123)

E - Counter-Vortex Rotation, N = 175 rps.

Figure 71. C_L vs $C_{M_{c/4}}$, Impeller, $\delta_f = 0°$

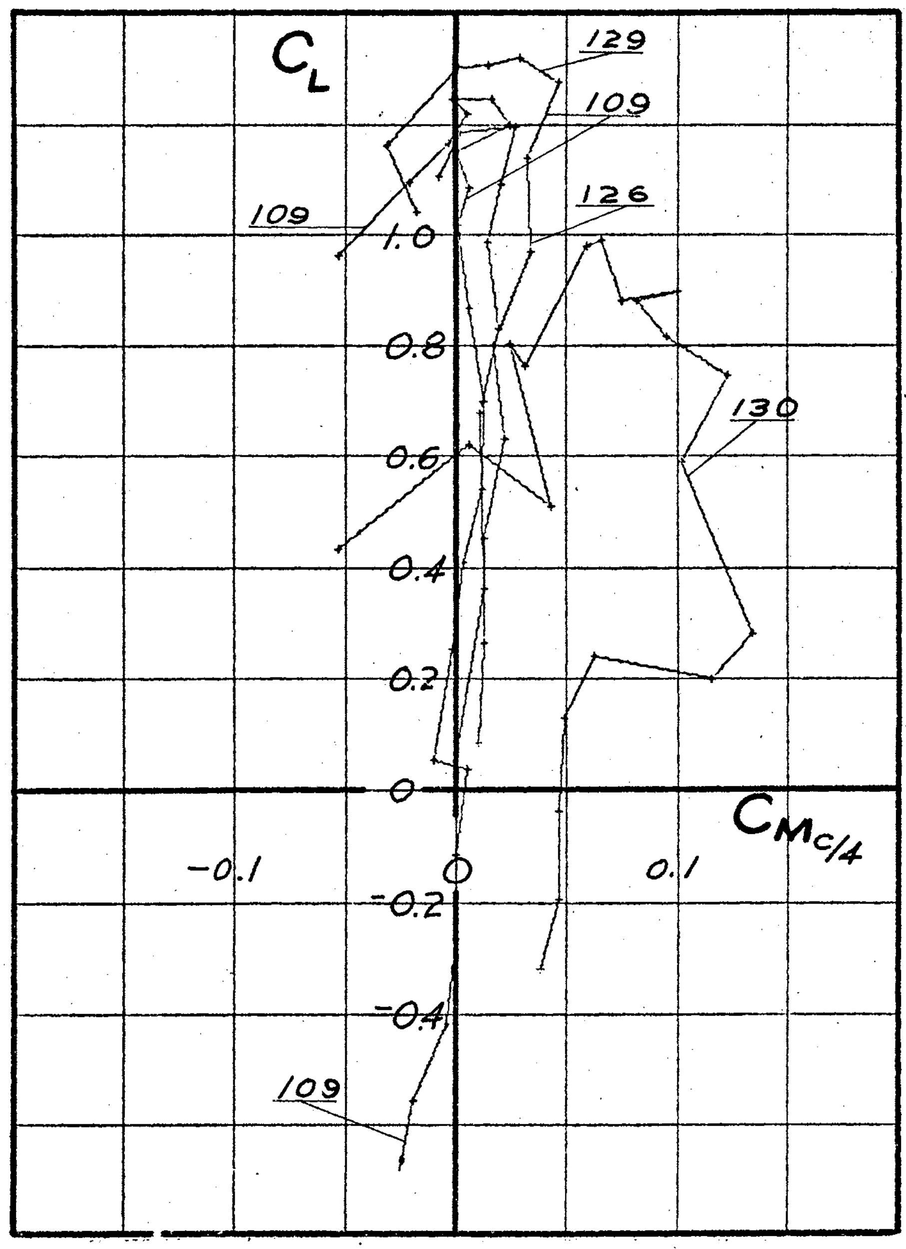

109 -- Dummy Spinner
126 -- Windmilling Propeller, N = 119 r.p.s.
129 -- Propeller, N = 175 r.p.s.
130 -- " , N = 50 r.p.s.

Figure 72. C_L vs $C_{M_{c/4}}$, Propeller, $\delta_f = 0°$

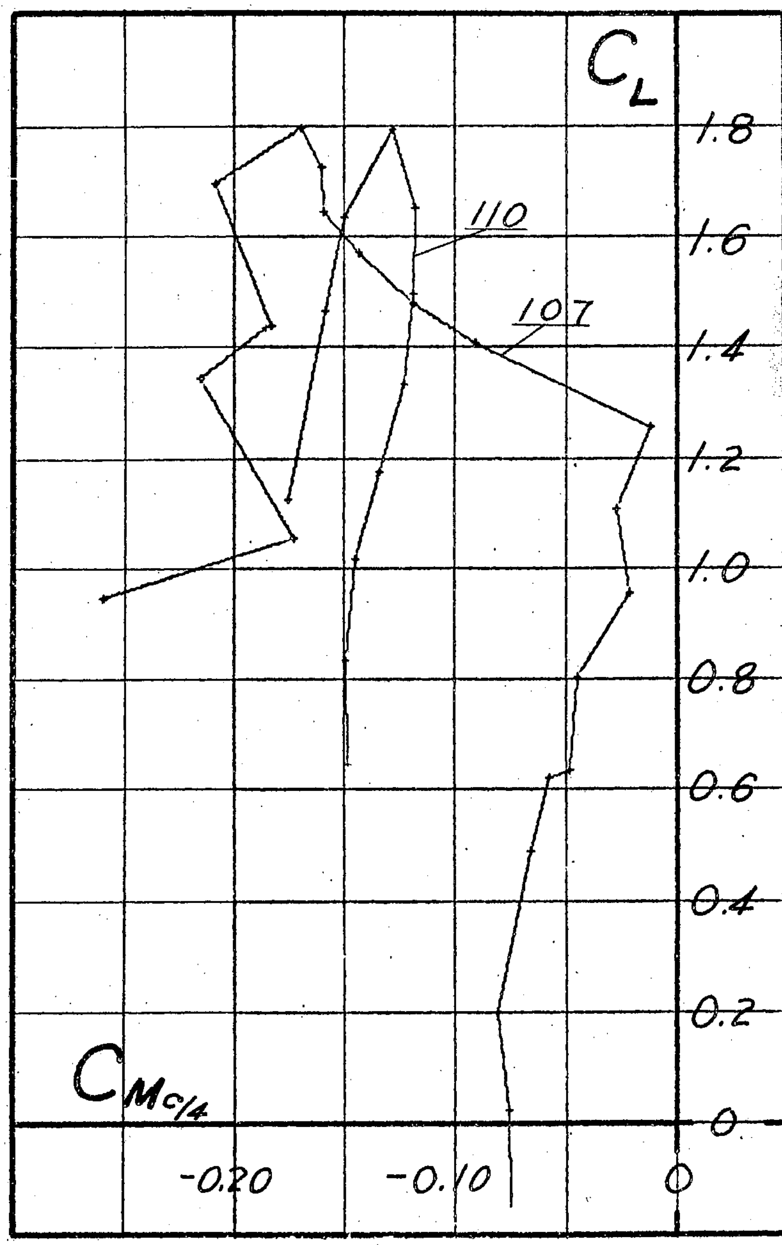

107 -- Wing with Standard Tip.
110 -- Wing with Dummy Pod.

Figure 73. C_L vs $C_{M_{c/4}}$, Basic Wing and Pod, $\delta_f = 40°$

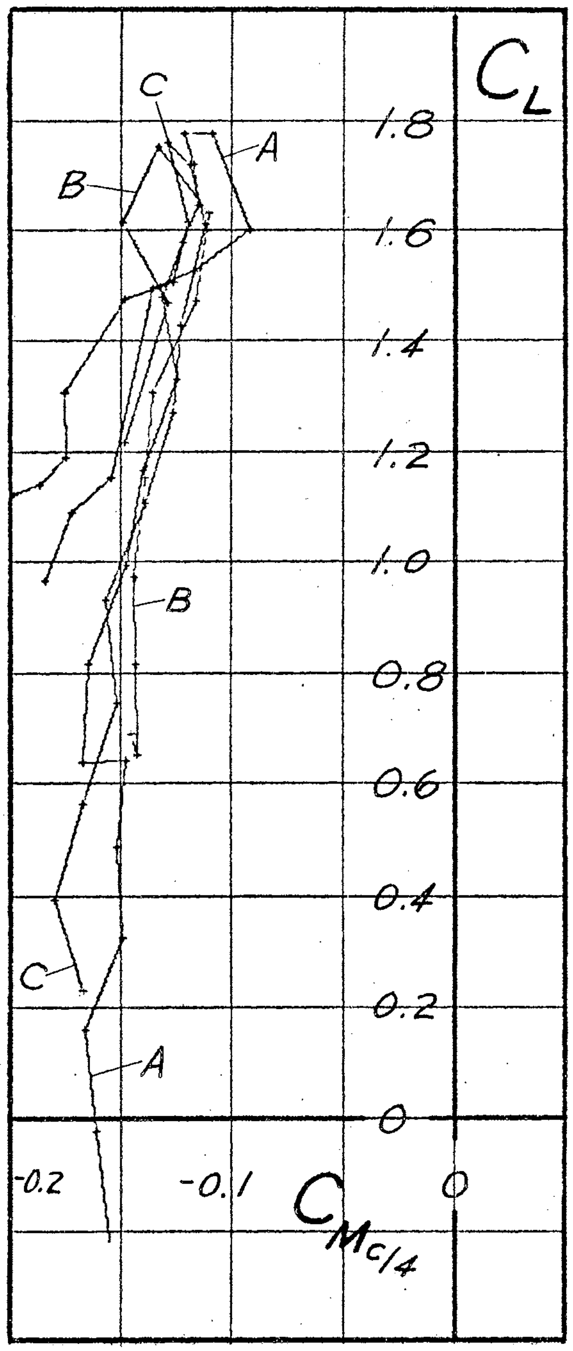

Vortex Direction Rotation

$\delta_f = 40°$

A -- No Rotation.

B -- N = 50 r.p.s.

C -- N = 175 r.p.s.

Wing, Pod, and Impeller.

Figure 74. C_L vs $C_{M_{c/4}}$, Impeller, Vortex Rotation

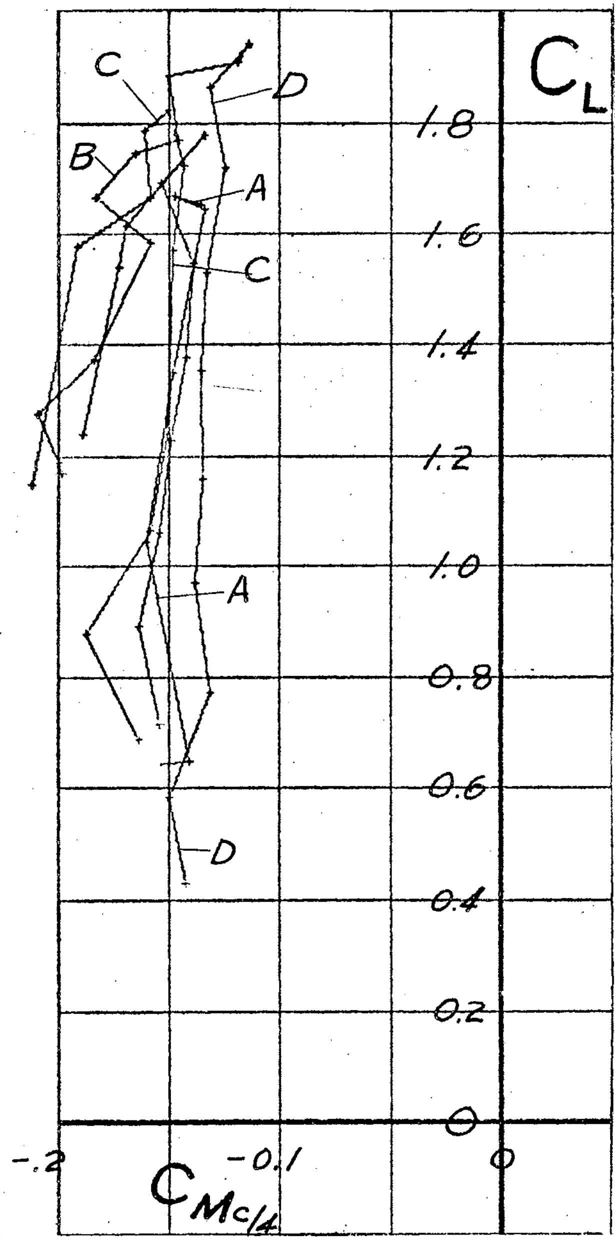

$\delta_f = 40°$

A: No Rotation

B: N=50rps. (run120)

C: N=50rps. (run121)

D: N=175 rps.

Counter-Vortex Rotation.

Wing, Pod, and Impeller.

Figure 75. C_L vs $C_{M_{c/4}}$, Impeller, Counter-Vortex Rotation

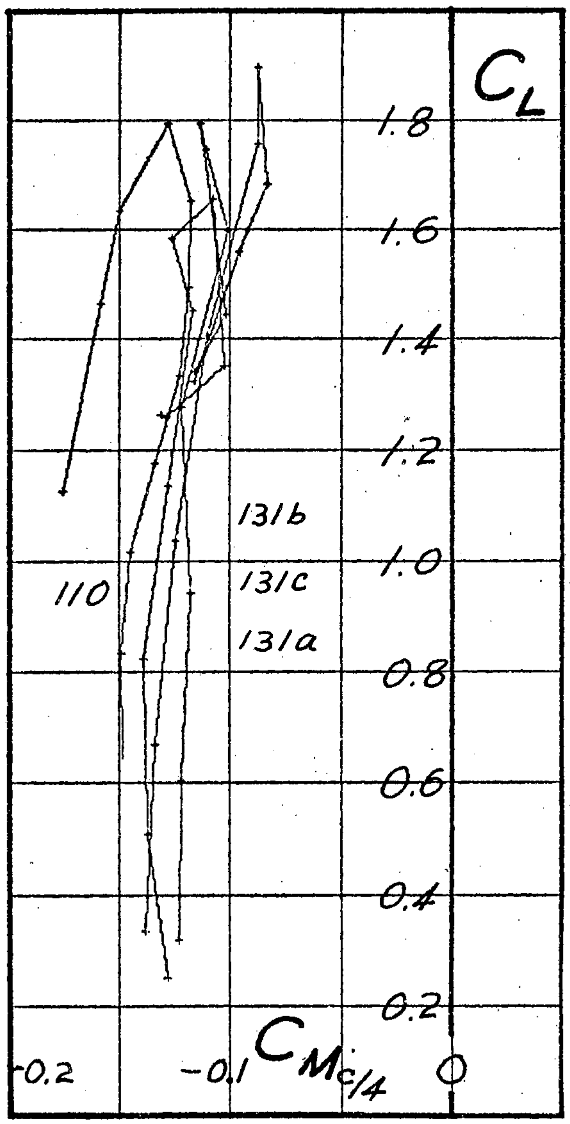

Wing, Pod,
Propeller.

$\delta_f = 40°$

110: Dummy Sinner

131a: Windmilling Propeller, N=120.

131b: N = 175 r.p.s.

131c: N = 100 r.p.s.

Figure 76. C_L vs $C_{M_{c/4}}$, Propeller, $\delta_f = 40°$

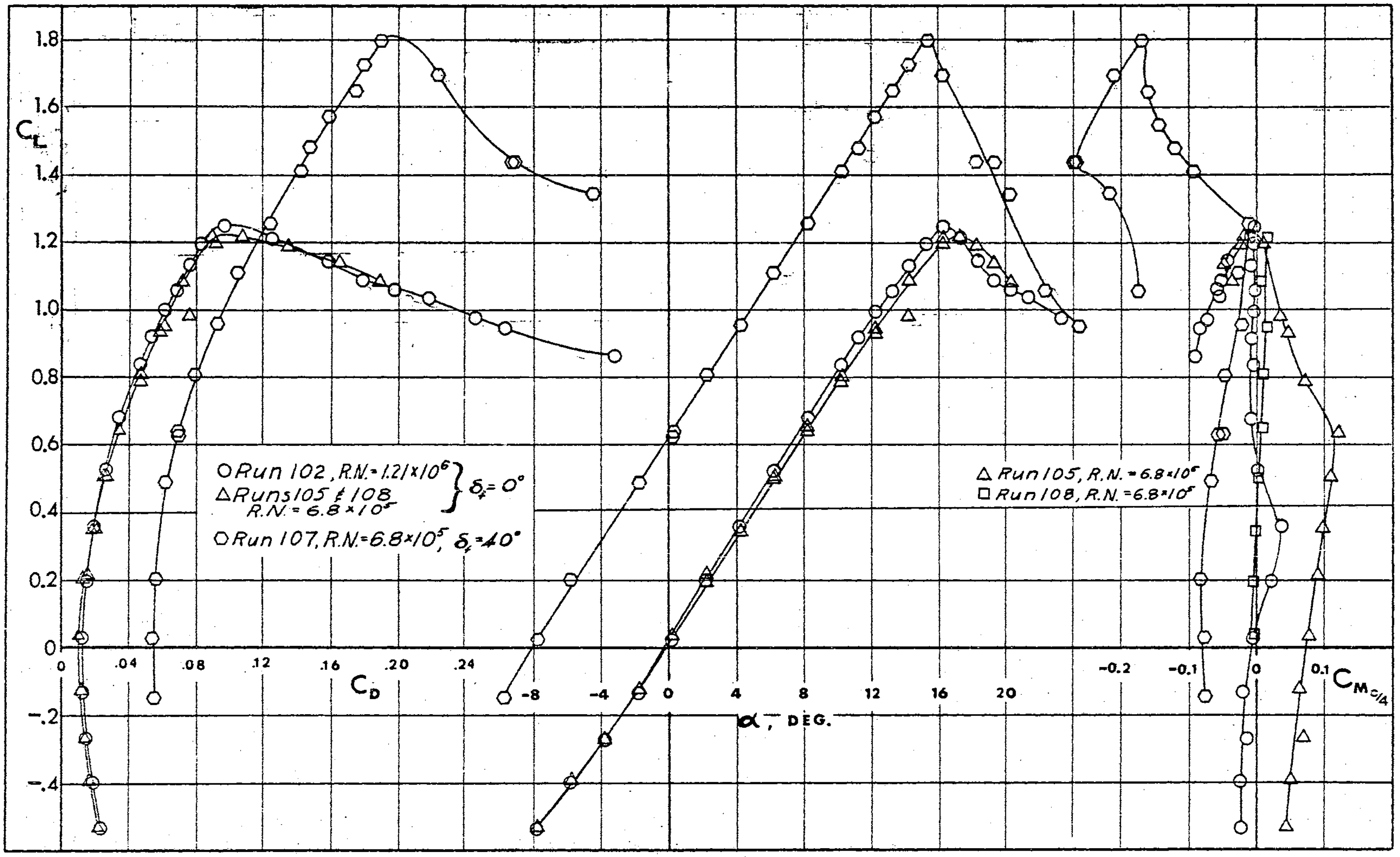

Figure 77. Wing Characteristics, Basic Wing

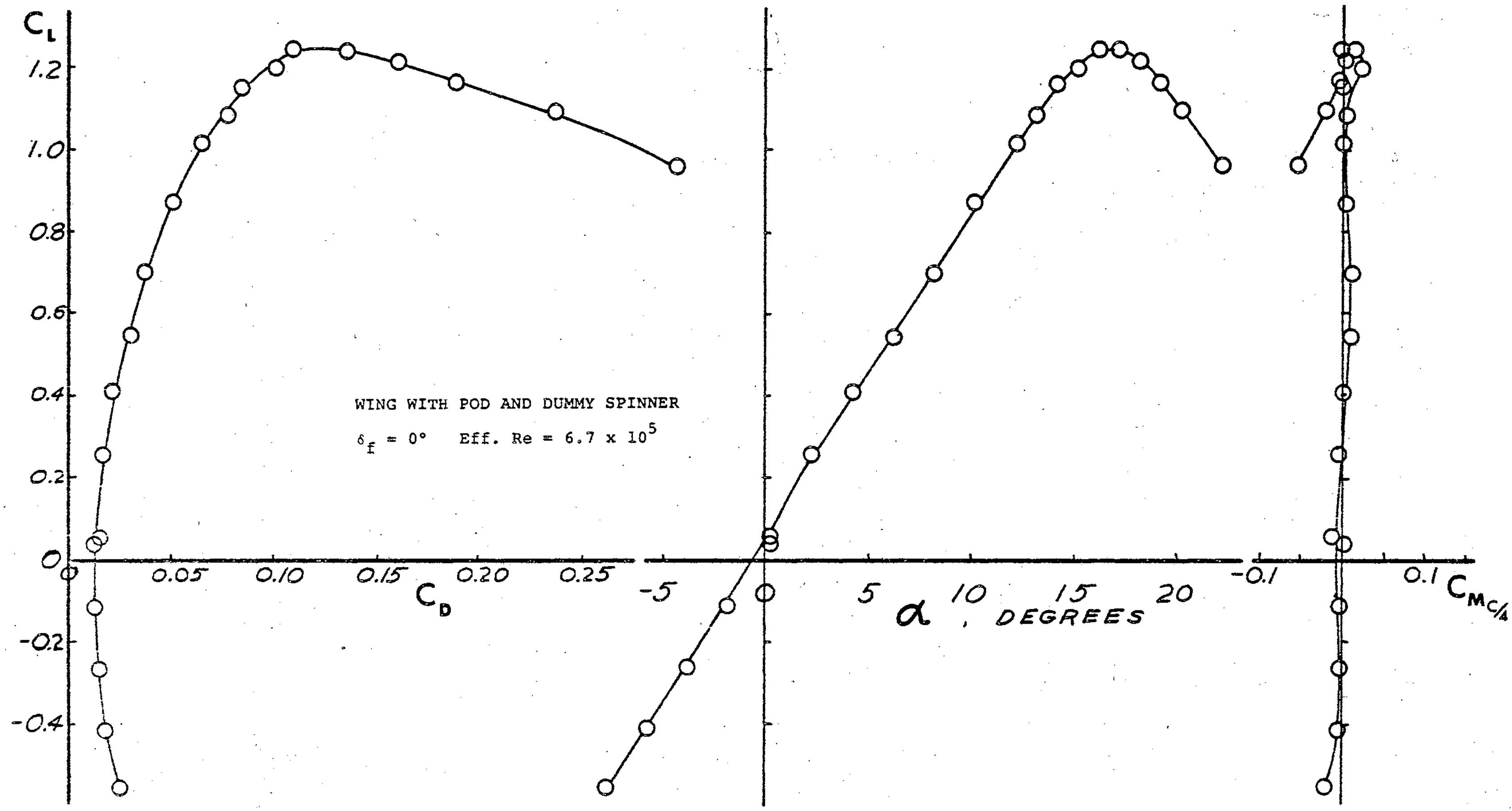

Figure 78. Wing Characteristics, Wing With Pod

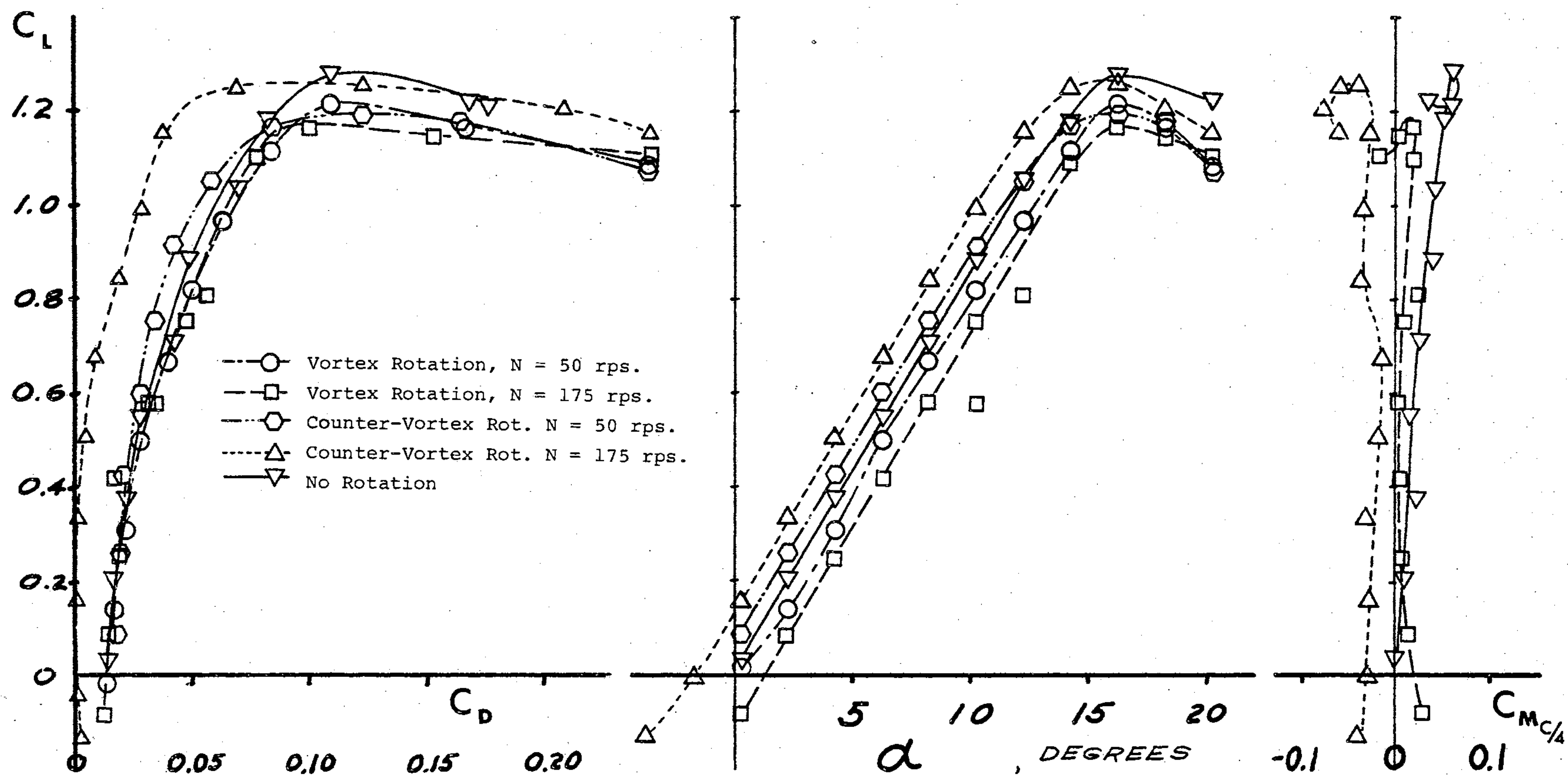

Figure 79. Wing Characteristics, Impeller, Corrected for Thrust

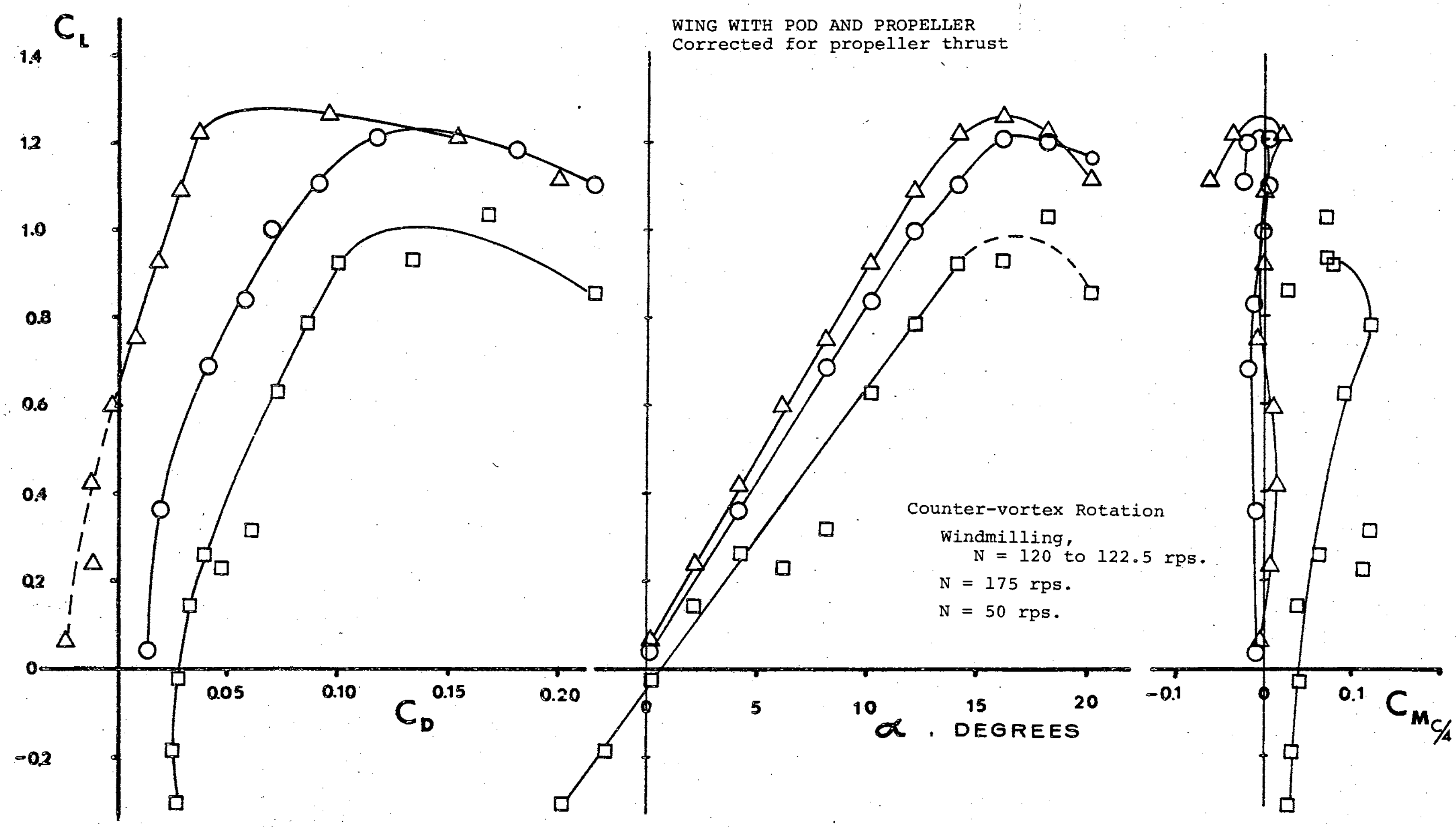

Figure 80. Wing Characteristics, Propeller, Corrected for Thrust

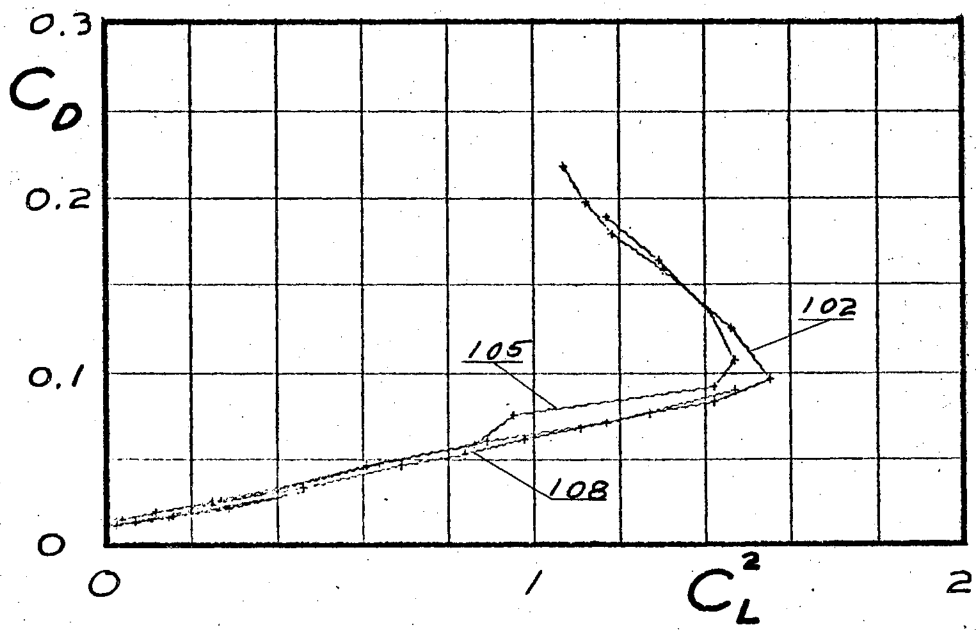

Basic Wing, Standard Tip, $\delta_f = 0°$.
105 & 108: Eff. Re = 6.7×10^5, $C_D = .012 + .0477C_L^2$
102: Eff. Re = 1.2×10^6, $C_D = .014 + .047C_L^2$

Figure 81(a). Drag Polar, Basic Wing

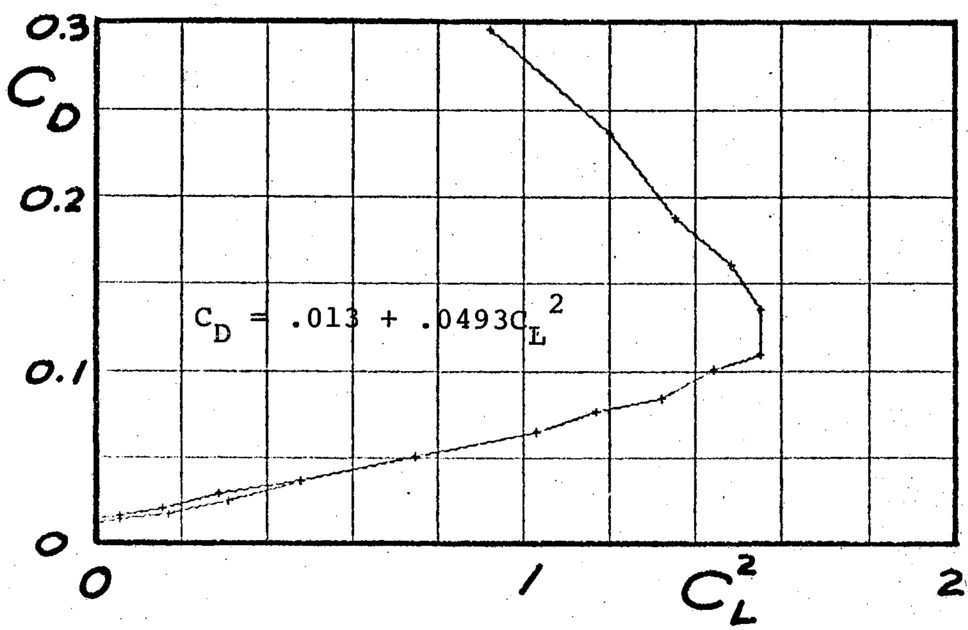

Wing, Pod, Dummy Spinner, $\delta_f = 0°$.
$C_D = .013 + .0493C_L^2$

Figure 81(b). Drag Polar, Dummy Spinner

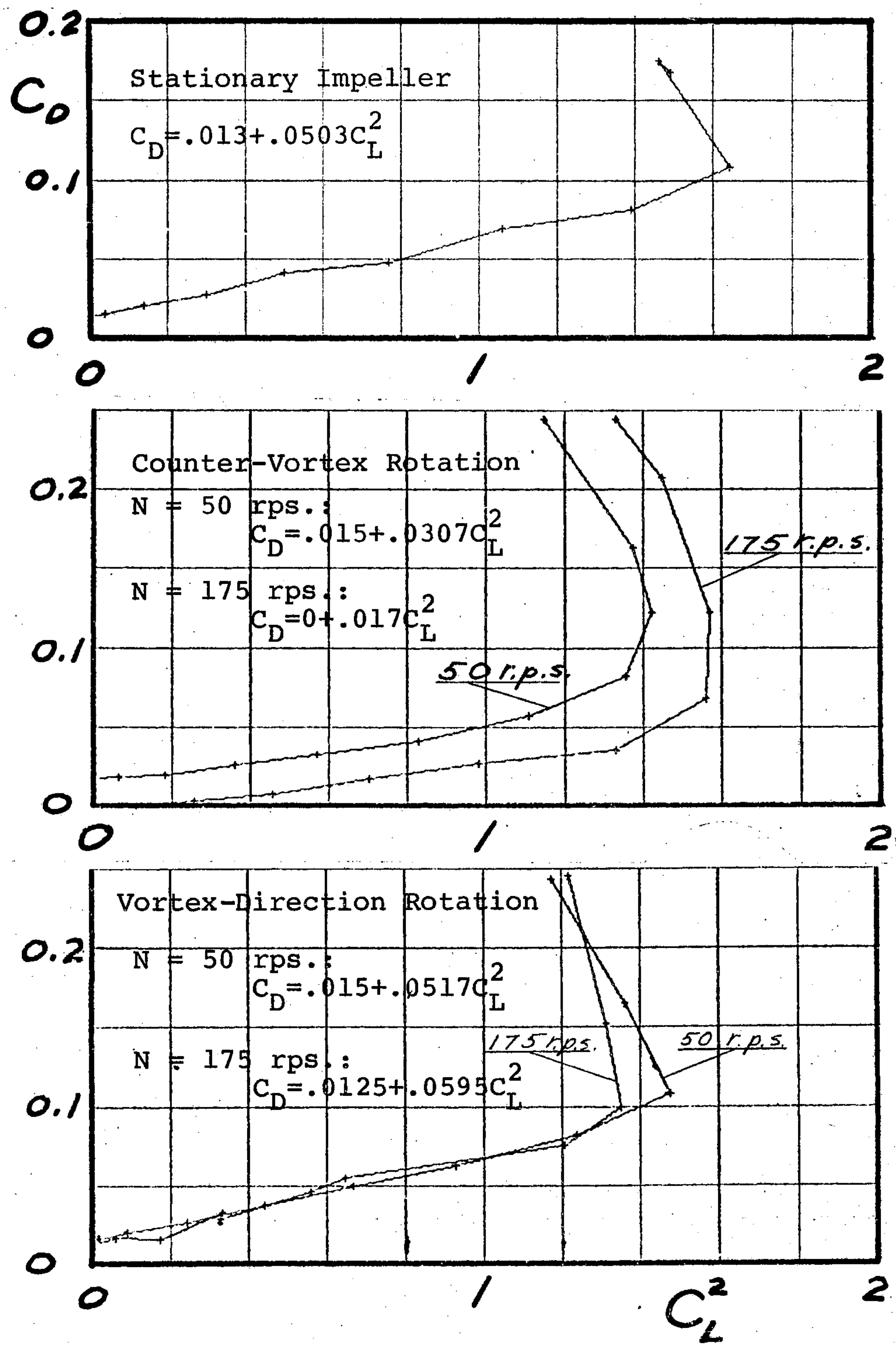

Figure 82. Drag Polar, Impeller Corrected for Thrust

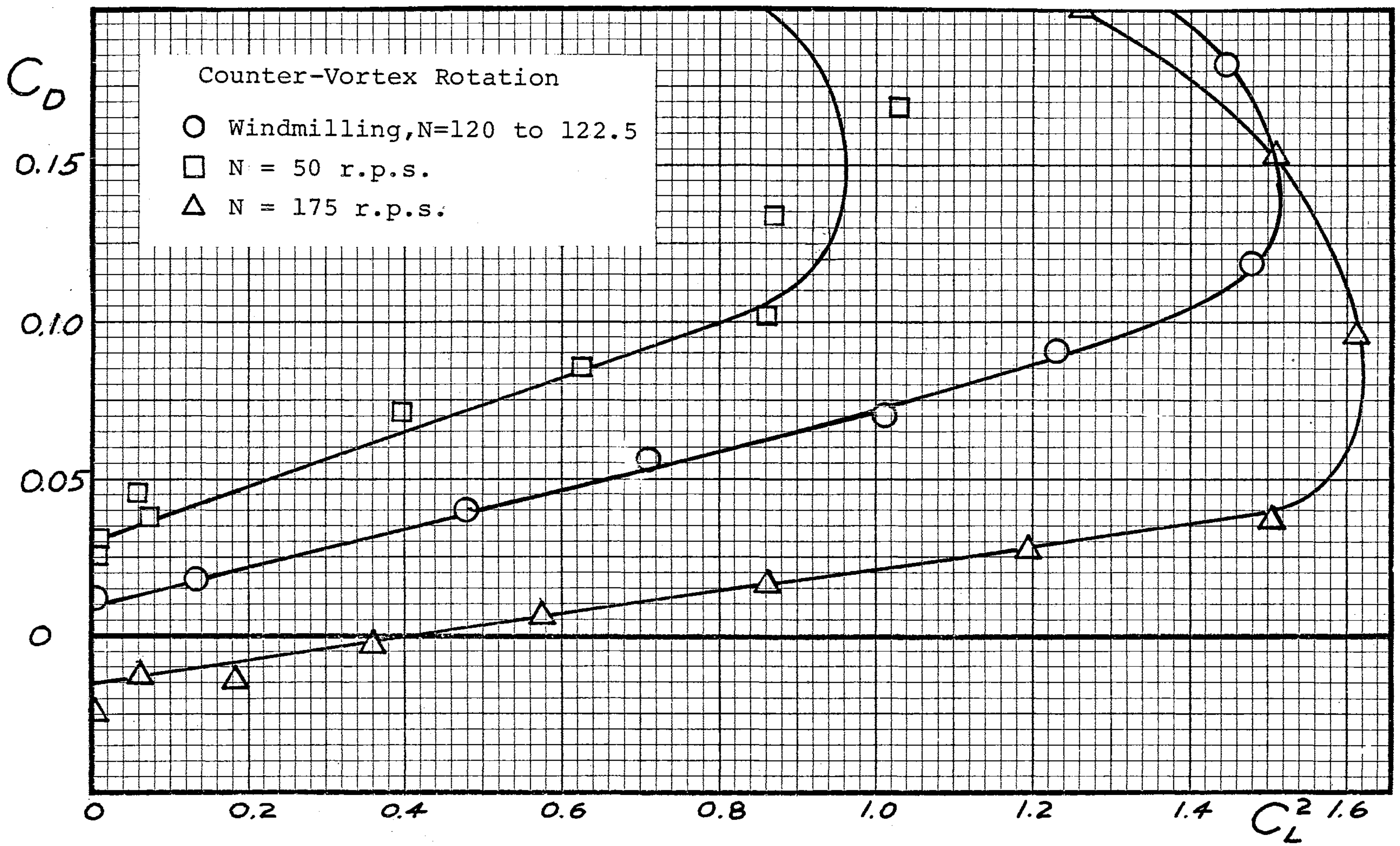

Figure 83. Drag Polar, Propeller Corrected for Thrust

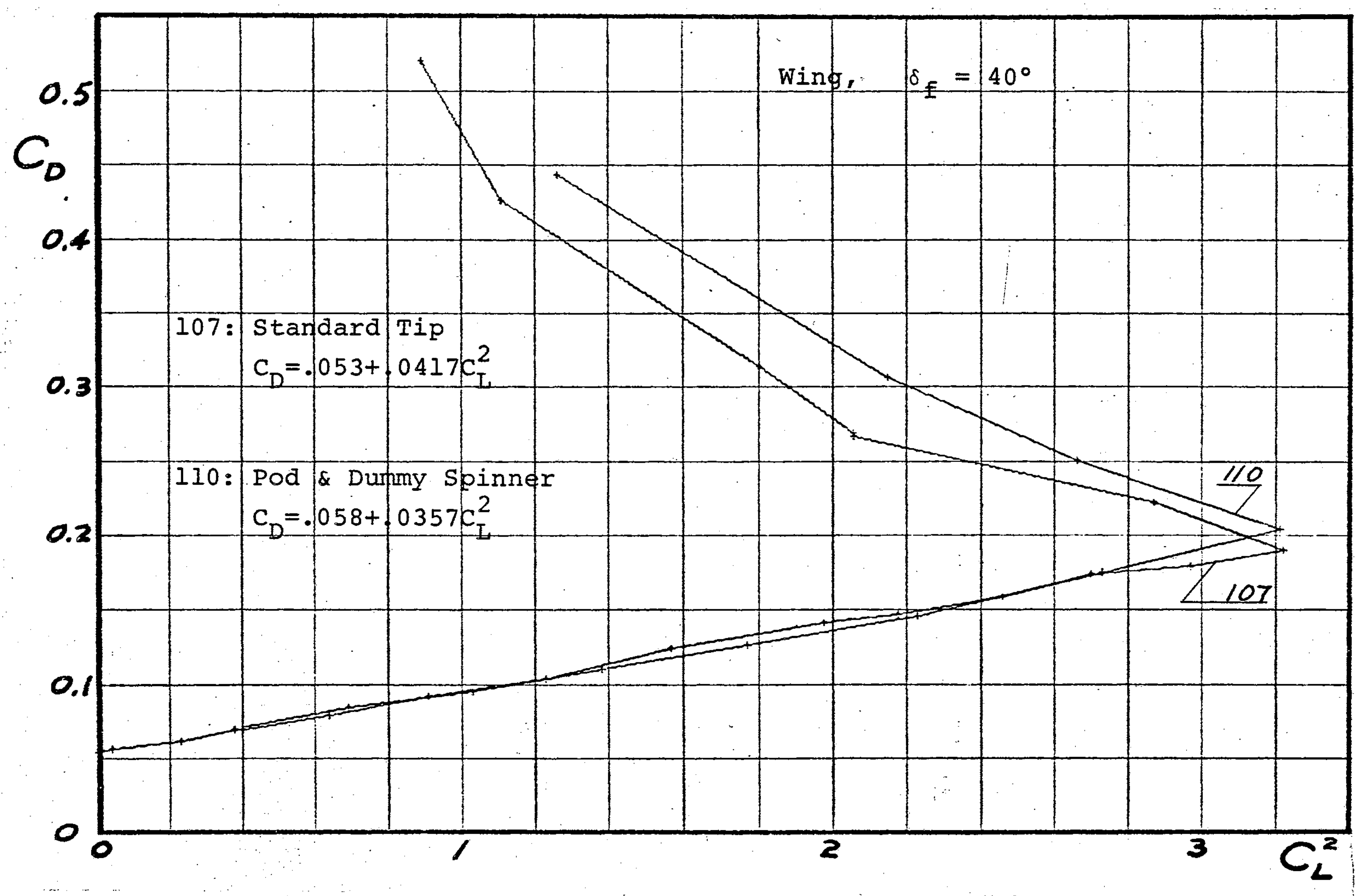

Figure 84. Drag Polar, Dummy Spinner

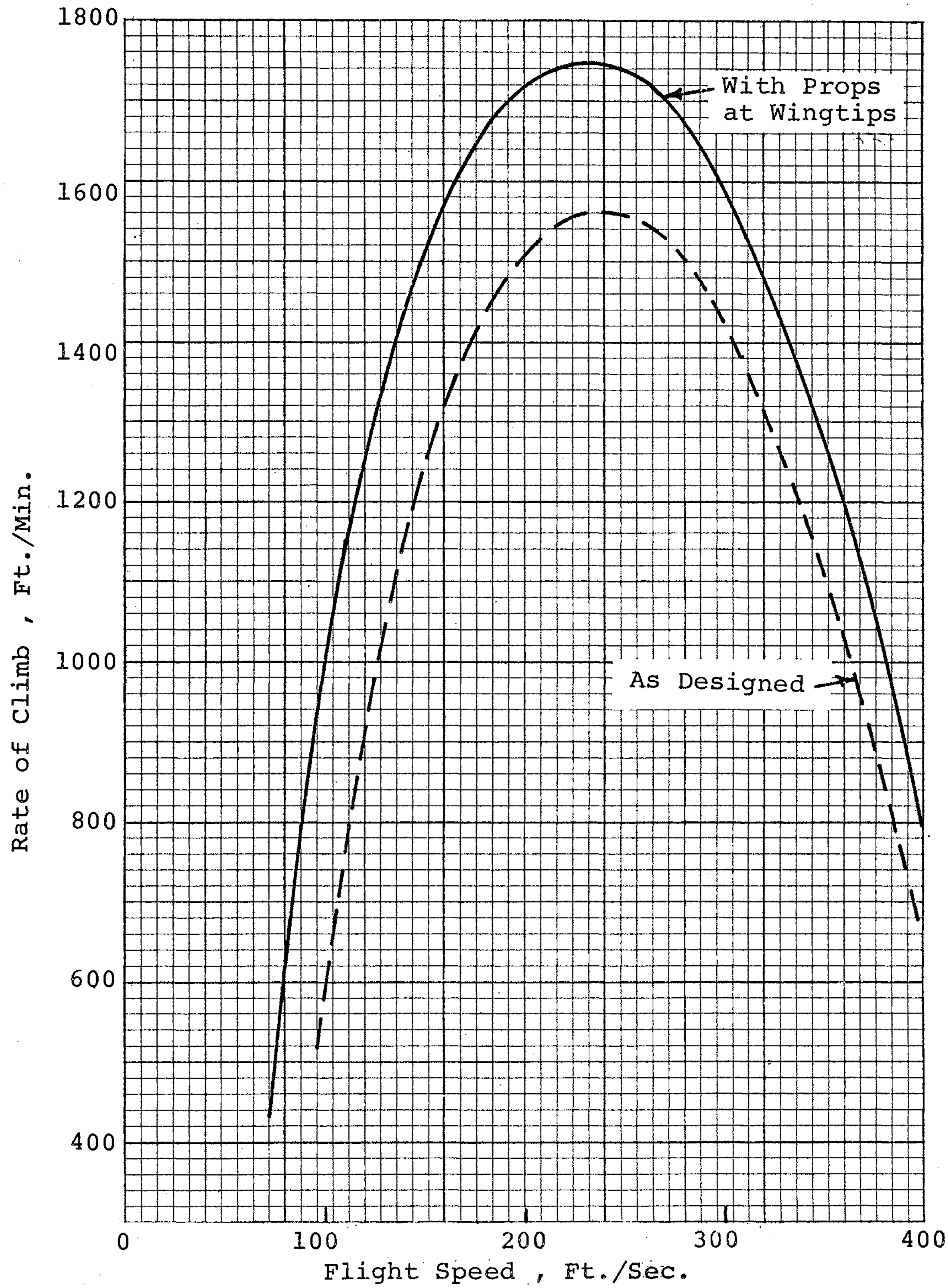

Figure 85. Climb Performance of ASW Airplane

VITA

Melvin H. Snyder, Jr.

Candidate for the Degree of

Doctor of Philosophy

Thesis: EFFECTS OF A WINGTIP-MOUNTED PROPELLER ON WING LIFT, INDUCED DRAG, AND SHED VORTEX PATTERN

Major Field: Mechanical Engineering

Biographical:

Personal Data: Born in Wilkinsburg, Pennsylvania, on September 22, 1921. Married to the former Cathleen Ann Collins, of Wichita, Kansas, and father of six children.

Education: Graduated from Penn High School, Penn Township, Pa., in 1939. Received the Degree of Bachelor of Science in Mechanical Engineering (Aeronautical option) from Carnegie Institute of Technology in January, 1947. Received the Degree of Master of Science in Aeronautical Engineering from Wichita State University (then University of Wichita) in June, 1950. Completed requirements for the Doctor of Philosophy degree in May, 1967.

Professional History: Employed by Wichita State University in the School of Engineering from February, 1947, to the present. Served as Instructor, Assistant Professor, Associate Professor, and became full Professor in 1957. Served as Head to Aeronautical Engineering department for 10 years, Assistant to Dean for two years, and acting Dean of Engineering for one semester. Consulting work has been done for Crosley, Boeing, Beech, and Cessna.

Professional and Learned Societies: Associate Fellow-American Institute of Aeronautics and Astronautics; member of American Society for Engineering Education, Society for the History of Technology, Tau Beta Pi, Sigma Gamma Tau, Pi Mu Epsilon, Pi Delta Epsilon.